Mississippi State University

Scholars Junction

Theses and Dissertations Theses and Dissertations

8-7-2004

Steady State 1D Modeling of PEM Fuel Cell and Characterization of Gas Diffusion Layer

Venkata Ramesh Chilukuri

Follow this and additional works at: https://scholarsjunction.msstate.edu/td

Recommended Citation

Chilukuri, Venkata Ramesh, "Steady State 1D Modeling of PEM Fuel Cell and Characterization of Gas Diffusion Layer" (2004). *Theses and Dissertations*. 4056.
https://scholarsjunction.msstate.edu/td/4056

This Graduate Thesis - Open Access is brought to you for free and open access by the Theses and Dissertations at Scholars Junction. It has been accepted for inclusion in Theses and Dissertations by an authorized administrator of Scholars Junction. For more information, please contact scholcomm@msstate.libanswers.com.

STEADY STATE 1D MODELING OF PEM FUEL CELL AND CHARACTERIZATION OF GAS DIFFUSION LAYER

By

Venkata Ramesh Chilukuri

A Thesis
Submitted to the Faculty of
Mississippi State University
in Partial Fulfillment of the Requirements
for the Degree of Master of Science
in Chemical Engineering
in the Dave C. Swalm School of Chemical Engineering

Mississippi State, Mississippi

August 2004

STEADY STATE 1D MODELING OF PEM FUEL CELL AND CHARACTERIZATION OF GAS DIFFUSION LAYER

By

Venkata Ramesh Chilukuri

Approved:

Hossein Toghiani
Associate Professor of Chemical Engineering
(Director of Thesis and Major Professor)

Junxiao Wu
Research Assistant Professor
Center for Advanced Vehicular Systems
(Committee Member)

Kirk H. Schulz
Earnest W. Deavenport, Jr., Chair,
Director of the Dave C. Swalm
School of Chemical Engineering, and
Professor of Chemical Engineering
(Committee Member)

Rebecca K. Toghiani
Associate Professor of Chemical Engineering
(Committee Member)

Mark E. Zappi
Texas Olefins Professor of Chemical
Engineering and Graduate Coordinator
of the Dave C. Swalm School of
Chemical Engineering

Robert P. Taylor
Interim Dean of the James Worth
Bagley College of Engineering

Name: Venkata Ramesh Chilukuri

Date of Degree: August 7, 2004

Institution: Mississippi State University

Major Field: Chemical Engineering

Major Professor and Director of Thesis: Dr. Hossein Toghiani

Title of Study: STEADY STATE 1D MODELING OF PEM FUEL CELL AND
CHARACTERIZATION OF GAS DIFFUSION LAYER

Pages in Study: 190

Candidate for Degree of Master of Science

In this work, a steady-state, one-dimensional model was developed for the cathode side of the PEM fuel cell. The model results compared well with available literature results. The effects of operating temperature, cathode gas pressure, cathode gas porosity, and membrane thickness were studied.

Carbon materials used for the gas diffusion layer (GDL) were characterized. The materials were: untreated and Teflon-treated carbon paper and untreated and Teflon-treated carbon cloth. Physisorption data were analyzed using the BET and the BJH methods to determine surface area and pore size distribution. Capillary flow porometry measurements provided the bubble point, mean flow, and smallest pore diameters and pore size distribution. Gas permeability measurements were performed. Mercury/non-mercury intrusion porosimetry measurements were performed to obtain pore size distribution and cumulative pore volume. The microstructure structure of the materials

was examined using Scanning Electron Microscopy. The elemental composition of the samples was measured using Energy Dispersive X-ray Spectroscopy.

DEDICATION

I would like to dedicate the work to my family and friends.

ACKNOWLEDGEMENTS

I would like to thank Dr. Hossein Toghiani, my major advisor who provided valuable advice, constant encouragement, guidance, and devotion through out my graduate program. I would also like to thank Dr. Junxiao Wu for his valuable input and suggestions with the modeling component of my research.

I would also like to thank Dr. Rebecca K. Toghiani for serving as my committee member and helping me in my modeling and also providing valuable suggestions during my program of study. I would like to thank my committee member, Dr. Kirk H. Schulz, for his valuable suggestions.

I would like to thank Porous Materials Inc., for conducting porometry and porosimetry experiments.

I would like to acknowledge the financial support of the Center for Advanced Vehicular Systems at Mississippi State University.

I would like to thank Rajkumar and Dr. Yan for providing valuable help during course of my research. I would also like to thank my friends and fellow graduate students for the friendship through out my stay at the Mississippi State University.

TABLE OF CONTENTS

Page

CHAPTER Page

APPENDIX

LIST OF TABLES

Table Page

LIST OF FIGURES

FIGURE Page

FIGURE Page

FIGURE Page

FIGURE Page

CHAPTER I

INTRODUCTION

In recent years, increasing environmental concerns over vehicle-generated pollution and increasing demand for energy sources have generated interest in alternative fuels and energy sources. The high efficiency and near-zero emissions of fuel cells make them a potential alternative energy source for both automotive and stationary power applications (Kordesch and Simander, 1995). Although fuel cells have been around for many years, they have recently received more attention in the media. This is due to a number of major automotive manufacturers and various federal agencies supporting research and development of fuel cell technology for use in vehicles powered by fuel cells. Fuel cell energy is anticipated to replace traditional power sources in the future, with applications ranging from micro fuel cells to be used in cell phones and laptops, to high-powered fuel cells for automobiles and stationary power generation.

The main challenge for the fuel cell industry will be to commercialize these fuel cell systems by improving their performance and decreasing their cost. In this chapter, an introduction to fuel cells is provided. The various types of fuel cells are presented with an emphasis on their advantages and disadvantages when compared to traditional power generation systems.

1.1 Overview of Fuel Cells

Fuel cells are electrochemical devices, which convert the chemical energy contained in fuels directly into electrical energy. Since electrical energy is produced without any combustion of fuel, fuel cells are virtually pollution free. If pure hydrogen gas is used as fuel, then only water and heat are produced as products. However, if reformate fuel is used, then some pollutants are released, but their concentrations are very low when compared to those generated by conventional combustion devices. Typically, a fuel cell consists of two porous electrodes (anode and cathode) separated by an electrolyte. A schematic of an individual fuel cell components (EG&G Technical Services Inc., 2002) is shown in Figure 1.1.

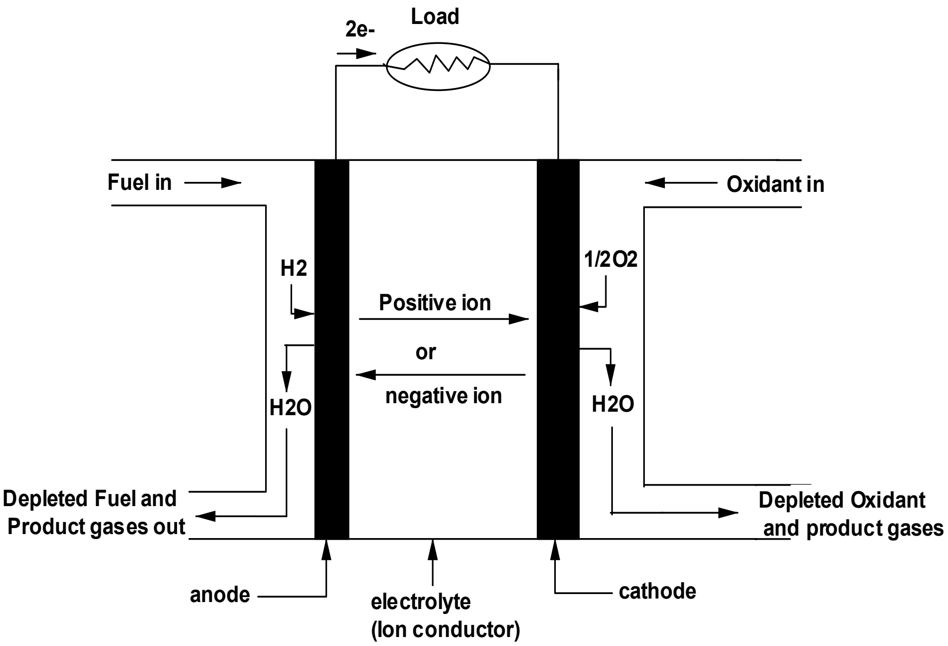

Figure 1.1. Schematic of an Individual Fuel Cell (EG&G Technical Services Inc., 2002).

Fuel cells are similar to a traditional battery, but differ in several aspects. The battery is an energy storage device. The maximum energy available is determined by the amounts of chemical reactants stored in the battery. In contrast, the fuel cell is an energy conversion device that can conceivably produce electrical energy as long as fuel and oxidant are supplied to the electrodes. The practical operating life of a fuel cell is determined by the lifetime of the various components, which can be significantly reduced by processes including catalyst deactivation and membrane degradation.

During operation, gaseous fuel is fed continuously to the anode and oxidant gas is fed continuously to the cathode. The electrochemical reactions take place at the electrodes. For example, in an acid electrolyte fuel cell, two primary reactions occur. At the anode, the hydrogen gas is ionized, releasing electrons and protons (H^+ ions), as shown in equation (1.1.1).

$$2H_2 \rightarrow 4H^+ + 4e^- \tag{1.1.1}$$

Electrons travel through the external load to reach the cathode, while the protons (hydrogen ions) travel through the electrolyte to reach the cathode. At the cathode, oxygen combines with the electrons and protons to produce water via reaction (1.1.2)

$$O_2 + 4H^+ + 4e^- \rightarrow 2H_2O \tag{1.1.2}$$

The reactions that take place at the electrodes depend on the type of electrolyte employed in the fuel cell. Since an individual fuel cell will produce only a very small voltage, several fuel cells are often connected in series, known as stacks, to produce the desired voltage.

The most common fuel used in fuel cells is gaseous hydrogen because of its high reactivity and high energy density. Similarly, the most commonly used oxidant is gaseous oxygen because it is readily available from air. Other types of fuels including hydrocarbons and methane can also be used with a reformer. Some fuel cells operate at very high temperatures so that the reformation of fuel can occur within the cell (internal reforming). The electrical energy produced by the fuel cell is DC voltage, which must be converted to AC voltage for many applications.

1.2 Types of Fuel Cells

A number of different types of fuel cells are available. They can be classified based on the type of electrolyte used. The most common types of fuel cells are:

- Phosphoric Acid Fuel Cell (PAFC)
- Alkaline Fuel Cell (AFC)
- Proton Exchange Membrane Fuel Cell (PEMFC)
- Molten Carbonate Fuel Cell (MCFC)
- Solid Oxide Fuel Cell (SOFC)
- Direct Methanol Fuel Cell (DMFC)

A brief description of each type of fuel cell is provided.

1.2.1 Phosphoric Acid Fuel Cell (PAFC)

The phosphoric acid fuel cell is commercially available today. The electrolyte used is concentrated phosphoric acid. The operating temperature of a PAFC is between

150 and 220° C (EG&G Technical Services, 2002). At low temperatures, phosphoric acid is a poor ionic conductor and carbon monoxide poisoning of the platinum catalyst at the anode becomes severe. The PAFC generates low current and power compare to other types of fuel cells. The primary reactions in the PAFC are (EG&G Technical Services, 2002):

$$\text{Anode: } H_2 \rightarrow 2H^+ + 2e^- \tag{1.2.1.1}$$

$$\text{Cathode: } \frac{1}{2}O_2 + 2H^+ + 2e^- \rightarrow H_2O \tag{1.2.1.2}$$

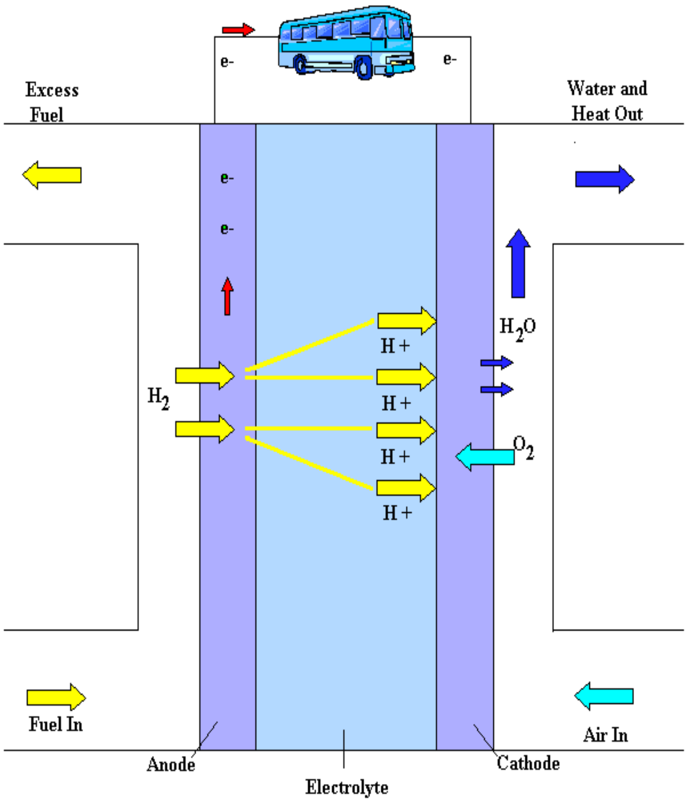

Figure 1.2. Schematic of PAFC $^{(a)}$.

$^{(a)}$→ Adapted from http://www.eere.energy.gov/hydrogenandfuelcells/fuelcells/fc_types.html

1.2.2 Alkaline Fuel Cell (AFC)

NASA used alkaline fuel cells on space missions to provide both electricity and water. An aqueous solution of alkaline potassium hydroxide is used as the electrolyte. These fuel cells operate at temperatures between 80 and 200° C (Larminie and Dicks, 2003). The main problem with the alkaline fuel cell is poisoning by carbon dioxide. Carbon dioxide reacts with potassium hydroxide to form potassium carbonate, which terminates the transport of ions through the electrolyte. The reactions occurring in the alkaline fuel cell are (Larminie and Dicks, 2003):

$$\text{Anode: } 2H_2 + 4OH^- \rightarrow 4H_2O + 4e^- \qquad (1.2.2.1)$$

$$\text{Cathode: } O_2 + 2H_2O + 4e^- \rightarrow 4OH^- \qquad (1.2.2.2)$$

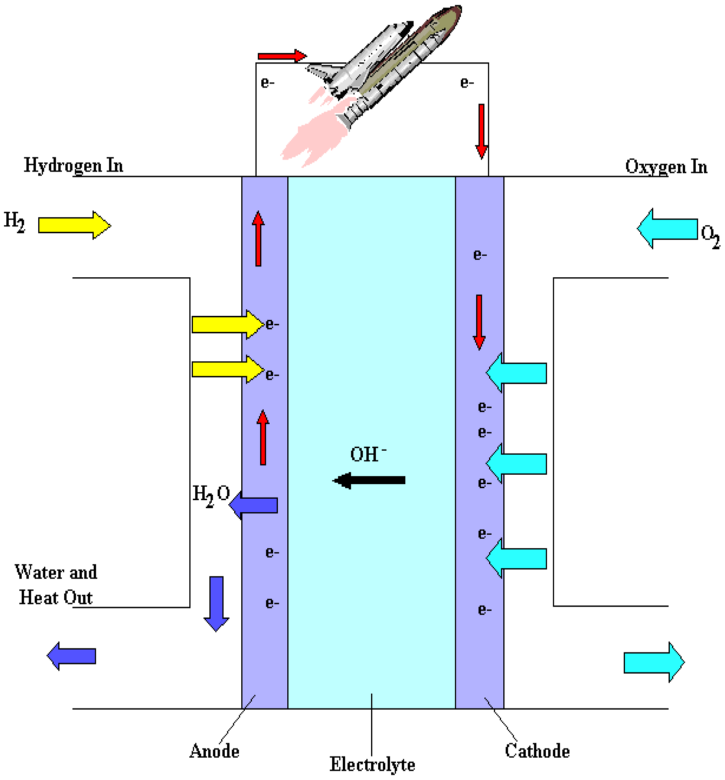

Figure 1.3. Schematic of AFC (a).

(a)→ Adapted from http://www.eere.energy.gov/hydrogenandfuelcells/fuelcells/fc_types.html

1.2.3 Proton Exchange Membrane Fuel Cell (PEMFC)

Proton exchange membrane fuel cells (PEMFC) operate at relatively low temperatures (between 60 and 80° C), allowing for faster startup and immediate response to changes in demand for power. They are able to generate high power density. Nafion membrane is used as the electrolyte. Nafion is a good conductor of protons and a good electronic insulator, but is essentially impermeable to hydrogen (fuel) and oxygen (oxidant). Carbon monoxide poisoning of the electro-catalyst is one of the main problems for PEM fuel cells. PEM fuel cells are discussed in more detail in Chapter 2. The reactions taking place in the PEM fuel cell are (Larminie and Dicks, 2003):

$$\text{Anode:}\quad 2H_2 \rightarrow 4H^+ + 4e^- \tag{1.2.3.1}$$

$$\text{Cathode:}\quad O_2 + 4H^+ + 4e^- \rightarrow 2H_2O \tag{1.2.3.2}$$

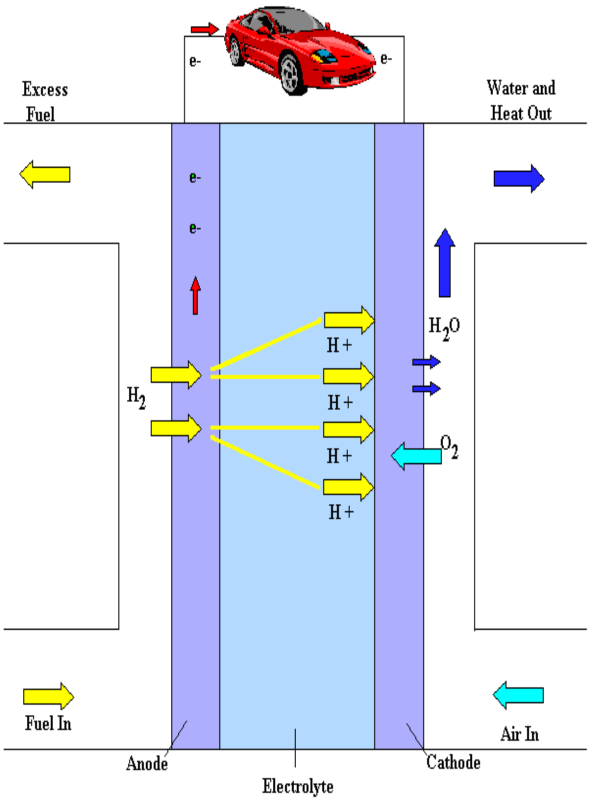

Figure 1.4. Schematic of PEM FC (a).

(a)→ Adapted from http://www.eere.energy.gov/hydrogenandfuelcells/fuelcells/fc_types.html

1.2.4 Molten Carbonate Fuel Cell (MCFC)

Molten carbonate fuel cells use a eutectic mixture of lithium, sodium and/or potassium carbonate as the electrolyte. These fuel cells operate at much higher temperatures approximately 650^{o} C (EG&G Technical Services, 2002). MCFC's have a very high fuel to electricity efficiency, approximately 60%. This efficiency can be increased to as much as 85% when cogeneration is employed (Larminie and Dicks, 2003). Since the MCFC operates at high temperature, noble metal catalysts are not needed for the electrochemical oxidation and reduction reactions. Nickel alloy is commonly used as the catalyst for the anode, while nickel oxide is used as the cathode catalyst (EG&G Technical Services, 2002). The high operating temperature is advantageous because different types of fuels can be employed including natural gas, gasoline, propane, simulated gasification products, and carbon monoxide containing fuels from gasified coals, biomass, or landfill gas. The primary disadvantages of molten carbonate fuel cells are the enhanced corrosion and the degradation of cell components due to the high temperature (Larminie and Dicks, 2003). The primary applications of these fuel cells are in stationary applications, such as power plants. The following reactions occur in the molten carbonate fuel cell (Larminie and Dicks, 2003):

$$\text{Anode: } H_2 + CO_3^{2-} \rightarrow H_2O + CO_2 + 2e^- \qquad (1.2.4.1)$$

$$\text{Cathode: } \frac{1}{2}O_2 + CO_2 + 2e^- \rightarrow CO_3^{2-} \qquad (1.2.4.2)$$

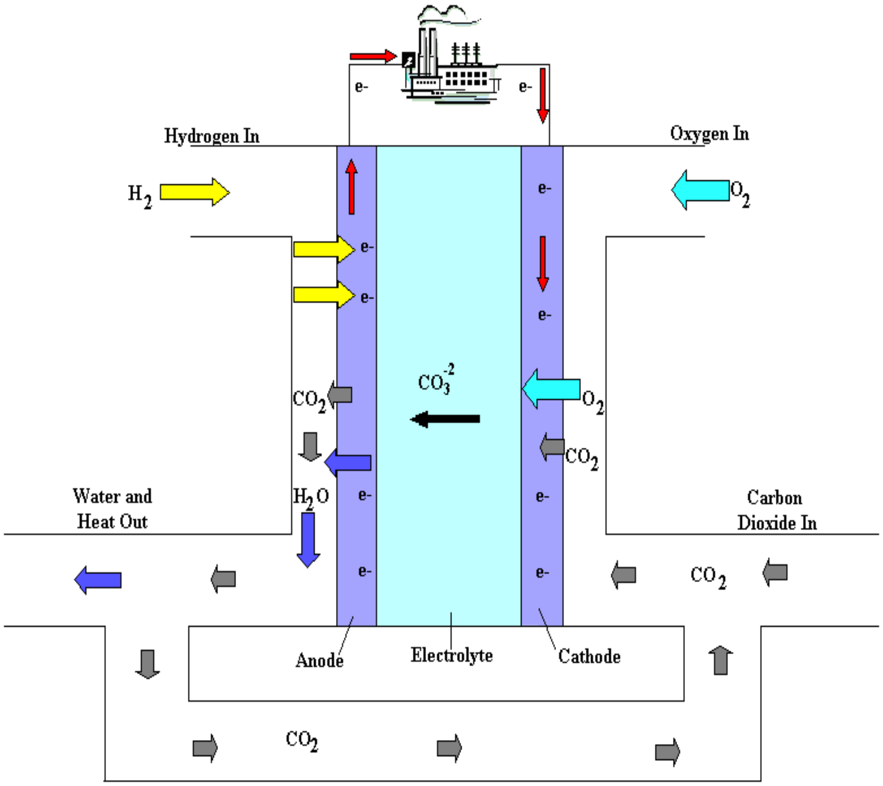

Figure 1.5. Schematic of MCFC (a).

(a)→ Adapted from http://www.eere.energy.gov/hydrogenandfuelcells/fuelcells/fc_types.html

1.2.5 Solid Oxide Fuel Cell (SOFC)

In the solid oxide fuel cell, the electrolyte composed of zirconium oxide, stabilized with a small amount of ytrria (Larminie and Dicks, 2003). Use of this hard ceramic material, instead of a liquid electrolyte, allows operating temperatures of up to 1000° C to be achieved. The high temperature increases the oxygen reduction reaction (ORR) kinetics at the cathode, leading to improved performance as well as the ability to use less expensive catalysts. This type of fuel cell can be used in high-power applications including industrial and large-scale central electricity generating stations and auxiliary power units. The primary technical challenges facing commercialization of SOFCs are the development of low cost materials that can withstand the high operating temperatures and improvement in performance at the lower temperatures (EG&G Technical Services, 2002). The following reactions occur in the SOFC (EG&G Technical Services, 2002).

$$\text{Anode: } H_2 + O^{--} \rightarrow H_2O + 2e^- \qquad (1.2.5.1)$$

$$\text{Cathode: } \frac{1}{2}O_2 + 2e^- \rightarrow O^{--} \qquad (1.2.5.2)$$

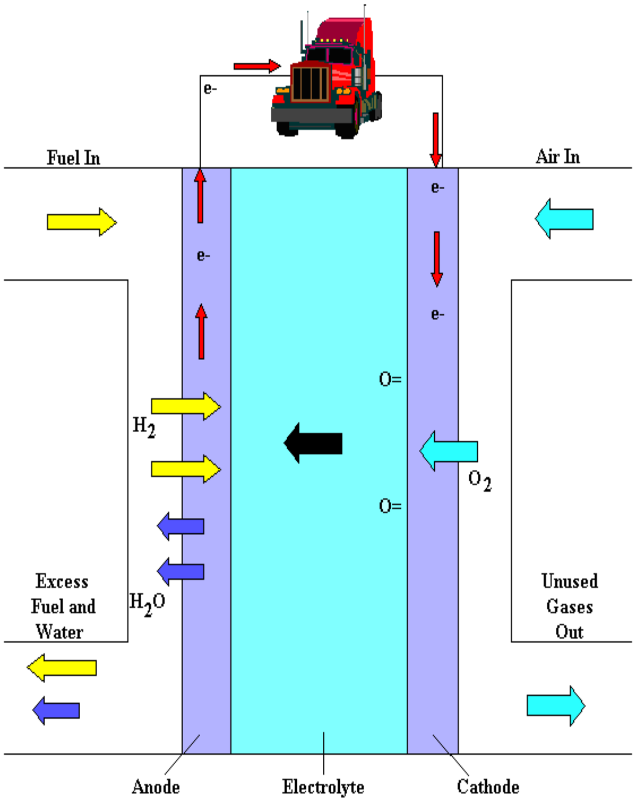

Figure 1.6. Schematic of SOFC [a].

[a] → Adapted from http://www.eere.energy.gov/hydrogenandfuelcells/fuelcells/fc_types.html

1.2.6 Direct Methanol Fuel Cell (DMFC)

Direct methanol fuel cells are similar to PEM fuel cells in that both use a polymer membrane as the electrolyte. The operating temperature of direct methanol fuel cells is between 50 to 100^{o} C (EG&G Technical Services, 2002). This makes the DMFC, attractive for small power applications including laptop computers and cellular phones among others. Since this fuel cell operates on liquid methanol as fuel, the infrastructure needed to supply the fuel to automobiles is essentially in place (EG&G Technical Services, 2002). Additionally, the on-board fuel supply system is much simpler.

Problems with methanol crossover from the anode to the cathode and high over potentials still inhibit the performance of these fuel cells. The reactions taking place in the DMFC are given in equations (1.2.6.1) and (1.2.6.2) (Larminie and Dicks, 2003). The anodic reaction results in the production of carbon dioxide, a greenhouse gas.

$$\text{Anode:}\quad CH_3OH + H_2O \rightarrow CO_2 + 6H^+ + 6e^- \qquad (1.2.6.1)$$

$$\text{Cathode:}\quad 6H^+ + 6e^- + \frac{3}{2}O_2 \rightarrow 3H_2O \qquad (1.2.6.2)$$

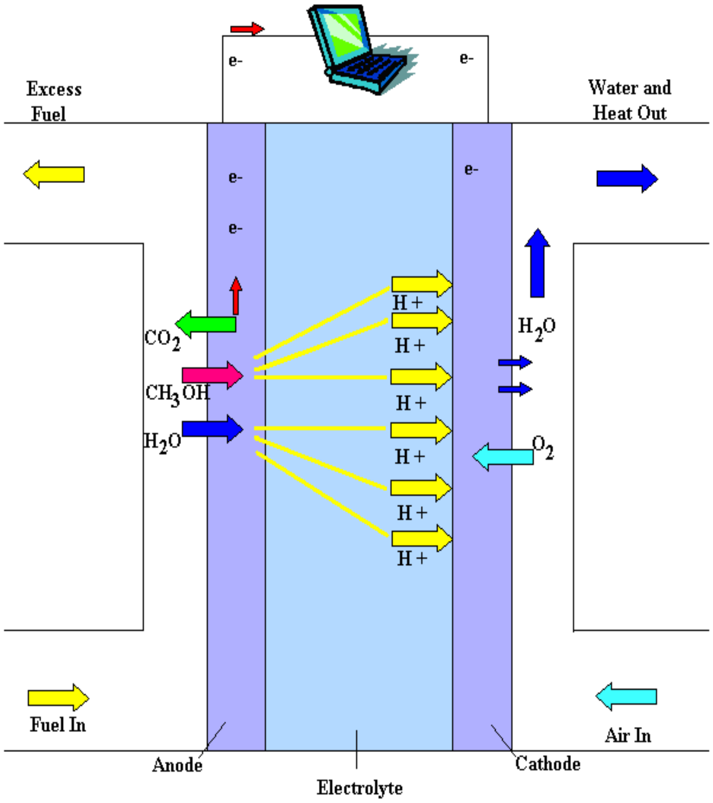

Figure 1.7. Schematic of DMFC.

Other types of fuel cells have also been studied more recently and include: Regenerative Fuel Cells, Zinc-Air Fuel Cells, and Protonic Ceramic Fuel Cells. Table 1.1 summarizes the main features of the various types of fuel cells discussed in this chapter.

Table 1.1. Main Features of Different Types of Fuel Cells.

Type of Fuel cell	PAFC	AFC	PEMFC	MCFC	SOFC
Electrolyte[a]	Immobilized liquid phosphoric acid	Potassium hydroxide	Solid polymer membrane	Alkali carbonates	Ceramic oxide
Mobile ion[a]	H^+	OH^-	H^+	CO_3^{2-}	O^{2-}
Operating temperature (^{o} C)[b]	~220	80-200	30-100	~650	500-1000
Catalyst[b]	Platinum	Nickel	Platinum	Nickel	Perovskites
Anode gas[b]	Hydrogen	Hydrogen	Hydrogen	Hydrogen, methane, etc	Hydrogen, methane, etc
Cathode gas[b]	Air or oxygen	Pure oxygen	Pure oxygen or air	Air or oxygen	Air or oxygen
Efficiency (%)[b]	40-50	45-60	40-60	50-60	50-65
Reformer[a]	External	External	External	External or internal	External or internal
Product water management[a]	Evaporative	Evaporative	Evaporative	Gaseous product	Gaseous product
Start-up time[a]	Hours	Min	Sec-min	Hours	Hours

[a] EG&G Technical Services, 2002
[b] Larminie and Dicks, 2003

1.3 Advantages of Fuel Cells

Fuel cells have many characteristics that make them an attractive alternative to conventional energy conversion systems.

- **Efficiency:** Since fuel cells convert the chemical energy contained in fuels directly into electrical energy, their efficiencies are not limited by the Carnot limit. Efficiencies of present fuel cell plants are in the range of 40 to 55 %

(Larminie and Dicks, 2003). Hybrid fuel cell/gas turbine cycles have demonstrated efficiencies greater than 70% (Larminie and Dicks, 2003). Even at low load, efficiencies are not affected. This makes fuel cells suitable for applications such as automobiles, where good efficiencies are required at low loads.

- **Low (near zero) emissions:** If pure hydrogen gas is used as fuel, only water and heat are produced as products and no pollutants are produced. However, hydrogen produced by reforming hydrocarbon fuels results in the generation of NO_x, SO_x, CO and CO_2 (EG&G Technical Services, 2002). The amount of carbon dioxide produced is significantly lower when compared to conventional combustion engines, operating on conventional gasoline fuel.
- **Scalability**: Fuel cells can be configured to meet the needs of a wide range of power applications, ranging from a few watts to megawatts (EG&G Technical Services, 2002). Thus fuel cells are expected to serve as the power source for portable computers as well as vehicles or large power plants in the future.
- **Fuel flexibility**: Fuel cells can be operated using commonly available fuels such as natural gas, methanol, and various complex hydrocarbons (EG&G Technical Services, 2002).
- **Reliability and low maintenance:** Since no moving parts are involved in the operation of the fuel cell, maintenance requirements and system downtime are minimized.
- **Quiet operation.**

1.4 Objective of Thesis

The development of a one-dimensional model of the proton exchange membrane fuel cell is one objective of this thesis. An essential element of the model is the description of the various components in the fuel cell. Thus, the second primary objective of the thesis is the characterization of gas diffusion layer using physisorption, SEM, capillary flow porometry, and mercury/non-mercury intrusion porosimetry.

CHAPTER II

PROTON EXCHANGE MEMBRANE FUEL CELL

The Proton Exchange Membrane fuel cell is also known as the Solid Polymer fuel cell and/or Polymer Electrolyte (PEM) fuel cell. PEM fuel cells have high power density (2.6 to 3.8 kW/m^2), and an electrical efficiency of 45 to 60%(fuel cell stack), resulting in a low weight, low volume and competitive alternative for mobile and stationary applications. The electrolyte is an ion-conducting polymer, which simplifies sealing, assembly and handling problems and also reduces corrosion. The PEM fuel cell operates at low temperatures. The advantage of operating at low temperatures is that startup is faster and the fuel cell can respond immediately to changes in the demand for power. The primary disadvantage of operating at low temperature is carbon monoxide poisoning of the electro-catalyst particles. At low temperature, carbon monoxide can chemisorb onto the platinum (Pt) catalyst particles, thereby reducing the number of sites available for the desired reaction, resulting in decreased power generation. In this chapter, a complete description of the PEM fuel cell, the components of the PEM fuel cell, and its applications are presented. A review of the available literature is also provided.

2.1 PEM Fuel Cell

A schematic representation of a PEM fuel cell is shown in Figure 2.1.

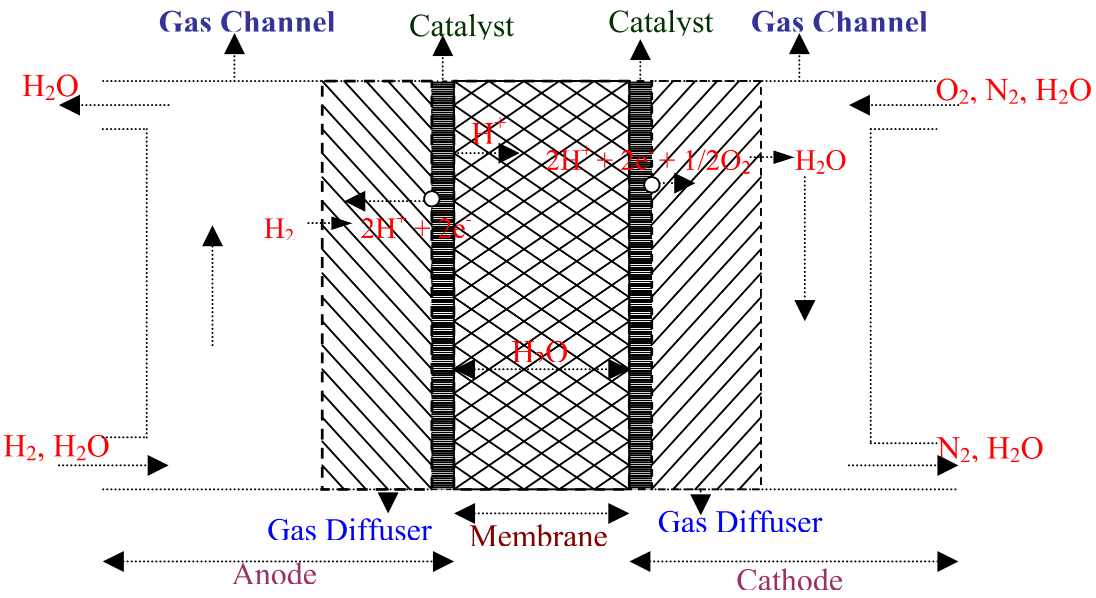

Figure 2.1. Schematic Representation of PEM Fuel Cell (EG&G Technical Services, Inc, 2002).

Fuel (hydrogen) is fed continuously to the anode and an oxidant (air, oxygen) is fed continuously at the cathode. The electrochemical reactions take place at the electrodes. Each electrode is divided into three regions: gas channel, gas diffuser and active catalyst layer. These regions are also shown in Figure 2.1. The PEM fuel cell is divided into seven distinct regions. Hydrogen from the anode gas channel diffuses through the gas diffusion layer to the active catalyst layer where the oxidation reaction (equation (2.1.1)) takes place:

$$2H_2 \rightarrow 4H^+ + 4e^- \tag{2.1.1}$$

Protons (H^+ ions) then migrate through the membrane to the cathode side. Electrons (e^-) are transported through the external load to the cathode catalyst layer where the reduction reaction takes place, equation (2.1.2).

$$O_2 + 4H^+ + 4e^- \rightarrow 2H_2O \tag{2.1.2}$$

The overall reaction is:

$$2H_2 + O_2 \rightarrow 2H_2O \tag{2.1.3}$$

2.2 Polarization Curve

The ideal potential of the H_2/O_2 fuel cell is approximately 1.229V at 25° C. The actual potential is lower than the ideal value because of overpotential losses, as shown in

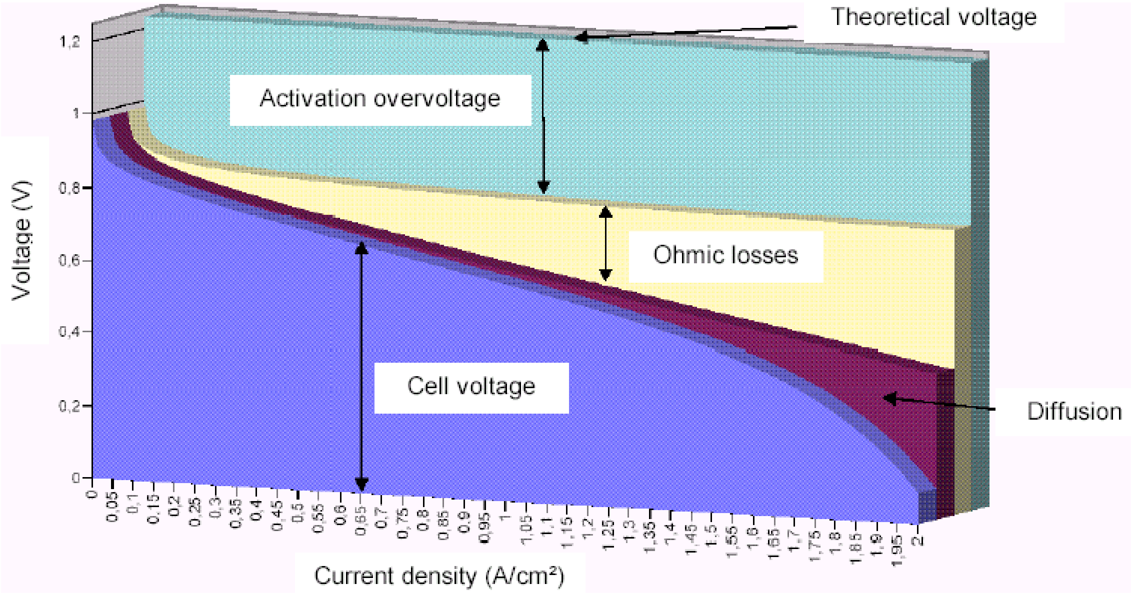

Figure 2.2. Polarization Curve of PEM Fuel Cell (Pascal, 2003).

Figure 2.2. As indicated in Figure 2.2, there are three types of overpotential losses, which result in decreased cell potential. These losses are:

1. Activation overpotential (η_{act});
2. Ohmic overpotential (η_{ohm}); and
3. Concentration overpotential (η_{con}).

Activation overpotential (η_{act}) is caused by the slowness of the reactions taking place at the interface between the electro catalyst and the membrane. A portion of the voltage generated is lost in driving the chemical reaction that transfers electrons to or from the electrodes. The cathode exchange current density is five to six times lower than the anode exchange current density. Using catalysts with lower activation resistance and increased effective catalyst surface area available for reaction per unit volume of electrode can lessen this overpotential.

Ohmic overpotential (η_{ohm}) is the loss due to the resistance to the flow of electrons through the electrodes and various interconnects and also due to the resistance to the flow of ions through the electrolyte. This loss is proportional to the current density and is also known as the resistive loss. This loss can be reduced by using humidified gases, using thinner membranes, and/or membranes with lower ionic and water transport resistances.

Concentration overpotential (η_{con}) is the loss due to the change in the concentration of reactants at the surface of the electrodes as the reactants are used. These losses occur due to the depletion of the reactant gases at the reaction interface. This overpotential is severe on the cathode side of the cell not only due to the reduction in oxygen concentration as it is consumed by the reaction, but also because oxygen must be transported through the water barrier created by the cathode reaction products (water). Proper water management and properly designed gas distribution channels are important factors to minimize the impact of concentration overpotential.

2.3 Main Components of PEM Fuel Cell

This section provides a description of the main components of the PEM fuel cell and also discusses their characteristics and functions. A schematic of a single PEM fuel cell is shown in Figure 2.3 (Shimshon, 2000).

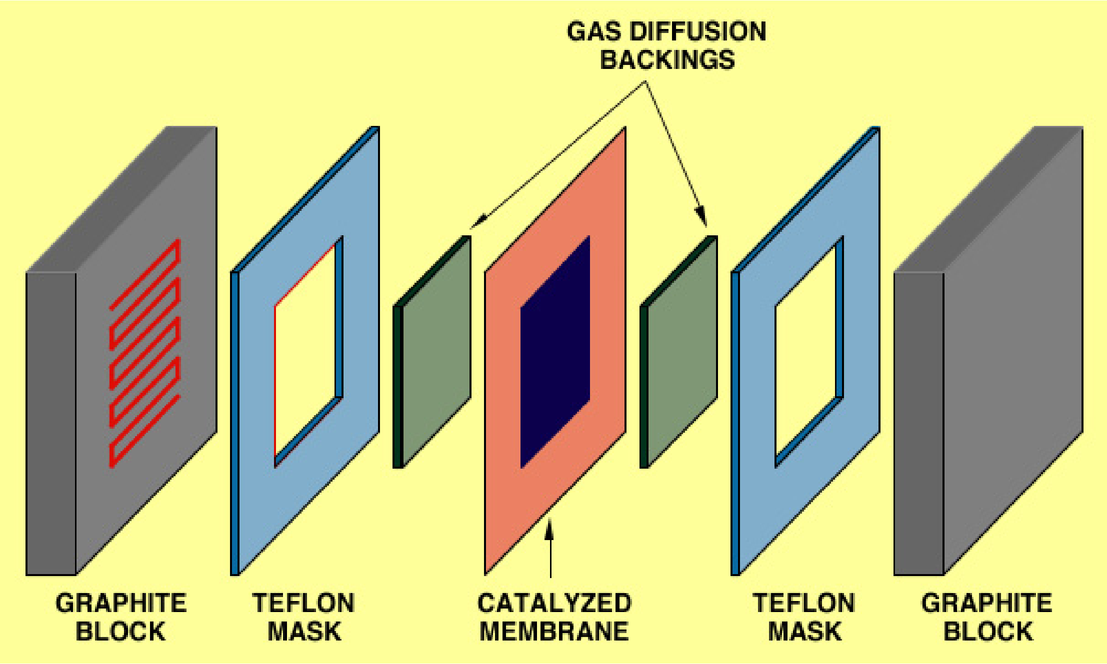

Figure 2.3. Schematic of Single Cell Hardware (Shimshon, 2000).

The main components of the PEM fuel cell are:

1. Ion exchange membrane
2. Porous backing layer
3. Electrode-catalyst layer
4. Cell plate hardware

2.3.1 Proton Exchange Membrane

In 1959, William T. Grubbs (1955) conceived the idea of using an ion exchange membrane in a fuel cell. The main function of the ion exchange membrane is to provide a conductive path for the protons while acting as an insulator to the electrons. The membrane should also prevent the fuel and oxidant from directly mixing with one another. Presently, the most widely used proton exchange membrane is the Nafion membrane. Nafion has a Teflon like structure. The structure of the Nafion membrane is shown in Figure 2.4 (James et al., 2000).

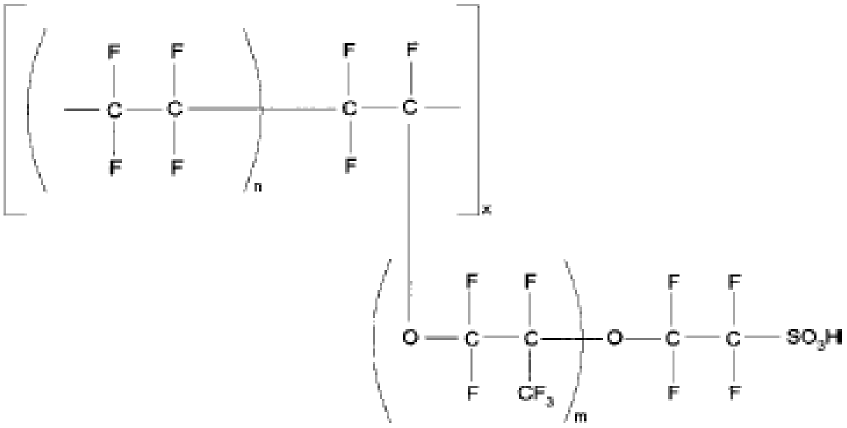

$$C_{(2n+3m+4)}F_{(4n+6m+7)}O_{(m+4)}SH$$

Figure 2.4. Structure of Nafion.

Nafion is perfluorosulfonic acid polymer. This material has played a very important role in the development of the PEM fuel cell. Nafion is durable (Larminie and Dicks, 2003) and resistant to chemical attack due to presence of strong bonds between the fluorine and the carbon atoms. The presence of the fluorocarbon matrix makes Nafion hydrophobic (Uan-Zo-Li, 2001). Due to the presence of sulphonate ions, Nafion is strongly hydrophilic and as a result, can absorb water. When membrane is well hydrated, protons can move freely within the membrane. The most important properties of the membrane are strongly influenced by the water content. Nafion cannot be used at temperatures higher than 100^{o} C because its glass transition temperature is only 111^{o} C (Yeo and Eisenberg, 1977).

2.3.2 Porous Backing Layer

The main function of the backing layer is to act as a gas diffuser and to provide a pathway for the electrons from the reaction sites. The backing layer is typically made from carbon-based materials including carbon-cloth, carbon fibers, and carbon papers. The backing layer should be porous in order to allow gases to diffuse through the pores to the sites where the electrochemical reactions take place. It should also possess high electrical conductivity to transport electrons, be mechanically strong, and be resistant to acidic medium and humidity. In order to facilitate the diffusion of gases, this layer is made partially hydrophobic by treating it with Polytetrafluoroethylene (PTFE), so that water is repelled from the pores. This allows the gases to more easily reach the sites on the surface.

2.3.3 Electrode-Catalyst Layer

The electrocatalyst layer is sandwiched between the backing layer and the membrane. Typically, the catalyst particles are deposited on the carbon electrode. The important characteristics of the electrode are low resistivity, large electrochemical active area, mechanical strength, inert and act as a catalyst support, and should be porous enough to provide reactant gases to the reaction sites. A schematic of a typical carbon-supported catalyst is shown in Figure 2.5 (Larminie and Dicks, 2003).

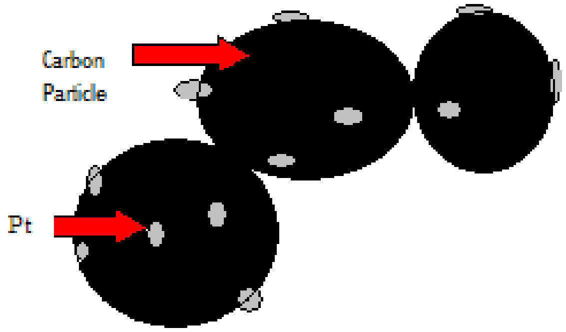

Figure 2.5. Structure of Carbon-Supported Catalyst.

The electrochemical reactions in the fuel cell take place at active sites on the catalyst. In the fuel cell, the catalyst must be in intimate contact with both the electrolyte and the backing layer. This contact allows efficient transfer of protons and electrons produced at the reaction sites.

2.3.4 Cell Plate Hardware

The cell plate, shown in Figure 2.3, is a double-sided configuration and delivers the fuel and the oxidant to the reaction sites via flow channels. These plates are also known as bipolar plates. The main function of these plates is to distribute the reactant gases evenly over the surface of the anode and the cathode. The bipolar plates must also maintain good electrical contact with the surface of the electrodes in the PEM fuel cell stack. The channels in the flow field plates are very small, typically less than 1 mm in width and in height. Pressure drop in the flow field plates must be maintained above the surface tension of water so that the channels are not blocked by liquid water. This ensures smooth passage of the reactant gases through the channel. It should also prevent the reactant gases and the cooling fluids from mixing with one another. The geometry of the machined flow field pattern affects the performance of the PEM fuel cell, especially with respect to water management and distribution of the reactant gases. The requirements for the flow field plates include:

- High electrical and thermal conductivity;
- Minimum gas permeability;
- Good mechanical strength;
- Corrosion resistant to acids, O_2, H_2, heat, and humidity;
- Slim and light weight;
- Low cost.

Solid graphite is the most commonly used material for the flow field plates. Since graphite is expensive in terms of both material cost and manufacturing cost, a significant amount of research is directed towards finding a cheaper material with lower production costs. Various configurations for the flow channels are shown in Figure 2.6 (Larminie and Dicks, 2003).

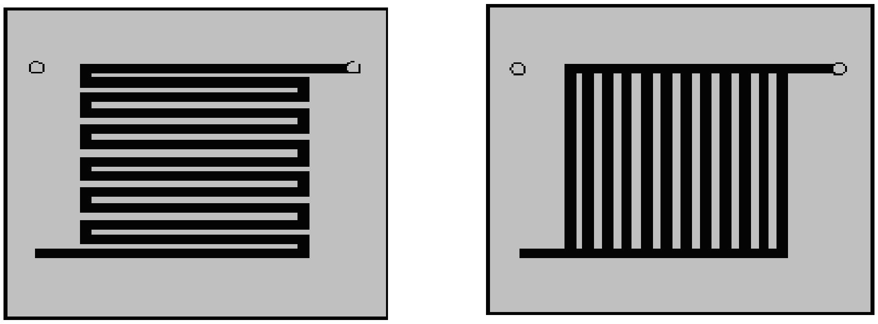

(a) Serpentine

(b) Parallel

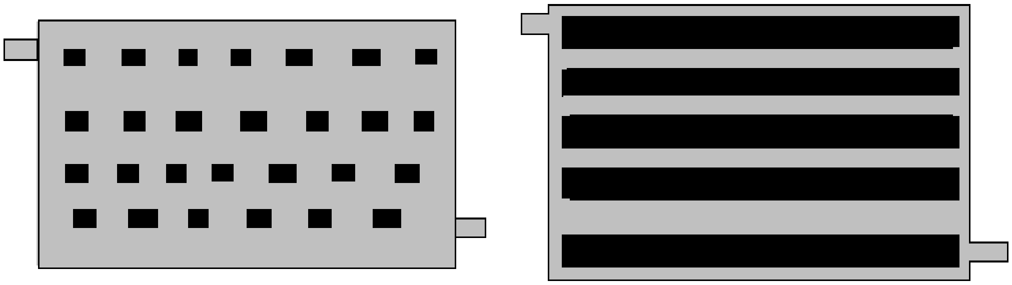

(c) Grid

(d) Long Parallel

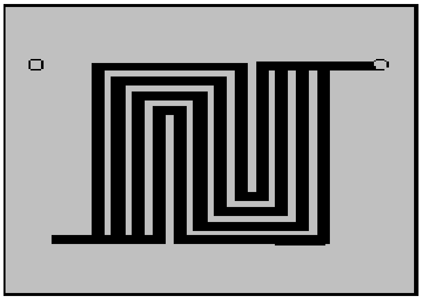

(e) Parallel Serpentine

Figure 2.6. Different Types of Flow Field Plates.

2.4 Characteristics and Applications of PEM Fuel Cells

PEM fuel cells have many characteristics that make them efficient energy conversion devices. The primary advantages of the PEM fuel cell that have generated interest among researchers are its relatively high efficiency and its very low (near zero) environmental emissions. The efficiency of the PEM fuel cell is not limited by the Carnot efficiency as in an internal combustion engine. Efficiencies of present-day PEM fuel cells are in the range of 35 to 50%. If fuel cells are used in conjunction with cogeneration systems, then efficiencies can be improved to approximately 70% (EG&G Technical Services, Inc; 2002). Since the efficiency of a fuel cell is independent of size, small fuel cell plants operate nearly as efficiently as large ones (Larminie and Dicks, 2003). Thus, fuel cells can be used for a wide range of applications requiring very different power outputs, from watts to mega watts. The primary advantages of the PEM fuel cell are:

- Direct energy conversion;
- Low temperature operation;
- Flexibility of scale;
- Noise-free operation;
- No moving parts;
- Fuel flexibility (even with hydrogen derived from hydrocarbon fuels, levels of pollutants produced are very low);
- Minimum maintenance.

The main applications of PEM fuel cell are stationary electric power plants and portable power for vehicles.

2.5 Literature Survey

Much of the current research effort in fuel cell modeling has focused on developing models that address the performance issues of the PEM fuel cell. In this section, a brief overview of existing models, drawn from the literature, is presented.

Fuller and Newman (1993) developed a two-dimensional Membrane Electrode Assembly (MEA) model for the PEM fuel cell. They considered an MEA operating at steady state with air as oxidant and reformed methanol as fuel. Fuller and Newman assumed that the fuel and air streams were heated before the reactants enter their respective flow channels. In their model, Fuller and Newman considered thermal management, water management, and utilization of fuels along the channels. Their analysis mainly focused on the transport of water through the membrane since the conductivity of the membrane is a strong function of water content. They assumed that oxidation of hydrogen and evaporation/absorption of water occurred rapidly. They applied concentrated solution theory, which states that the driving force for species transport is proportional to the dynamic motion of the species. Their model predicted that equilibrium sorption of water between the gas phase and the electrolyte depended on temperature, water and thermal management. They concluded that adequate heat removal was essential to prevent membrane dehydration and maintain high performance of the PEM fuel cell. They also concluded that cell performance was improved when gas streams were saturated with water at a temperature above the operating temperature of the fuel cell.

Verbrugge and Hill (Verbrugge, 1989; Verbrugge and Hill, 1990) developed a mathematical model for ion (protons) and solvent (bisulfate ions) transport within an ion-exchange membrane. They used the Nernst-Planck equation to describe the diffusion, migration, and convection of ions through the polymer electrolyte membrane. Verbrugge and Hill employed the dilute solution theory for ion transport, by assuming that the concentration of ions was much lower than the solvent concentration. Each proton was assumed to be attached to a single fixed charge. They concluded that if no current was passed, the diffusion coefficients of the proton (H^+) and bisulfate (HSO_4^-) ions were not equal and diffusion potential resulted from the concentration gradients in the membrane. Since no current was passed, the diffusion potential caused both proton and bisulfate ions to transport at the same rate. They also performed experimental work to determine the water and proton transport characteristics of perfluorosulfonic acid membranes and Dow membranes using electroanalytical and radiotracer experimental techniques (Verbrugge and Hill, 1990). From electroanalytical experimental results, they concluded that the effective membrane conductivity decreased with increasing membrane thickness and that the Dow membrane showed lower resistance than the Nafion membrane of the same thickness. From radiotracer experiments, they observed that the Dow membrane yielded lower fluid transport rates and diffusion coefficients, compared to the Nafion membrane.

Springer (Springer et al., 1991) presented an isothermal, one-dimensional, steady state model for the PEM fuel cell. The proton exchange membrane was modeled as a Nafion 117 membrane. In their model, they incorporated measurements obtained in their laboratory as a function of the water content of the membrane. These incorporated measurements included: water diffusion coefficients, electro-osmotic coefficients, water sorption isotherms, and membrane conductivities. Their model included transport through the porous electrodes, based on calculated diffusivities, and transport through the membrane electrolyte, based on experimentally determined parameters. They assumed equilibrium existed between membrane water and electrode water vapor at the membrane/electrode interface. They considered the electro-osmotic drag and diffusion driving forces for water in the membrane and diffusion for water vapor and reactant gases in the electrodes to obtain the mass balance in the cell. Their model predicted that membrane resistance increased with increasing current density. They also provided key parameters for the membrane including: the water diffusion coefficient, proton conductivity, and electro-osmotic drag as a function of the water content of the membrane. In this pseudo one-dimensional model, Springer et al. assumed that the gases in the flow channels were well mixed. They also studied the air cathode characteristics in the PEM fuel cell using impedance spectroscopy (Springer et al., 1996). They also determined the amount of water uptake by membranes immersed in liquid water and by membranes exposed to different water vapor levels at 30^{o} C (Springer et al., 1993a).

Nguyen and White (Nguyen and White, 1993) developed a steady state, two-dimensional heat and mass transport model for the PEM fuel cell that accounted for variations in temperature and membrane hydration along the length of the flow channels. The primary focus of this effort was to investigate the effectiveness of various humidifier designs for maintaining high membrane hydration and performance for PEM fuel cell. Their model accounted for water transport across the membrane by electro-osmosis and by diffusion, heat transfer from the solid phase to the gas phase, and the latent heat effects of water evaporation and condensation in the flow channels. Results from their model showed that back diffusion of water from the cathode to the anode was not sufficient to keep the membrane hydrated at high current densities. This increased the ohmic losses. They concluded that the anode gas must be humidified. They also concluded that the cathode stream must also be humidified when air is used instead of oxygen at the cathode. Their model assumed that the temperature of solid phase was uniform and constant.

Nguyen (Nguyen, 1996) proposed a non-conventional gas distribution design to improve the mass transport rates of the reactants from the flow channels to the inner catalyst layers of the porous electrodes and to reduce the electrode water flooding problem in the cathode of the PEM fuel cell. In this design, the inlet and outlet channels were dead-ended. Thus, reactant gases were forced to flow into the porous electrodes to exit. In his model, he replaced the diffusion mechanism of reactant gases with a convection mechanism to describe the transport of the reactant and product gases from the catalyst layers. This resulted in a much reduced gas-diffusion layer over the catalyst sites. This design also helped to remove the liquid water condensed in the inner layers of the electrodes, thereby reducing the electrode flooding problems. With this design, Nguyen observed that the mass-transport-limited region was significantly extended. The new flow field design resulted in increased current densities and power densities due to the enhanced convective flow and the water removal from the porous electrodes.

Nguyen and Yi (1998) developed a model to describe mass and thermal conditions in both the solid phase and the gas phases along the flow path of both the anode and the cathode sides of a PEM fuel cell. This model was based on the earlier model developed by Nguyen and White (1993). The Yi and Nguyen model is a two dimensional, steady state model. Plug-flow conditions in the flow channels were assumed and pressure drop along the flow channels was neglected. Their model incorporated the convective water transport from the cathode to the anode of the fuel cell due to the differential pressure (the difference between the anode and the cathode gas pressures). Results of their model showed that humidification of the anode gas increased the membrane conductivity and that application of higher cathode gas pressure helped to reduce the water loss by electro-osmosis, thereby increasing cell performance. They also found that a counter flow heat exchanger was more effective than either a cocurrent flow heat exchanger or a constant bulk temperature scheme.

Nguyen and Yi (1999) also investigated the hydrodynamics of gases in the cathode of a PEM fuel cell. They incorporated an interdigitated gas distributor using a multi component transport model. They used a two dimensional, steady state, isothermal model of a porous electrode to simulate the hydrodynamics of gas flow through the pore volume of the electrode in the cell. Yi and Nguyen assumed that the water in the electrode existed as vapor only and also that the porous electrode layer was a homogeneous phase with uniform morphological properties such that the effective diffusion coefficient was independent of position. Results from this model showed that the diffusion of reactant gases plays a significant role in determining the cell performance. They also concluded that higher gas flow rates through the electrodes increased the cell performance. The average current density decreased with an increase in the electrode thickness and an increase in the width of the gas distributor. However, their model did not consider the effect of liquid water.

Bernardi and Verbrugge (Bernardi and Verbrugge, 1991; Bernardi and Verbrugge, 1992) developed a macro-homogeneous mathematical model of the PEM fuel cell. They applied their model to simulate an oxygen electrode bonded onto the membrane of a PEM fuel cell. They included both electro-osmotic and pressure driven water transport within the PEM fuel cell. They considered isothermal conditions and also assumed gases to be ideal and well mixed. Bernardi and Verbrugge also assumed that the total gas pressure within the gas diffuser was constant and that the gas phase in the gas diffuser was in equilibrium with the liquid water phase. They investigated the limiting factors of cell performance, the effect of porosity of the electrodes, and the effect of membrane properties. They used hydraulic permeabilities for both the membrane and the electrodes. Results from their model showed that, at low current densities (<100 mA/cm^2), the potential dropped rapidly due to the activation overpotential of the oxygen reduction reaction. At higher current densities, the potential dropped almost linearly with increasing current density, due to the greater influence of potential drop through the membrane. Their model also suggested that only a small portion of the active catalyst layer was utilized due to dissolved oxygen transport limitations. Since they assumed that the membrane was fully hydrated, they found that there was no need for external water humidification at operating current densities, since the water produced at the cathode was sufficient to satisfy the water requirements of the membrane. Their model also predicted that the volume fraction of the cathode (cathode gas porosity) available for gas transport should be at least 25% in order to avoid low limiting current densities. They also concluded that lower platinum loadings could achieve the same performance as higher platinum loadings, provided that the catalyst was optimally located. This means that the catalyst should be distributed to give more active sites for the electrochemical reaction. Their model was tested by comparison with experimental cell polarization curves, in the current density ranges of 0-1 A/cm^2.

Springer et al. (1993b) considered a detailed model of losses in the cathode of the PEM fuel cell. To study the cathode losses, they fitted their model to measured polarization curves that were iR-corrected. They measured the high frequency resistance of the PEM fuel cell at each current density along the polarization curve to determine iR-losses. They considered a composite catalyst layer, made of Pt/C/ionomer, containing uniformly distributed Pt/C catalyst well mixed with ionomer. They also assumed that the thicknesses of the catalyst layer and of the backing layer were fixed and uniform and that electronic conductivity losses within the catalyst and within the backing layer were negligible. In their model, Springer and coworkers considered the following factors: 1) losses caused by the rate of the oxygen reduction reaction at the Pt/ionomer interface; 2) limited oxygen permeability and ionic conductivity within the catalyst layer; and 3) the drop in oxygen concentration along the air/O_2 flow channels. Their experimental results showed that the overall loss of the cell was the sum of a high frequency loss (ionic and contact loss) and the voltage loss at the cathode in a well-humidified PEM fuel cell operating with pure hydrogen. For a well-humidified H_2/air PEM fuel cell, their model predicted the effect of the gas-phase transportation limitations in the cathode-backing layer on the limiting current and also on the slope of the polarization curve in the medium current densities range. The accuracy of their model depended on the effective representation of the oxygen reduction reaction.

Um et al. (2000) developed a transient, multidimensional model to simulate operation of a PEM fuel cell. The main objective of their work was to develop a model for electrochemical kinetics, current distribution, fuel and oxidant flow, and multi component transport for a realistic fuel cell using a finite-volume-based, Computational Fluid Dynamics (CFD) approach. They also studied the effect of diluted hydrogen gas on the PEM fuel cell running on reformate gases. Their model assumed that gases obeyed the ideal gas law, and that the electrodes, catalysts layers, and membrane were both isotropic and homogenous. They assumed constant temperature operation and negligible ohmic potential drop in the electronically conductive solid matrix of porous electrodes, catalyst layers, and current collector plates. They used Henry's law to account for the oxygen concentration difference between the liquid and the gas phase. Their results showed that the presence of liquid water in the membrane altered its ionic conductivity and the liquid water in the gas diffusion electrode decreased the oxygen transport to the catalyst layers. They showed that hydrogen dilution at the anode led too much lower cell current densities, due to the limitation of diffusive transport of hydrogen at the reaction site. Their model also predicted detailed reactant and product distributions inside the cell. However, their model only considered a single phase of water and was unable to predict the concentration overpotential at the cathode.

Wang et al. (2001) analytically and numerically studied the two-phase flow and transport of reactants and products in the air cathode of the PEM fuel cell. They assumed that the cell operated at constant temperature and that the gas phase was an ideal gas mixture. They treated the catalyst layer as a thin surface and assumed that the gas diffusion electrodes were isotropic and homogenous. They observed that the liquid water and vapor transport were controlled by capillary action and molecular diffusion, due to negligibly small air velocity within the porous electrodes. They described different regimes of water transport and distribution in the air cathode of the PEM fuel cell. However, their model did not include the influence of the catalyst layer, the membrane, or the anode side.

Parthasarathy et al. (Arvind and Martin, 1991; Arvind et al., 1992a; Arvind et al., 1992b; Arvind et al., 1992c) performed experimental measurements of the concentration and diffusion coefficient of oxygen in Nafion, and the electrode kinetic parameters for the reduction of oxygen at the solid-state Pt/Nafion interface. The contact between the membrane (Nafion) and the electrode was measured by mechanical pressure, defined as the pressure applied to the electrode/membrane interface. They used cyclic voltammetry measurements to determine the purity of the Nafion based on the resolution of the platinum surface electrochemical processes and also to determine the electrochemically active surface area of the electrode. They calculated the roughness factor for the electrode by dividing the determined electrode area by the geometric area. They also measured the diffusion coefficient and solubility of oxygen in the Nafion membrane. They measured the exchange current density by extrapolating the Tafel plot to the equilibrium potential. The transfer coefficients were calculated from the slope of the Tafel plot, using slow scan voltammetric experiments. They also studied the effect of temperature and pressure on the oxygen reduction reaction. From their experimental studies, they concluded that the diffusion coefficient of oxygen in air-equilibrated Nafion membranes was lower than the diffusion of oxygen in pure oxygen-equilibrated membranes.

Dannenburg et al. (2000) proposed a two-dimensional, mass and heat transfer model for a PEM fuel cell. They considered mass transfer in the gas channels and electrode gas backings, water transport in the membrane, and heat transfer. They considered only cathode electrode kinetics and assumed the anode potential to be equal to its equilibrium value. They used an agglomerated model to describe the active catalyst layer of the cathode. They performed model simulations varying the humidity, temperature, gas composition, stoichiometric amounts of reactants, and cooling media with different heat transfer coefficients. Results from their model showed that, ohmic resistance was constant up to current densities of 0.8 A/cm^2, and then increased due to the anode dehydration. Predictions from their model showed that ohmic resistance increased with stoichiometric amounts of reactants for dry or partially humidified reactant gases due to drying of the membrane. For well-humidified reactants, they observed that better cell performance was observed at higher current densities when the stoichiometric ratio was increased from 0.7 to 2 and that cell performance was decreased when the stoichiometric ratio was increased from 2 to 3. From their model predictions, they concluded that the best performance of the fuel cell was obtained at isothermal conditions.

Gurau et al. (1998) developed a two-dimensional model for the PEM fuel cell. They considered the equations governing flow and transport in the flow channels and the gas diffuser, as well as transport equations in the catalyst layer and in the membrane. They studied the oxygen and water vapor distributions in the cathode gas channels and gas diffuser at various operating current densities. They also studied the liquid water velocity distributions in the membrane and the influence of various parameters including porosity and temperature on the performance of the fuel cell. Predictions from their model showed that the oxygen mole fraction along the gas channel-gas diffuser interface and the current density along the membrane-catalyst layer interface were not linear.

CHAPTER III

THEORY AND GOVERNING EQUATIONS

A single PEM fuel cell can be divided into seven distinct regions for modeling purposes. These seven regions are: 1) the anode gas channel; 2) the anode gas diffuser; 3) the anode catalyst; 4) the membrane; 5) the cathode catalyst; 6) the cathode gas diffuser; and 7) the cathode gas channel. The performance of the fuel cell is affected by the properties of the materials used for each of the individual components and also by the operating conditions of the fuel cell. Important material properties include: effective electrode porosity, degree of hydrophobicity, permeability of the gas diffusers, catalyst loading, membrane conductivity, and the hydration index of membrane. Important operating conditions include: temperature, pressure, gas flow rates, relative humidity, and compositions of the reactant gases. A modeling approach is adopted to study the effect of these parameters on the performance of the fuel cell.

This chapter explains the basic equations used to describe the different regions of the fuel cell. These equations are used to develop a steady state, one-dimensional, isothermal fuel cell model. The single fuel cell model is then used to study the effect of parameters on the performance of the fuel cell.

3.1 Model Description

A schematic of the cathode side of the fuel cell is shown in Figure 3.1. In this model, the system is considered to be composed of three regions.

- Membrane Region
- Active-Catalyst Region
- Gas Diffusion Layer Region

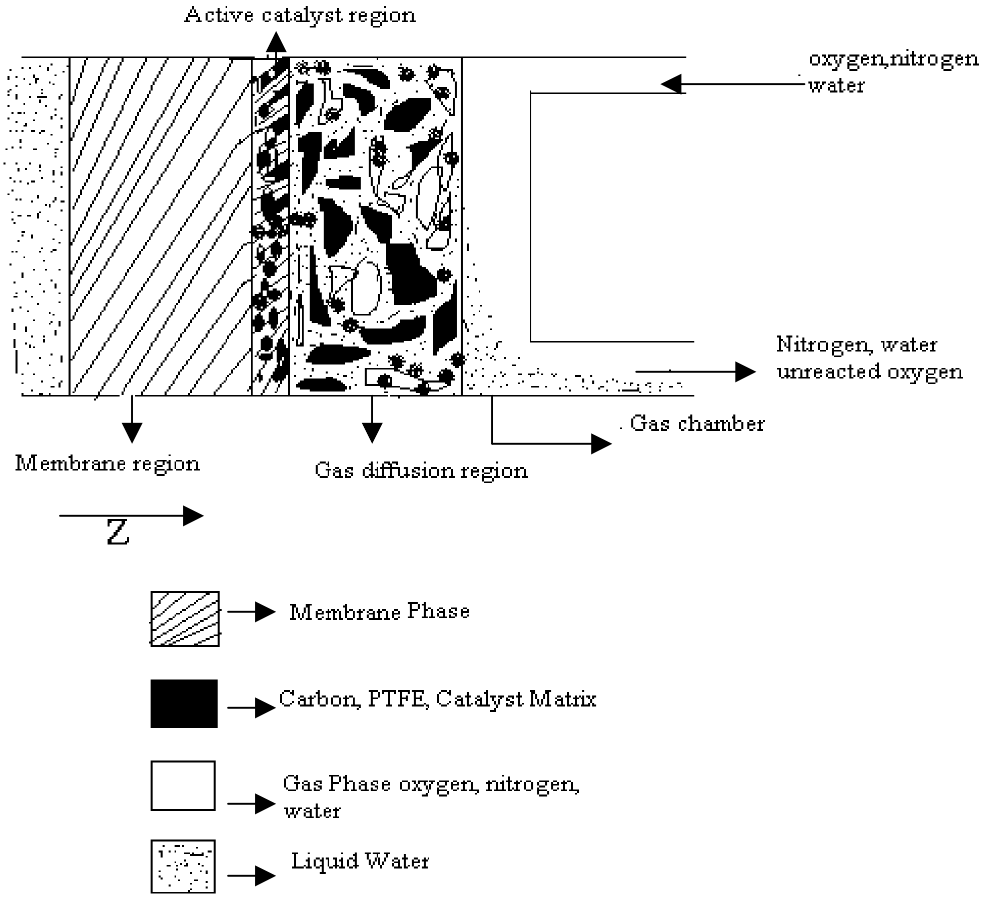

Figure 3.1. Schematic of Cathode Side of PEM Fuel Cell (Bernardi and Verbrugge, 1991).

The membrane region consists of the hydrated polymer electrolyte. The active-catalyst region is treated as a homogenous and isotropic region made by the overlapping of small particles of the membrane and the porous electrode diffusion layer (Bernardi and Verbrugge, 1991). The gas diffusion region is comprised of the gas diffusion layer, which contains the carbon backing layer and catalyst particles. The main function of the gas diffusion region is to provide a pathway for reactants to reach the catalyst sites as well as a pathway for the reaction products to exit. Therefore, it is very important that catalyst particles are loaded so that the particles are in good contact with both the ionic (polymer) and the electronic (solid particles) conductors. In the active-catalyst region, dissolved gaseous reactants (oxygen) contact ions from the membrane and the electrochemical reaction takes place at the catalyst sites (Bernardi and Verbrugge, 1991). Three types of species are transported in the gas diffusion region (Bernardi and Verbrugge, 1991). These are:

- Electrons move through the electronically conductive portion of the carbon and platinum particles.
- Gases are transported through the pores of the electrodes.
- Liquid water is transported through the channels.

The fuel and oxidant gases enter through the flow field channels on the anode side and the cathode sides, respectively. Hydrogen gas (fuel) enters the anode gas chamber and is transported through the porous gas diffuser region and reaches the active catalyst layer. In the active catalyst region, the hydrogen gas is oxidized, releasing protons and electrons. The membrane phase of the active catalyst layer transports the protons to the cathode catalyst region. The electronically conductive electrode transports the electrons to the external load. The overall electrochemical reaction taking place at the anode catalyst layer is shown in equation (3.1.1).

$$H_2 \leftrightarrow 4H^+ + 4e^- \qquad (3.1.1)$$

Similarly, the gaseous oxygen enters the cathode gas chamber and diffuses through the diffuser to the membrane phase of the cathode catalyst layer. In the cathode catalyst layer, the oxygen is reduced by reacting with protons and electrons to form water, as shown in equation (3.1.2).

$$O_2 + 4H^+ + 4e^- \leftrightarrow 2H_2O \qquad (3.1.2)$$

3.2 Model Assumptions

The following assumptions have been made during model development.

- One-dimensional model;
- Steady state operation;
- Isothermal operation, no heat flux into or out of the system;
- Gases assumed to behave as ideal gases and are well mixed in the respective gas chambers;
- Membrane is fully hydrated;
- Reactant gases are fully saturated with water vapor as they enter the gas diffuser layers;
- Gas pressures are constant and equal to the inlet pressures at the diffusion layers;

- Wet liquid pores in the gas diffuser;
- Electro-neutrality within the membrane.

3.3 Model equations

The following equations are used in the development of the model.

1. Nernst-Planck equation is used to determine species transport;
2. Modified form of Schlogl's velocity equation;
3. Butler-Volmer equation for electro-kinetics;
4. Stefan-Maxwell equation for gas transport;
5. Mass conservation equation;
6. Momentum (Darcy's) equation;
7. Current conservation equation;
8. Potential equation (Ohm's law).

In the following sections, the equations used to model the different regions of the fuel cell are developed.

3.3.1 Transport in Membrane Region

The main function of the membrane is to transfer protons from the anode catalyst region to the cathode catalyst region of the fuel cell, while restricting the passage of hydrogen, oxygen, and electrons between the anode and cathode. A generalized equation that describes the flux of species through the membrane is given by the Nernst-Planck equation (Bernardi and Verbrugge, 1991).

$$N_j = -z_j \frac{F}{R\_j * T} D_j C_j \frac{d\phi}{dZ} - D_j \frac{dC_j}{dZ} + C_j v \qquad (3.3.1.1)$$

Where species j is either a proton (hydrogen ion) or water (H_2O)

N_j = Molar flux of species j (mol/(cm^2-sec))

z_j = Charge on species j

F = Faraday's constant = 96484 (coulombs/equivalent)

T = Cell temperature (K)

R_j = Universal gas constant =8.314(Joule/(mol-K))

D_j = Diffusion coefficient of species j (cm^2/sec)

C_j = Concentration of species j (mol/cm^3)

ϕ = Membrane phase potential (volts)

v = Water velocity (cm/sec)

Z = Distance (cm)

This equation states that the movement of species j is due to three contributions: migration, diffusion, and convection. The first term on the right hand side of equation (3.3.1.1) describes the migration of species j due to the transfer of a charged species under the influence of an electric field. The second term on the right hand side of the equation (3.3.1.1) describes the diffusion of species j due to the presence of a concentration gradient $\frac{dC_j}{dZ}$. The third term on the right hand side of equation (3.3.1.1) describes the convection of species j caused by the pressure gradient $\frac{dP}{dZ}$ that drives the flow. The flow of charge is related to the current density by equation (3.3.1.2) (Bernardi and Verbrugge, 1991).

$$i = F\sum_{j} z_j N_j \tag{3.3.1.2}$$

Where

i = ionic current density (Amps/cm^2)

N_j = Molar flux of species j (mol/(cm^2-sec))

z_j = Charge on species j

F = Faraday's constant =96484 (coulombs/equivalent)

The equation for the membrane potential is obtained by combining equations (3.3.1.1) and (3.3.1.2). The differential equation for the membrane potential is shown in equation (3.3.1.3).

$$\frac{d\phi}{dZ} = \frac{-i}{\kappa} - \frac{F}{\kappa}\left(\sum_{j} z_j D_j \frac{dC_j}{dZ}\right) + \frac{F}{\kappa}\left(\sum_{j} z_j C_j\right)v \tag{3.3.1.3}$$

Where

κ = Membrane conductivity (mho/cm).

The equation for the membrane conductivity is shown in equation (3.3.1.4) (Bernardi and Verbrugge, 1991).

$$\kappa = \frac{F^2}{R\_j * T}\sum_{j} z_j^2 D_j C_j \tag{3.3.1.4}$$

The fluid motion is described using Schlogl's equation of motion, as shown in equation (3.3.1.5) (Bernardi and Verbrugge, 1991).

$$v = \left(\frac{k_\phi}{\mu} z_f c_f F \right) \frac{d\phi}{dZ} - \left(\frac{k_P}{\mu} \right) \frac{dP}{dZ} \tag{3.3.1.5}$$

k_ϕ = Electro kinetic permeability (cm^2)

k_P = Hydraulic permeability (cm^2)

z_f = Charge of membrane fixed-charge-site (+1)

c_f = Concentration of membrane fixed-charge-site (mol/cm^3)

μ = Pore water viscosity (gram/(cm-sec))

P = Hydraulic pressure (atm)

In this application, current and mass are conserved quantities. Thus, the conservation of current is given by equation (3.3.1.6), while the conservation of mass is given by equation (3.3.1.7) (Bernardi and Verbrugge, 1991).

$$\frac{di}{dZ} = 0 \tag{3.3.1.6}$$

$$\frac{dN_j}{dZ} = 0 \tag{3.3.1.7}$$

Assuming that the fluids behave as incompressible fluids, the continuity equation is given as equation (3.3.1.8) (Bernardi and Verbrugge, 1991).

$$\frac{dv}{dZ} = 0 \tag{3.3.1.8}$$

In the membrane of the PEM fuel cell, the only mobile ions are protons. The requirement of electroneutrality results in the reduction of the equation (3.3.1.3) to the following form, when equations (3.3.1.6), (3.3.1.7), and (3.3.1.8) are combined.

$$\kappa \frac{d\phi}{dZ} = -i + F * c_f * v$$

From equations (3.3.16) and (3.3.1.7)

$$\frac{d}{dZ}\left(\kappa \frac{d\phi}{dZ}\right) = 0 \qquad (3.3.1.9)$$

Where

$$\kappa = \frac{F^2}{R\_j * T} D_{H^+} C_{H^+} \qquad (3.3.1.10)$$

When equation (3.3.1.1) is substituted into equation (3.3.1.7) and used in equation (3.3.1.8), the dissolved species concentration is obtained (Bernardi and Verbrugge, 1991).

$$D_j \frac{d^2 C_j}{dZ^2} = v \frac{dC_j}{dZ} \qquad (3.3.1.11)$$

3.3.2 Transport in Active Catalyst Region

The kinetic expression for the electrochemical reaction is given by the Butler-Volmer equation. This equation is used to characterize the relationship between activation over-potential and current density at particular values of temperature, pressure and concentrations of the reacting species. The Butler-Volmer equation is given in equation (3.3.2.1) (Bernardi and Verbrugge, 1991).

$$\frac{di}{dZ} = ai_0 * \left(\exp\left(\alpha_a f\left(\phi_s - \phi\right)\right) - \exp\left(-\alpha_c f\left(\phi_s - \phi\right)\right)\right) \qquad (3.3.2.1)$$

Where

$$ai_0 = ai_0^{ref} * \left(\frac{C_{O_2}}{C_{O_2}^{ref}}\right)^{\gamma_{O_2}} \left(\frac{C_{H_{P2}}}{C_{H_P}^{ref}}\right)^{\gamma_{H_P}} \qquad (3.3.2.2)$$

i = Ionic current density (Amps/cm^2)

ai_0^{ref} = Reference exchange current density times area (Amps/cm^3)

α_a, α_c = Anode and cathode charge transfer coefficient

$$f = \frac{F}{R\_j * T}$$

ϕ_s = Solid phase potential (volts)

ϕ = Membrane phase potential (volts)

$C_{O_2}^{ref}, C_{H_P}^{ref}$ = Reference concentrations of oxygen and proton, respectively (mol/cm^3).

$\gamma_{O_2}, \gamma_{H_P}$ = Oxygen and proton concentration parameter for i_0

The exchange current density and charge transfer coefficients are determined by empirical expressions. The exchange current density is a function of reactant concentrations and is given as equation (3.3.2.2).

The difference between the solid phase potential (ϕ_s) and the membrane phase potential (ϕ) is known as the activation overpotential (η) and is shown in equation (3.3.2.3).

$$\eta = \phi_s - \phi \tag{3.3.2.3}$$

Since the reactant gases are consumed in this region, the mass balance equation simplifies to equation (3.3.2.4) (Bernardi and Verbrugge, 1991).

$$\frac{dN_j}{dZ} = -\left(\frac{s_j}{n\_c * F}\right)\frac{di}{dZ} \tag{3.3.2.4}$$

Liquid water is produced in the active catalyst region by the electrochemical reaction as shown in equation (3.1.2). By applying mass continuity, the velocity is obtained through equation (3.3.2.6) (Bernardi and Verbrugge, 1991).

$$\frac{dv_s}{dZ} = -\left(\frac{s_w}{n\_c * F * \rho}\right)\frac{di}{dZ} \tag{3.3.2.5}$$

But $v_s = \varepsilon_{m,c}\varepsilon_{w,m}v$, therefore

$$\frac{dv}{dZ} = -\left(\frac{s_w}{n\_c * F * \rho * \varepsilon_{m,c} * \varepsilon_{w.m}}\right)\frac{di}{dZ} \tag{3.3.2.6}$$

Where

v_s = Superficial water velocity (cm/sec)

$\varepsilon_{w.m}$ = Volume fraction of water in membrane region

$\varepsilon_{m,c}$ = Volume fraction of membrane in catalyst region

s_w = Stoichiometric coefficient of water

ρ = Molar density of water (mol/cm^3)

Assuming that the conductivity remains constant, Ohm's law gives the movement of electrons in the solid portion of the catalyst region as shown in equation (3.3.2.7) (Bernardi and Verbrugge, 1991).

$$i_{solid} = -\sigma_c^{eff}\frac{d\phi_s}{dZ} \tag{3.3.2.7}$$

Where

i_{solid} = Current density in the solid phase (Amps/cm^2)

σ_c^{eff} = Electronic conductivity of solid particles (C, Pt) (mho/cm)

ϕ_s = Solid phase potential (volts)

Z = Distance (cm)

By combining equations (3.3.1.1), (3.3.2.4), and (3.3.2.6), the concentration of each species in the active catalyst region is obtained, as shown in equation (3.3.2.8) (Bernardi and Verbrugge, 1991).

$$D_j^{eff}\frac{d^2C_j}{dZ^2}=(\varepsilon_{m,c}*v)\frac{dC_j}{dZ}-C_j\left(\frac{s_j}{n\_c*F}-\frac{s_w}{n\_c*F*\rho*\varepsilon_{w,m}}\right)\frac{di}{dZ} \qquad (3.3.2.8)$$

$\varepsilon_{m,c}$ = Volume fraction of membrane in the active catalyst region

s_j = Stoichiometric coefficient of species j

Use of the electroneutrality condition relates the current in the solid matrix to the current in the membrane matrix. This is represented as equation (3.3.2.9) (Bernardi and Verbrugge, 1991).

$$\frac{di_{solid}}{dZ}+\frac{di}{dZ}=0 \qquad (3.3.2.9)$$

This ultimately leads to equation (3.3.2.10) (Bernardi and Verbrugge, 1991).

$$i+i_{solid}=-I \qquad (3.3.2.10)$$

Where I is the operating current density and is taken as negative during operation.

3.3.3 Transport in Gas Diffuser Region

In the gas diffusion region, the main species present at the cathode side of PEM fuel cell are oxygen, nitrogen, and water. The Stefan-Maxwell equation describes the diffusion of a multicomponent mixture. Assuming that the gas mixture behaves ideally, this model can be used to describe the diffusion of species through the porous electrodes by equation (3.3.3.1) (Bernardi and Verbrugge, 1991).

$$\frac{dX_j}{dZ} = \sum_{m=1}^{n} \frac{R\_atm * T}{pD_{jm}^{eff}} \left(X_j N_{m,g} - X_m N_{j,g} \right) \tag{3.3.3.1}$$

X_j = Gas-phase mole fraction of species j

$N_{j,g}$ = Gas-phase flux of species j (mol/(cm^2-sec)

R_atm = Universal gas constant, (atm-cc/(mol-K))

pD_{jm}^{eff} = Effective gas-pair diffusivity of the pair j-m in porous medium (atm-cm^2/sec)

n = number of components.

The effective diffusivity is a function of temperature and pressure. At steady state, it is assumed that the fluxes of all diffusing species in the porous media are constant and thus independent of position. It is assumed that the water vapor in the diffusion region is in equilibrium with the water in the liquid phase, so that:

$$X_w = Y_w^{sat} \tag{3.3.3.2}$$

$$\frac{dX_w}{dZ} = 0 \tag{3.3.3.3}$$

In the gas pores of the cathode, oxygen has to diffuse through the water vapor and the nitrogen gas. The mass balance leads to equation (3.3.3.4) (Bernardi and Verbrugge, 1991).

$$X_{O_2} + X_{N_2} + X_w = 1 \tag{3.3.3.4}$$

The molar fluxes of nitrogen and oxygen are (Bernardi and Verbrugge, 1991).

$$\frac{dN_{O_2}}{dZ} = 0 \;\&\; \frac{dN_{N_2}}{dZ} = 0 \tag{3.3.3.5}$$

Since nitrogen is inert, there is no net flux of nitrogen. Therefore, the net flux of nitrogen is zero.

$$N_{N_2} = 0 \tag{3.3.3.6}$$

The gas phase flux of oxygen is related to the cell operating current density by equation (3.3.3.7) (Bernardi and Verbrugge, 1991).

$$N_{O_2} = \frac{I}{n\_c * F} \tag{3.3.3.7}$$

Combining equations (3.3.3.3), (3.3.3.5), and (3.3.3.7) with equation (3.3.3.1), the molar flux of water vapor at the cathode gas diffuser is obtained as equation (3.3.3.8) (Bernardi and Verbrugge, 1991).

$$N_w^{dc} = \frac{\left(I * X_w^{sat}\right)}{\left(n\_c * F\right)\left(1 - X_w^{sat} - X_{N_2}\left(1 - \frac{1}{r_w}\right)\right)} \tag{3.3.3.8}$$

Where

r_w = Diffusivity ratio of water

X_w^{sat} = Mole fraction of saturated water

N_w^{dc} = Superficial flux of water in gas phase (mol/(cm^2-sec))

n_c = Number of electron participating in the cathode reaction

F = Faraday's constant =96484 (coulombs/equivalent)

I = Operating current density (Amps/cm^2)

The Schlogl's velocity equation, retaining only the pressure gradient term, is used to characterize the water flow in the gas diffusion region, since the fluid is not charged. Also in the gas diffusion region, the solid phase current density (i_{solid}) is equal to the operating current density (I) (Bernardi and Verbrugge, 1991).

$$i_{solid} = -I \tag{3.3.3.9}$$

3.3.4 Fuel Cell Voltage

The fuel cell voltage is calculated by the equation (3.3.4.1)

$$V_{cell} = V_{OC} - \eta_{act} - IR_{m} \tag{3.3.4.1}$$

Where η_{act} is the activation over-potential at the membrane/catalyst interface, R_m is the resistance of the membrane to the transfer of protons from the anode side to the cathode side of the fuel cell, and V_{OC} is the reversible voltage or open circuit voltage of the fuel cell.

The thermodynamic open circuit potential of the fuel cell is calculated by equation (3.3.4.2) (Bernardi and Verbrugge, 1991).

$$V_{OC} = U^{0}_{thermo} + 2.3\left(\frac{R\_j * T}{n\_c * F}\right)\log\left(p^{2}_{H_2} * p_{O_2}\right) \tag{3.3.4.2}$$

$$U^{0}_{thermo} = 1.23 - 0.9e - 3 * (T - 298)$$

$$p_{H_2} = P_a$$

$$p_{O_2} = \left(1 - X^{sat}_{w} - X^{c}_{N_2}\right) * P_c$$

Where

V_{OC} = Open circuit potential (volts)

U^{0}_{thermo} = Reference potential (volts)

p_{O_2} = Partial pressure of oxygen (atm)

p_{H_2} = Partial pressure of hydrogen (atm)

T = Temperature (K)

3.4 Boundary Conditions

Boundary conditions are an essential element of the numerical solution. In this section, the various boundary conditions employed are discussed. These boundary conditions ensure continuity of the solution over the sampled variable space.

1. At the anode side of the membrane, the membrane phase potential is assumed to be zero, the pressure is assumed equal to the anode inlet pressure, and the concentration of oxygen is zero.

   At Z = 0,

   $$\phi = 0 \tag{3.4.1}$$

   $$P = P_a \tag{3.4.2}$$

   $$C_{O_2} = 0 \tag{3.4.3}$$

2 At the membrane/cathode catalyst interface, the current in the membrane phase is continuous, the superficial velocity of water is continuous, and the flux of dissolved oxygen is continuous.

   At Z = l_m,

$$\kappa\left(\frac{d\phi}{dZ}\right)\Bigg|_{m} = \kappa_{eff}\left(\frac{d\phi}{dZ}\right)\Bigg|_{c} \tag{3.4.4}$$

$$v\big|_{m} = \varepsilon_{m,c}\, v\big|_{c} \tag{3.4.5}$$

$$D_{O_2}\frac{dC_{O_2}}{dZ}\Bigg|_{m} = D_{O_2}^{eff}\frac{dC_{O_2}}{dZ}\Bigg|_{c} \tag{3.4.6}$$

3 At the cathode catalyst layer-cathode/gas diffuser region interface, the current in the solid phase is continuous.

$$\sigma_{eff}^{c}\frac{d\phi_{solid}}{dZ}\Bigg|_{c} = \sigma_{eff}^{d}\frac{d\phi_{solid}}{dZ}\Bigg|_{d} \tag{3.4.7}$$

The dissolved oxygen species concentration is given by the following equation

$$C_{O_2}^{sat} = \left(1 - X_{N_2} - X_{w}^{sat}\right)\frac{P_c}{K_{O_2}} \tag{3.4.8}$$

At the cathode gas diffuser, the pressure is equal to the inlet gas chamber pressure and the nitrogen mass fraction is obtained from:

$$X_{N_2}^{c} = \frac{\left(1 - X_{w}^{sat}\right)\left(\frac{\varsigma}{\varsigma - 1}\right)\left(\frac{X_{N_2}^{0}}{X_{O_2}^{0}}\right)}{\left(1 + \left(\left(\frac{\varsigma}{\varsigma - 1}\right)\left(\frac{X_{N_2}^{0}}{X_{O_2}^{0}}\right)\right)\right)} \tag{3.4.9}$$

Where

$X_{N_2}^{c}$ = Gas phase mole fraction of nitrogen at cathode inlet

ς = Stoichiometric flow ratio =3

$\frac{X_{N_2}^0}{X_{O_2}^0}$ = Inlet Nitrogen-Oxygen mole ratio ($\frac{0.79}{0.21}$)=3.719

X_w^{sat} = Saturated mole fraction of water

All initial calculations needed for the model are detailed in Appendix A. Derivations of all governing equations are given in Appendix B.

3.5 Numerical Methods

Combination of the developed equations and boundary conditions described in the previous sections of this chapter results in a set of six differential equations that must be solved simultaneously for the six unknown variables: $\phi, v, i, V_{omic}, C_{O_2}, \text{and } P$. This equation set is solved using finite difference methods. The final governing equations for each variable in the different regions of the PEM fuel cell are shown below. Derivations of these governing equations are shown in Appendix B.

3.5.1 Membrane Region

a) The membrane phase potential is given by equation (3.5.1.1):

$$\frac{d}{dZ}\left(\kappa \frac{d\phi}{dZ}\right) = 0 \qquad (3.5.1.1)$$

b) The velocity is given by equation (3.5.1.2):

$$v = \left(\frac{k_\phi}{\mu} z_f c_f F\right)\frac{d\phi}{dZ} - \left(\frac{k_P}{\mu}\right)\frac{dP}{dZ} \qquad (3.5.1.2)$$

c) The ionic current density is calculated by equation (3.5.1.3):

$$i = -\kappa \frac{d\phi}{dZ} + F * c_f * v \tag{3.5.1.3}$$

d) The ohmic overpotential is calculated by equation (3.5.1.4):

$$V_{ohmic} = i * \frac{\Delta Z}{\kappa} \tag{3.5.1.4}$$

e) The concentration of dissolved oxygen is given by equation (3.5.1.5):

$$D_j \frac{d^2 C_j}{dZ^2} = v \frac{dC_j}{dZ} \tag{3.5.1.5}$$

f) The hydraulic pressure is given by equation (3.5.1.6):

$$\frac{d^2 P}{dZ^2} = 0 \tag{3.5.1.6}$$

3.5.2 Active Catalyst Region

a) The membrane phase potential is given by equation (3.5.2.1):

$$\kappa_{eff} \frac{d^2\phi}{dZ^2} = ai_0 \left(1 + \frac{(s_w * c_f)}{(n\_c * \rho * \varepsilon_{w,m})} \right) * \exp(-\alpha_c f(\phi_s - \phi_0 - V_{OC})) * (1 + (\alpha_c f) * (\phi - \phi_0))$$

$$\text{Let coef} = ai_0 \left(1 + \frac{(s_w * c_f)}{(n\_c * \rho * \varepsilon_{w,m})} \right) * \exp(-\alpha_c f(\phi_s - \phi_0 - V_{OC}))$$

$$\kappa_{eff} \frac{d^2\phi}{dZ^2} = \text{coef} * (1 + (\alpha_c f) * (\phi - \phi_0)) \tag{3.5.2.1}$$

b) The velocity is given by equation (3.5.2.2):

$$v = \left(\frac{k_\phi^{eff}}{\mu} z_f c_f F \right) \frac{d\phi}{dZ} - \left(\frac{k_P^{eff}}{\mu} \right) \frac{dP}{dZ} \tag{3.5.2.2}$$

c) The ionic current density is calculated by equation (3.5.2.3):

$$i = -\kappa_{eff}\frac{d\phi}{dZ} + F * c_f * \varepsilon_{m,c} * v \tag{3.5.2.3}$$

d) The ohmic overpotential is calculated by equation (3.5.2.4):

$$V_{ohmic} = i * \frac{\Delta Z}{\kappa_{eff}} \tag{3.5.2.4}$$

e) The concentration of dissolved oxygen is given by equation (3.5.2.5):

$$D_j^{eff}\frac{d^2C_j}{dZ^2} = (\varepsilon_{m,c} * v)\frac{dC_j}{dZ} - C_j\left(\frac{s_j}{n\_c * F} - \frac{s_w}{n\_c * F * \rho * \varepsilon_{w,m}}\right)\frac{di}{dZ} \tag{3.5.2.5}$$

f) The hydraulic pressure is given by equation (3.5.2.6):

$$\left(\frac{k_P^{eff}}{\mu}\right)\frac{d^2P}{dZ^2} = \left(\frac{k_\phi^{eff}}{\mu}z_f c_f F\right)\frac{d^2\phi}{dZ^2} + \left(\frac{s_w}{n\_c * F * \rho * \varepsilon_{w,m}}\right)\frac{di}{dZ} \tag{3.5.2.6}$$

3.5.3 Gas Diffuser Region

a) The water velocity is given by equation (3.5.3.1):

$$v_s = -\left(\frac{k_{p_s}^d}{\mu}\right)\frac{dP}{dZ} \tag{3.5.3.1}$$

b) The hydraulic pressure is given by the equation (3.5.3.2):

$$\left(\frac{k_{p_s}^d}{\mu}\right)\frac{d^2P}{dZ^2} = \frac{1}{\rho}\frac{dN_{w,g}}{dZ} \tag{3.5.3.2}$$

3.5.4 Finite Difference Method

These equations were implemented in MATLAB$^{@}$. The finite difference method was used. In this method, each derivative and coefficient were approximated in each partial differential equation. In order to use the finite difference method, one must define the grid spacing properly because the errors associated with solving partial differential equations via this method are a strong function of grid spacing. An example of a grid is shown in Figure 3.2 (Mathews, 1999).

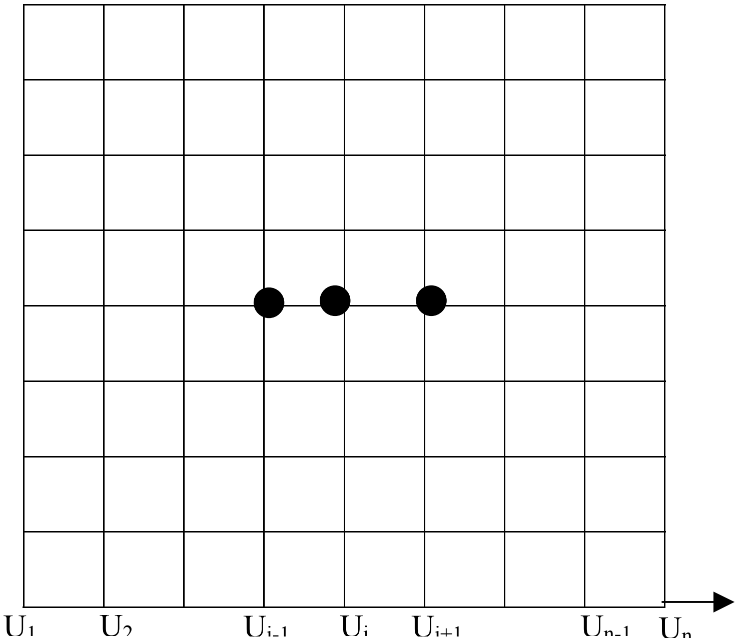

Figure 3.2. Example of Grid.

After grid spacing was established as shown in Figure 3.2, derivatives were approximated using the system of lines of intersections (nodes). The value of the dependent variable "u" in the derivative was obtained using a Taylor's series expansion in terms of variable values at adjacent nodes. For example, the value of "u" at the node [n, j+1] using a Taylor series expansion is:

$$u_{j+1}^{n} = u_{j}^{n} + \left(\frac{\partial u}{\partial x}\right)_{j}^{n} \Delta x + \frac{1}{2!}\left(\frac{\partial^{2} u}{\partial x^{2}}\right)_{j}^{n} \Delta x^{2} + \dots\dots\dots + \frac{1}{k!}\left(\frac{\partial^{k} u}{\partial x^{k}}\right)_{j}^{n} \Delta x^{k} \qquad (3.5.4.1)$$

Truncating the Taylor series at the second derivative simplifies equation (3.5.4.1) to:

$$u_{j+1}^{n} = u_{j}^{n} + \left(\frac{\partial u}{\partial x}\right)_{j}^{n} \Delta x + \frac{1}{2!}\left(\frac{\partial^{2} u}{\partial x^{2}}\right)_{j}^{n} \Delta x^{2} \qquad (3.5.4.2)$$

Rearrangement of equation (3.5.4.2) for the first derivative yields:

$$\left(\frac{\partial u}{\partial x}\right)_{j}^{n} \Delta x = u_{j+1}^{n} - u_{j}^{n} - \frac{1}{2!}\left(\frac{\partial^{2} u}{\partial x^{2}}\right)_{j}^{n} \Delta x^{2} \qquad (3.5.4.3)$$

Finally, dividing by Δx results in:

$$\left(\frac{\partial u}{\partial x}\right)_{j}^{n} = \frac{u_{j+1}^{n} - u_{j}^{n}}{\Delta x} - \frac{1}{2!}\left(\frac{\partial^{2} u}{\partial x^{2}}\right)_{j}^{n} \Delta x \qquad (3.5.4.4)$$

Equation (3.5.4.4) is known as the forward finite difference formula. The first term on the right hand side of equation (3.5.4.4) (Mathews, 1999, Daniil, 2002) is the forward finite difference approximation and the second term is the local truncation error. Similarly, the backward finite difference formula is obtained by performing a Taylor series expansion at node [n, j-1].

$$u_{j-1}^{n} = u_{j}^{n} - \left(\frac{\partial u}{\partial x}\right)_{j}^{n} \Delta x + \frac{1}{2!}\left(\frac{\partial^{2} u}{\partial x^{2}}\right)_{j}^{n} \Delta x^{2} - \dots\dots\dots + \frac{(-1)^{k}}{k!}\left(\frac{\partial^{k} u}{\partial x^{k}}\right)_{j}^{n} \Delta x^{k} \qquad (3.5.4.5)$$

Rearrangement to obtain the first derivative yields:

$$\left(\frac{\partial u}{\partial x}\right)_j^n = \frac{u_j^n - u_{j-1}^n}{\Delta x} + \frac{1}{2!}\left(\frac{\partial^2 u}{\partial x^2}\right)_j^n \Delta x \qquad (3.5.4.6)$$

The first term on right hand side of equation (3.5.4.6) is known as the backward finite difference approximation. The last finite difference formula is the centered finite difference formula. The formula for the centered finite difference is obtained by taking the average of the forward and backward finite difference formulae. By taking the average of equations (3.5.4.4) and (3.5.4.6), the first derivative for the centered finite difference method is obtained as equation (3.5.4.7):

$$\left(\frac{\partial u}{\partial x}\right)_j^n = \frac{u_{j+1}^n - u_{j-1}^n}{2\Delta x} + \frac{1}{6}\left(\frac{\partial^3 u}{\partial x^3}\right)_j^n \Delta x^2 \qquad (3.5.4.7)$$

From equations (3.5.4.4), (3.5.4.6) and (3.5.4.7), one observes that the truncation error for the centered finite difference method is of order Δx^2. In contrast, the truncation error for either the forward or the backward finite difference formula is of order Δx. For this reason, the centered finite difference formula is implemented to solve the ordinary differential equation set.

In a similar fashion, higher order derivatives can be approximately solved using finite difference expressions. For example, the centered finite difference formula to approximate a second derivative is given by equation (3.5.4.8)

$$\left(\frac{\partial^2 u}{\partial x^2}\right) = \frac{u_{j+1}^n - 2u_j^n + u_{j-1}^n}{\Delta x^2} - \frac{1}{12}\left(\frac{\partial^4 u}{\partial x^4}\right)_j^n \Delta x^2 \qquad (3.5.4.8)$$

For this approximation, the truncation error is also of order Δx^2.

Once the derivative is approximated, the ordinary differential equation is transformed into a system of linear equations in the form of AX=B where X is the solution of the dependent variable (Daniil, 2003). This is illustrated in the following example.

For the membrane phase potential in the membrane region, equation (3.5.1.1) is solved as follows.

$$\frac{d}{dZ}\left(\kappa \frac{d\phi}{dZ}\right) = 0$$

Using the centered finite difference formula for the second derivative, equation (3.5.1.1) becomes;

$$\frac{\phi_{j-1} - 2\phi_j + \phi_{j-1}}{\Delta Z^2} = 0$$

$$\downarrow$$

$$\phi_{j-1} - 2\phi_j + \phi_{j-1} = 0$$

$$\downarrow$$

$$\begin{bmatrix} 1 & 0 & 0 & & & & & 0 \\ -2 & 1 & & & & & & \\ 1 & -2 & 1 & & 0 & & & \\ & 1 & -2 & 1 & & & & \\ & & & & & & & \\ & & & & & & & \\ 0 & & & & & & & \\ & & & & & 1 & -2 & 1 \\ & & & & & & 1 & -2 \\ & & & & & & -1 & 1 \end{bmatrix} \begin{bmatrix} \phi_1 \\ \phi_2 \\ . \\ . \\ \phi_j \\ . \\ . \\ \phi_{N-2} \\ \phi_{N-1} \\ \phi_N \end{bmatrix} = \begin{bmatrix} 0 \\ 0 \\ . \\ . \\ \\ \\ \\ \\ \\ \left(Fc_f v(N) \Delta Z / \kappa \right) \end{bmatrix} \qquad (3.5.4.9)$$

Where $j = 1, 2, ...N-1$ and the first and last terms on right hand side are the boundary conditions for the membrane phase potential. The linear system, shown in equation (3.5.4.9), is then solved in MATLAB using the Gauss-Seidel iterative method along with the boundary conditions.

CHAPTER IV

EXPERIMENTAL

The main components of the PEM fuel cell are the bi-polar plates and the membrane-electrode-assembly (MEA). Bi-polar plates are made from a conductive material such as stainless steel or graphite. The main functions of the bi-polar plates are to provide an inlet and outlet for the flowing gases and to act as the current collectors (Larminie and Dicks, 2003). One of the main components of the MEA is the gas diffusion layer (GDL). The GDL not only serves as a support for the membrane-electrode-assembly, but also distributes the reactant gases over the catalyst layer and transports electrons to and from the reaction sites (EG&G Technical Services, Inc., 2002). The gas diffusion layer also plays a major role in water and energy management in the PEM fuel cell. GDL's are mainly made from carbon-based materials (Larminie and Dicks, 2003). Hydrophobic materials such as polytetrafluoroethylene (Teflon) are incorporated into the diffusion layer to prevent water from flooding the pores of the layer. This allows the gases to reach the catalyst sites (EG&G Technical Services, Inc., 2002).

In this work, carbon materials used for the gas diffusion layer have been characterized by surface area analysis (BET), scanning electron microscopy (SEM), mercury/non-mercury porosimetry and capillary flow porometry. Four different materials were examined: 1) untreated carbon paper; 2) Teflon-treated carbon paper; 3) untreated carbon cloth; and 4) Teflon-treated carbon cloth. These materials were purchased from Electrochem, Inc. (Woburn, MA). The carbon paper was Electrode Porous Toray Carbon Paper (19 cm x 19 cm x 0.17 mm), untreated and treated with Teflon. The manufacturer supplied density of the carbon paper is 0.49 g/cc. The carbon cloth was also supplied in untreated and Teflon treated forms (19 cm x 19 cm x 0.33 mm) with a manufacturer-reported density of 1.75 g/cc. Porosimetry and porometry measurements were performed at Porous Materials, Inc. (Ithaca, NY). In the following sections, detailed descriptions of these techniques are given.

4. 1 Adsorption

Gas adsorption is used to measure the specific surface area and the pore size distribution of a solid material. Adsorption is a technique where atoms or molecules of the gas (adsorbate) are attached to the surface of the solid (adsorbent) (Brunauer, 1945). Adsorption processes can be divided into two categories: physical adsorption (physisorption); and chemical adsorption (chemisorption).

Physisorption is a reversible, exothermic process with a low heat of adsorption (Gregg and Sing, 1967). In physisorption, the weak van der Waals attractive forces are formed between the adsorbent and the adsorbate, whereas in chemisorption, covalent bonds are formed between the adsorbent and the adsorbate (Young and Crowell, 1962). In physisorption, there are no chemical interactions between the adsorbent and the adsorbate, and thus, the surface of the solid does not undergo any chemical change. The characteristics of solid materials are determined from the adsorption and the desorption isotherms. A plot of relative pressure as a function of the volume of gas adsorbed is known as the adsorption isotherm. The relative pressure is the ratio of the gas pressure to the saturation vapor pressure of the adsorbate at a fixed, constant temperature (liquid nitrogen temperature at atmospheric pressure). “The isotherm shape reveals not only the structure of adsorbent, but also the adsorption and desorption process” (Doan, 2001). A complete description of the isotherms and the hysteresis are detailed in Doan (2001).

4.1.1 Brunauer-Emmett-Teller (BET) Model

In 1915, Langmuir developed an analysis method, assuming that gases form only a monolayer on the surface of the adsorbent and that each site adsorbs only one molecule (Langmuir, 1918). Langmuir assumed that the gas molecules collide with the adsorbent sites and remain attached to the adsorbent surface for a particular amount of time due to inelastic collisions. Therefore, the Langmuir isotherm depends on the rate at which molecules collide with, and leave from, the surface of the adsorbent sites (Webb and Orr, 1998). However, the Langmuir model is not applicable to microporous physisorption (Langmuir, 1915). Based on the Langmuir method, Brunauer, Emmett and Teller (BET) developed the BET model, which includes multilayer adsorption phenomenon (Brunauer et al., 1938). The BET theory is based on the assumption that the adsorption sites on the surface of the solid all possess the same energy. The BET method is widely used to analyze the adsorption data using equation (4.1.1.1) (Quantachrome Corporation, 1998).

$$\frac{1}{W\left(\left(\frac{P}{P_0}\right)-1\right)}=\frac{1}{W_mC}+\left(\frac{C-1}{W_mC}\right)\left(\frac{P}{P_0}\right) \tag{4.1.1.1}$$

Where W = Weight of gas adsorbed at relative pressure $\left(\frac{P}{P_0}\right)$

W_m = Weight of the adsorbate forming monolayer on the surface

P_0 = Saturation pressure of the adsorbate at the adsorption temperature.

C = energy of the adsorption in the monolayer.

A BET plot is a plot of $\frac{1}{W\left(\left(\frac{P}{P_0}\right)-1\right)}$ vs. $\left(\frac{P}{P_0}\right)$. The values of W_m and C are obtained from the slope and intercept of the BET plot, respectively. The surface area is then calculated by equation (4.1.1.2) (Quantachrome Corporation, 1998).

$$S_t=\frac{W_mNA_{cs}}{M} \tag{4.1.1.2}$$

Where S_t = Surface area of the adsorbent

N = Avogadro's number

A_{cs} = Cross-sectional area of the adsorbate

M = Molecular weight of the adsorbate

The specific surface area is then obtained by dividing the surface area by the weight of the sample. The C constant in the BET equation is a qualitative measure of the interactions of the adsorbate and the adsorbent in the monolayer. The C value also gives the fraction of adsorbent surface covered (Doan, 2001). C is evaluated using equation (4.1.1.3) (Brunauer et al., 1940).

$$C = e^{\frac{(E_A - E_L)}{RT}} \tag{4.1.1.3}$$

Where E_A is the heat of the adsorption of the gas in the first adsorbed layer, E_L is the heat of liquefaction of the gas and R is the gas constant. If $E_A > E_L$, then the attractive forces between the adsorbate and the adsorbent are greater than the attractive forces between gas molecules in the liquefied state. For most solids, the linear BET region is in the relative pressure range of 0.05-0.35, when nitrogen is the adsorbate. The linear BET region is limited and depends on the system and the operating temperature (Rouquerol et al., 1999). The operating temperature and cross-sectional area of different adsorbate gases are given in Table 4.1 (Doan, 2001).

Table 4.1. Adsorbate Parameters (Doan, 2001).

Adsorbate Gas	Temperature (K)	BET Range	Close-packed Cross Sectional Area $(\text{Å})^2$/molecule	Customary Cross-sectional Area $(\text{Å})^2$/molecule
Nitrogen	77	0.13-20	16.2	16.2
Argon	77	0.10-0.19	13.8	13.8
Krypton	77	0.14-0.24	15.2	20.2
Xenon	77	0.16-0.25	16.8	17.0
Oxygen	77	0.13-0.20	14.1	14.1
Carbon dioxide	195	0.14-0.22	16.3	21.0
n-Butane	273	0.32-0.53	32.1	43.0
Benzene	293	0.25-0.51	30.7	43.0

The BET theory has been criticized for assuming the same energy for all adsorption sites, since many adsorbent surfaces are heterogeneous in energy (Gregg and Sing, 1967). The BET model also does not consider the interactions between neighboring molecules in the same layer. Due to the horizontal forces between adsorbate molecules at higher degrees of coverage, the separation between molecules is less than a single diameter. The BET model also neglects the reduction in adsorption forces as the distance from the surface increases (Gregg and Sing, 1967).

4.1.2 Barrett-Joyner-Halenda (BJH) Model

Barrett, Joyner and Halenda developed the BJH method to estimate the volume and area of porous materials. They assumed that the pores are open-ended and cylindrical in shape and that the relative pressure varies only a very small amount from unity so that all pores are filled with liquid (Barrett et al., 1951). They assumed t_1 as the thickness of the adsorbate molecules adsorbed over the pore radius, r_{p1}. They also assumed equilibrium conditions. The relationship between pore volume and the inner capillary volume is given by equation (4.1.2.1) (Barrett et al., 1951).

$$V_{P1} = V_{k1}\left(\frac{r_{P1}^2}{r_{k1}^2}\right) \tag{4.1.2.1}$$

Where V_{P1} = Pore volume

V_{k1} = Inner capillary volume

r_{P1} = Largest pore radius

r_{k1} = Inner capillary radius

A schematic of the desorption mechanism showing different pores is shown in Figure 4.1 (Doan, 2001). Since V_{k1} is not measurable, the relative pressure is lowered from $(P/P_0)_1$ to $(P/P_0)_2$ and the desorbed volume (ΔV_1) of the adsorbed gas from the first pore is measured. Due to this desorption, the largest pore is emptied of the capillary condensate. This also results in a reduction in the thickness of the adsorbed layer by an amount, Δt_1. The desorbed volume of the first largest pore is given by equation (4.1.2.2) (Barrett et al., 1951).

$$V_{P1} = V_{k1}\left(\frac{r_{P1}^2}{(r_{k1} + \Delta t_1)^2}\right) \tag{4.1.2.2}$$

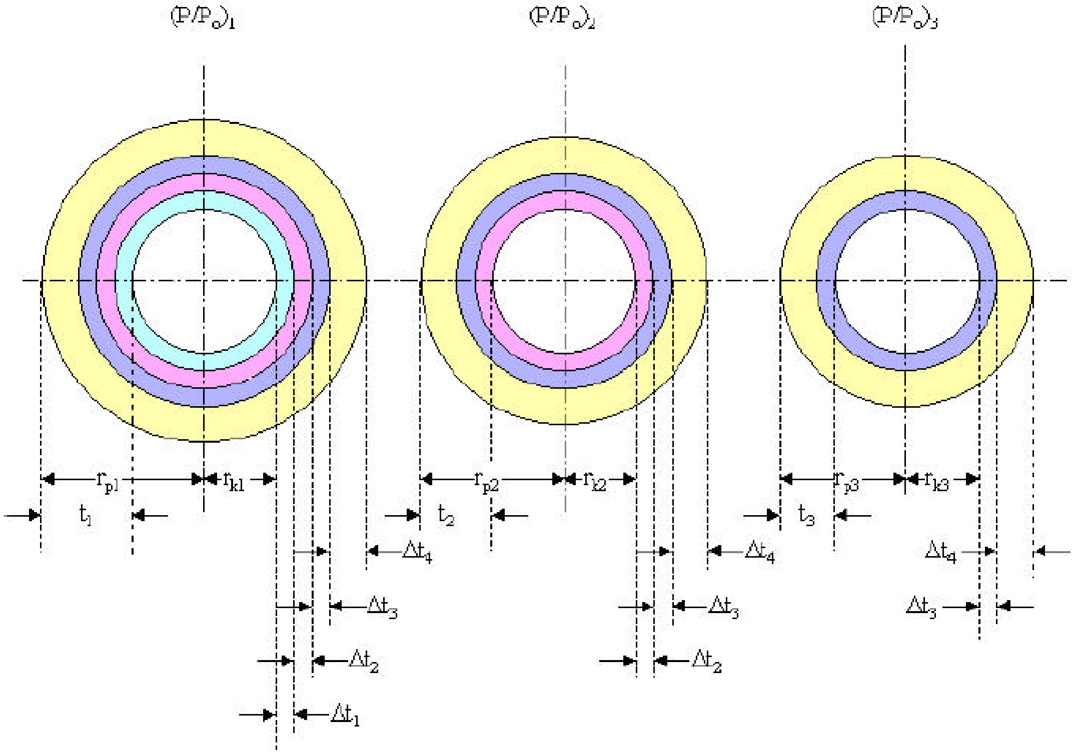

Figure 4.1. Desorption Steps for Three Different Pores (Doan, 2001).

Similarly, when the relative pressure is further lowered from $(P/P_0)_2$ to $(P/P_0)_3$, the desorption volume includes both the volume from the second pore and from the second thinning layer ($V_{\Delta t2}$). The desorption volume from the second pore is given by equation (4.1.2.3) (Barrett et al., 1951).

$$V_{P2} = (\Delta V_2 - V_{\Delta t2})\left(\frac{r_{P2}^2}{(r_{k2} + \Delta t_2)^2}\right) \tag{4.1.2.3}$$

With this stepwise desorption process, more pores become involved and computing becomes complicated. Therefore, the volume of the second thinning layer, as shown in equation (4.1.2.4), is given in terms of the average area (Ac_1) from which adsorbed gas is desorbed (Barrett et al., 1951).

$$V_{\Delta t2} = \Delta t_2 Ac_1 \tag{4.1.2.4}$$

The generalized form of the stepwise desorption of the thinning layer is shown in equation (4.1.2.5) (Barrett et al., 1951).

$$V_{\Delta tn} = \Delta t_2 \sum_{j=1}^{n-1} Ac_j \tag{4.1.2.5}$$

The generalized form for the desorbed volume is expressed as equation (4.1.2.6) (Doan, 2001).

$$V_{Pn} = \left(\Delta V_n - \Delta t_n \sum_{j=1}^{n-1} Ac_j \right) \left(\frac{r_{Pn}^2}{\left(r_{kn} + \Delta t_n\right)^2} \right) \tag{4.1.2.6}$$

Since Ac_j is not constant, but varies for each stepwise desorption step, an alternate way to describe the desorption volume is based on the pore area. The relationship between pore area and Ac_j is given in equation (4.1.2.7) (Barrett et al., 1951).

$$Ac_j = C_j A_P \tag{4.1.2.7}$$

Where $C_j = \frac{\left(r_P - t_r\right)}{r_P}$

$A_P = \frac{2V_P}{r_P}$, Area of each pore

r_P = Radius of the previously emptied pore.

t_r = Thickness of the adsorbed layer at corresponding relative pressure

Substituting equation (4.1.2.7) into equation (4.1.2.6), the final form for the desorbed volume becomes:

$$V_{Pn} = \left(\Delta V_n - \Delta t_n \sum_{j=1}^{n-1} C_j A_P \right) \left(\frac{r_{Pn}^2}{\left(r_{kn} + \Delta t_n\right)^2} \right) \qquad (4.1.2.8)$$

The BJH model is applicable in the range of unity relative pressure to 0.3.

4.1.3 The t Method

The t method is used to find the surface area and micropore volume in the presence of mesopores. Pores are classified based on their widths as micropores (diameter less than 20 Å), mesopores (diameter between 20 Å and 500 Å) and macropores (diameter greater than 500 Å). The t-method is based on BET theory, which involves adsorption of adsorbate (gas) on the adsorbent (sample) at low pressures. The t-method is valid up to relative pressures of 0.75 (De Boer et al., 1965). There are three characteristic t curves, as shown in Figure 4.2 (Doan, 2001).

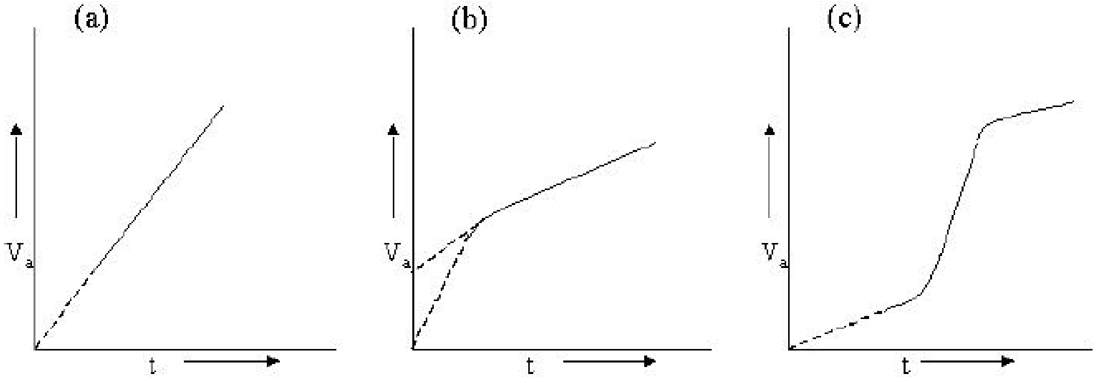

Figure 4.2. Characteristic t Curves.

A t curve is a plot of volume of adsorbed gas versus the thickness of the adsorbed layer. Figure 4.2a is a t plot of a sample having no micropores. In this sample, capillary condensation at the adsorption temperature is also absent (Quantachrome Corporation, 1998). Figure 4.2b and Figure 4.2c give details regarding the micropore structure of the sample. The slope of the t curve gives the surface area, which need not be same as the BET surface area. This is because, instead of the various C values in the BET equation, an average valve is used to produce the t curve (Lippens and De Boer, 1965). The micropore volume is calculated from the intercept of the t curve after conversion to liquid volume (Quantachrome Corporation, 1998). The average thickness of the adsorbed layer based on the BET model is expressed as equation (4.1.3.1) (Lippens et al., 1964).

$$t = \left(\frac{X}{S}\right)10^4 = \left(\frac{MV_{sp}}{22414}\right)\left(\frac{V_a}{S}\right)10^4 \tag{4.1.3.1}$$

Where t = Thickness of the adsorbed layer

X = Adsorbed volume of liquid adsorbate (ml)

S = Specific surface area (m^2/gram)

M = Molecular weight of the adsorbate

V_a = Adsorbed volume of the adsorbate at STP (ml/gram)

V_{sp} = Specific volume of the adsorbate (ml/gram)

For nitrogen as the adsorbate gas, equation (4.1.3.1) reduces to equation (4.1.3.2) (Lippens et al., 1964).

$$t = 15.47\left(\frac{V_a}{S}\right) \tag{4.1.3.2}$$

The t method assumes that the properties of the adsorbed layer are the same as the properties of liquid nitrogen and that the adsorbed layer has the same density as the capillary condensed liquid (Lippens et al., 1964). The t valves are calculated using either the Hasley equation, the De Boer equation, or the Carbon-Black equation as a function of relative pressure. The De Boer method is applied to gas adsorption on solids using equation (4.1.3.3) (Quantachrome Corporation, 1998).

$$t = \left(\frac{13.99}{\left(0.034 + \log\left(\frac{P_0}{P} \right) \right)} \right)^{\frac{1}{2}} \tag{4.1.3.3}$$

The De Boer equation can be applied for the multilayer region, but does not apply for condensed phase (Jura and Harkins, 1946). The Halsey equation for nitrogen adsorption at 77 K is expressed as equation (4.1.3.4) (Quantachrome Corporation, 1998). The Halsey method is based on the assumption that the adsorption energy in the second layer is equal to the liquefaction energy (Halsey, 1948).

$$t = 3.54 \left(\frac{5.0}{2.303 \log\left(\frac{P_0}{P} \right)} \right)^{\frac{1}{3}} \tag{4.1.3.4}$$

The Carbon-Black equation is shown in equation (4.1.3.5) (Quantachrome Corporation, 1998).

$$t_{CB} = 0.88 \left(\frac{P_0}{P} \right)^2 + 6.45 \left(\frac{P_0}{P} \right) + 2.98 \tag{4.1.3.5}$$

The total surface area of all pores is then calculated using equation (4.1.3.6) (Quantachrome Corporation, 1998).

$$S_t = \frac{15.47 V_{ads}^{STP}}{t} \tag{4.1.3.6}$$

Where V_{ads}^{STP} is the volume of the adsorbed gas corrected to the standard conditions of temperature and pressure, and the constant, 15.47, represents a conversion factor to change gas volume to liquid volume (Quantachrome Corporation, 1998). The t method does not take into account the effect of pore filling by assuming monolayer adsorption occurs at the pore walls or open surface (De Boer et al., 1966).

4.1.4 Instrumentation

A Quantachrome Autosorb 1C instrument (Model P/N 05061-C) was used to perform the analysis of the carbon materials (carbon cloth and carbon paper). A schematic of the instrument is shown in the Figure 4.3 (Quantachrome System Manual, 1998). The instrument contains two out-gassing stations, the Dewar station, temperature and pressure measurement devices, cold trap, and the analysis station. A detailed diagram of the instrument is shown in Figure 4.4. The inert gas (helium) enters the instrument through the coarse valve at ambient temperature. The pressure transducer monitors the pressure of the entering gas. Fine and coarse valves control the flow rates of the adsorbate gas (nitrogen) entering the system. The main chamber of the system is known as the manifold. The thermometer and two transducers [100 torr and 10 torr] monitor the manifold temperature and pressure. The LED on the top front panel of the instrument, shown as temperature/pressure meter, indicates the manifold temperature (°C), manifold pressure (mm Hg), the sample station pressure (mm Hg), saturation pressure of the adsorbent (mm Hg), and the outgassing temperature (°C). Automatically controlled solenoid valves are used to separate the manifold from the other stations. Since the measurements are taken based on the manifold volume, the manifold is calibrated by using a solid sphere in the calibration chamber. Details about the calculations of the manifold volume are given elsewhere (Doan, 2001). The analysis station contains two stations. One station is used to measure the saturation pressure (P_0) of the adsorbate, while the other station is used for the sample analysis. A 1000 torr transducer measures the pressure in the saturation pressure station (P_0 cell) while the pressure in the sample station is measured by 1000 and 1 torr transducers. The cold trap dewar, which is mounted on the front of the panel, is filled with liquid nitrogen. The cold trap keeps the vacuum system clean and also prevents the sample degassing products and oil vapors from the vacuum pump from diffusing into the manifold.

Before starting the analysis, the sample was degassed in the outgassing station. Two outgassing stations were provided on the front panel of the system. Each outgas station has an individually controlled heating mantle. The maximum temperature allowed on the heating mantles is 350°C. The system is provided with a turbo pump and a mechanical pump to create the inert atmosphere inside the system. The outgassing stations are evacuated through either, or through both, a fine and coarse valve. A pirani gauge is used to monitor the pressure.

During analysis, the motor lifts the dewar flask in the dewar lift until both the sample cell and the saturation pressure cell (P_0 cell) are immersed in liquid nitrogen. The level of liquid nitrogen in the dewar is monitored by the thermistor. The LED's on the front panel indicate the status of the dewar. The blue "ON" light indicates the contact of the thermistor with liquid nitrogen. The flashing yellow "ON" light indicates that the dewar is moving up or down. The green "ON" light indicates normal operating status. The thermistor hangs parallel to the sample cell such that the bulb of the sample cell is immersed in the liquid nitrogen.

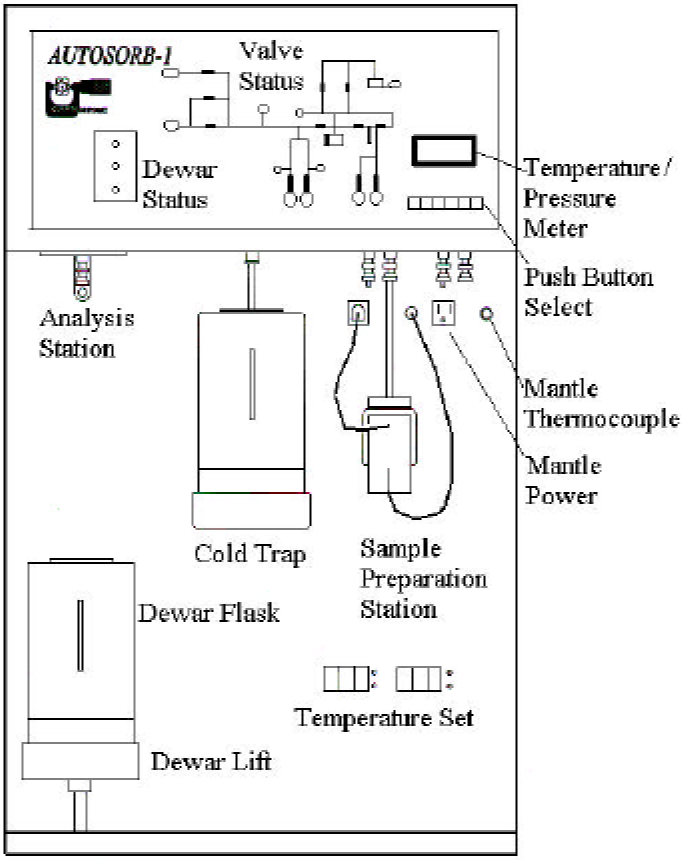

Figure 4.3. Schematic of the Instrument (Quantachrome System Manual, 1998).

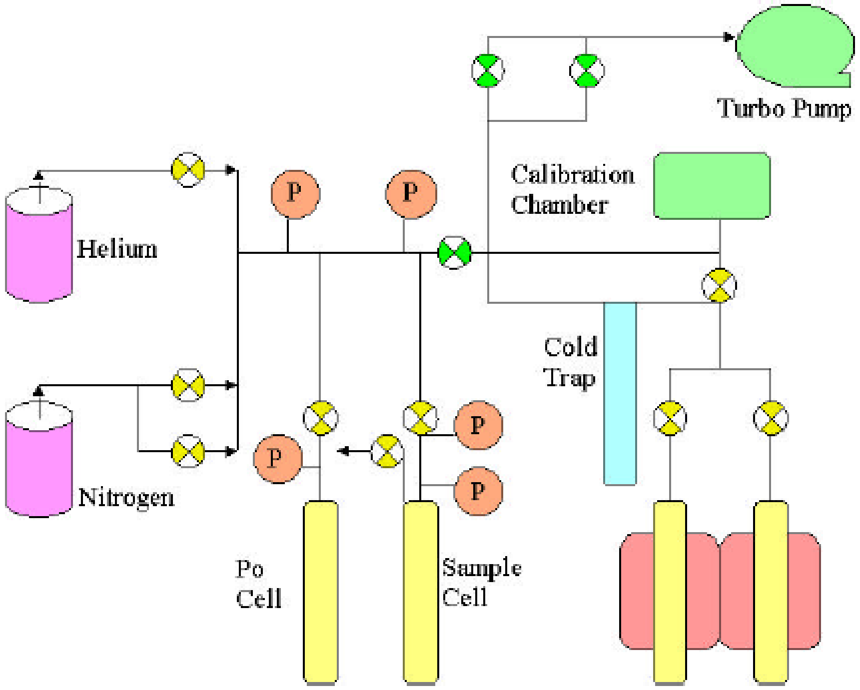

Figure 4.4. Detailed Diagram of the Instrument (Doan, 2001).

4.1.5 Operating Parameters

Nitrogen gas was used as the adsorbate gas and helium was used as the inert gas to create the inert atmosphere in the system. The manifold volume was calibrated using the standard sphere supplied by the Quantachrome Corporation. Liquid nitrogen was used in the cold trap. Table 4.2 shows the weight of the sample and operating conditions used during degassing of the different samples.

Table 4.2. Operating Parameters for Sample Degassing.

Parameter	Untreated Carbon Cloth	Teflon Treated Carbon Cloth	Untreated Carbon Paper	Teflon Treated Carbon Paper
Sample Weight, grams	0.5428	0.8730	0.6774	0.7995
Outgassing temperature, °C	150	150	110	110
Duration of outgassing, hours	18.374	13.389	10.588	9.190

A weighed sample was taken into the sample tube and degassed in the outgassing station until the sample passed the outgassing test of 5 μ mmHg/min. After the sample passed the outgassing test, the sample was allowed to return to ambient temperature. The sample cell was then placed in the sample analysis port. The system performed a leak test prior to the analysis. The physisorption analysis was carried out using nitrogen gas with fine evacuation and maxi dose on. The P_0 cell was placed in the saturation pressure station (P_0 station) to directly measure the saturation pressure of the nitrogen gas. Analysis was carried out for a previously selected micropore range, and 20 adsorption and 20 desorption points were measured with zero tolerance for relative pressure and an equilibration time of five minutes.

4. 2 Scanning Electron Microscope and X-Ray Microanalysis

Elemental characterization of contaminants and defects on the surfaces of the sample was performed using Scanning Electron Microscope (SEM) and Energy Dispersive X-Ray Spectrometry (EDS). SEM and EDS yield information about the topography, morphology, composition and crystallographic information of the sample. Electron microscopes use a beam of highly energetic electrons to examine the surface on a very finite scale (Michael et al., 1980). The electrons ejected from the surface of the sample produce the image once the electron beam strikes the sample. The beam interactions with the sample are classified into two types: elastic collisions and inelastic collisions. The elastic collisions produce backscattered electrons with negligible energy loss. The inelastic collision produces secondary electrons with a considerable amount of energy loss during collisions. Secondary electrons are absorbed by the adjacent atoms in the specimen due to their low energies (Michael et al., 1980). Therefore, only those secondary electrons created at the surface are able to escape from the surface of the specimen. In contrast, backscattered electrons can escape from greater depths within the specimen because of their high energy. The backscattered electrons have energies similar to those in the incident beam and interact with the specimen to produce more secondary electrons. The resulting backscattered electrons and collected secondary electrons produce the electron image (Michael et al., 1980). The difference in energies of initial and final states of the transitional electrons may be emitted as X-radiation (Michael et al.,1980). Since various shells of the atoms are associated with different energy levels, their energy differences, emitted as X-radiation, are unique and are characteristic of the shell in the atom from which it is released. Identification of the specific wavelength or energy of the X-radiation is very useful for the elemental analysis of the specimen.

4.2.1 Instrumentation

Elemental compositions of the gas diffusion layer material (carbon cloth and carbon paper, Electrochem, Inc.) were investigated using Energy Dispersive X-ray Spectroscopy (EDS) along with the JSM-6500F, a field emission Scanning Electron Microscope (SEM). Princeton Gamma Tech eXcalibur software was used to analyze the dispersive X-rays. The scanning electron microscope can be divided into different working regions such as the electron optical system, the specimen storage region, the detector area, and the vacuum system (Baker, 2001). The electron optical system contains a Schottky field-emission electron gun, which has a stabilized electron-beam probe with a probe current in the range of pA to 100 nA, and also apertures and a grid cap to control the size and brightness of the electron beam. The most commonly used filament is Tungsten. The specimen storage area is where the specimen is placed relative to the electron beam. Here, the specimen can be manipulated along three axes. In the detector region, electron beams were collected and a signal generated, which was processed in order to record an image or series of peaks that were later analyzed. The vacuum system removes the air molecules in the column using mechanical and diffusion pumps because these molecules can obstruct the electron beam that travels down to the column to interact with the specimen. Air molecules can also impact the number of electrons a detector can pick up. This affects the overall resolution of the instrument.

The column also contains a series of condenser lenses, which were used to control the spot size of beam and also to focus the image on monitor.

The image was obtained when the specimen surface was bombarded with high-energy electrons in a raster pattern. The interaction between the beam and the surface of specimen produced a large number of electrons. The detector then counted the number of electrons emitted and displayed the image on the monitor. The signal was stored in the computer and converted into an image. The Windows NT operating system is used with JEOL specific graphical user interface for smooth and easy operations in all stages from condition-setting to image observation and filing.

4.2.2 Operating Parameters

A small piece of sample (carbon material) was first mounted on a grid using double-sided adhesive carbon tape. The grid was then placed in the specimen chamber of the SEM. The chamber was closed and sufficient time allowed in order to attain the required vacuum inside the column. Once the required vacuum level was reached, the analysis was started. Obtained SEM images and EDS analysis are discussed in the Results and Discussions chapter.

4. 3 Porometry and Porosimetry

Porometry and porosimetry measurements were conducted at Porous Materials, Inc. (Ithaca, NY). The porometry experiments were carried out using a PMI Capillary

Flow Porometer. Mercury and water intrusion porosimetry experiments were carried out using a PMI Mercury/Non-Mercury Intrusion Porosimeter.

4.3.1 Capillary Flow Porometry

Capillary flow porometry was used to assess pore size distribution in a porous sample and to determine characteristic pore dimensions including the largest pore diameter, mean flow pore diameter and smallest pore diameter. This technique was also used to measure the air permeability of the samples. Measurements were performed in both the lateral (through-plane) and transverse (in-plane) directions.

The pores of the sample were filled with galwick (a wetting liquid, perfluorinated polymerized fluorocarbon, surface tension of 15.4 dynes/cm, contact angle of approximately 0°). This fluid fills all of the through and blind pores in the sample, both hydrophobic and hydrophilic. Air was forced to flow through the sample (either wet or dry) under a imposed differential pressure. As the differential pressure increased, the flowrate of the air passing through the sample was measured. The 'dry-curve' was generated using the data from the dry sample, while the 'wet-curve' was generated using the data from the wet sample. The pressure corresponding to the first measurable flow through the wet sample is termed the 'bubble point pressure' and the corresponding bubble point pore diameter is evaluated using (PMI, 2003):

$$D = \frac{4\gamma_{l/g}\cos(\theta)}{P} \tag{4.3.1.1}$$

where D is the pore diameter, $\gamma_{l/g}$ is the surface tension (dyne/cm), θ is the contact angle of the wetting liquid, and P is the pressure. With galwick as the wetting fluid, the cos(θ) term in the numerator is equal to unity. This assumes that pores are cylindrical and, for non-cylindrical pores, a tortuosity factor of ~ 0.7 is used. The bubble point pore diameter represents the largest pore diameter in the sample. Two other pore diameters are also important. The intersection of the 'dry-curve' and the 'wet-curve' on a plot of flowrate as a function of differential pressure represents the smallest pore diameter. A 'half-dry curve' is generated by multiplying the dry sample flowrate by 0.5. The intersection of the 'half-dry curve' with the 'wet-curve' represents the mean flow pore diameter.

Pore size distributions are also evaluated from the obtained data. The PMI-defined pore size distribution, based on wet and dry sample data, is defined as (PMI, 2003):

$$f_F = -\frac{d\left[\left(\frac{F_w}{F_d}\right)*100\right]}{dD} \qquad (4.3.1.2)$$

where F_w and F_d are the wet and dry flow rates, respectively, and D is the pore diameter. A distribution plot with f_F as defined above plotted as a function of pore diameter provides a visual depiction (area) of the percentage of the total flow corresponding to the particular diameter range.

The permeability of air through each sample was also measured using the capillary flow porometer. The sample was mounted into the apparatus, and the air permeability in two primary directions was measured: through-plane and in-plane. In the through-plane measurements, the air was directed towards the entire cross sectional area

($\Pi D^2/4$) of the sample and passed through the sample in the direction of its thickness (L). In the in-plane measurements, the sample is placed between two non-porous barriers. One of these barriers has a small hole drilled in the center and the air flow was directed into this small hole to enter the sample at its center. In order to exit from the sample, the air had to move radially outward to the perimeter surface of the sample (πDL). The permeability was evaluated using Darcy's law (Bird et al., 1960):

$$v = -\frac{k}{\mu}\frac{dP}{dx} \qquad (4.3.1.3)$$

where v is the velocity, k is the permeability coefficient, μ is the fluid viscosity, and dP/dx is the pressure gradient in the direction of flow. Multiplication by the cross sectional area of flow gives the gas flowrate, F. The gas flowrate is then corrected to standard conditions by multiplying by P/P_s, where P is the average pressure (upstream pressure, P_1, plus downstream pressure, P_0, divided by 2), and P_s is the reference pressure (14.7 psia). The pressure gradient is represented as $-(P_1-P_0)/L$. The resulting expression is:

$$k = \frac{2F_sP_s\mu L}{A\left(P_1^2 - P_0^2\right)} \qquad (4.3.1.4)$$

The permeability coefficient has units of area, but is most often reported in Darcy (1 Darcy = 9.87×10^{-9} cm^2).

4.3.2 Mercury/Non-Mercury Porosimetry

Evaluation of the characteristics of the GDL is crucial in correlating physical parameters/characteristics with observed performance of a fuel cell system. The GDL distributes the feed gases to the active catalyst sites and facilitates removal of excess water from the electrodes. The pore size distribution and the degree of hydrophobicity exert significant influence on water transport. Inadequate water transport can impact cell operation through flooding of the catalyst or through dehydration of the membrane.

Porosimetry was used to determine the degree of hydrophobicity of the carbon paper and carbon cloth samples. Water porosimetry was used to quantify the hydrophobic portion of the pores. This included: pore size distribution, mean pore diameter and pore volume. Mercury porosimetry was used to quantify all pores in the sample (both hydrophobic and hydrophilic). Subtraction of these results should yield the hydrophilic component of the sample.

The sample is loaded into the porosimeter and then the system is evacuated to outgas the sample. Mercury is then introduced into the sample chamber under vacuum. The mercury is forced to enter and fill the pores of the sample (intrusion) by increasing the pressure. Both through pores and blind pores are filled. The mercury fills pores of decreasing diameter as the pressure is increased. Assuming cylindrical pores, the diameter of the pores being filled is related to the pressure by the Washburn equation, given as equation (4.3.2.1) (Washburn, 1921):

$$D = -\frac{4\gamma\cos(\theta)}{P} \tag{4.3.2.1}$$

where P is the intrusion pressure, γ is the surface tension of the fluid, θ is the contact angle on the solid surface, and D is the pore diameter. Mercury, with a contact angle of 140°, has a surface tension of 480 dynes/cm. Water porosimetry is also based on this expression, with water having a surface tension of 72 dynes/cm, and a contact angle of 100°. Cumulative pore volume is plotted as a function of pore diameter, yielding the intrusion curve. The total pore volume is given by the total volume of mercury forced into the pores at the highest pressure. The total pore surface area is given by the area above the intrusion curve. The pore size distribution (by volume) is related to the slope of the intrusion curve, as shown in equation (4.3.2.2):

$$F_v = -\frac{dV}{d[\log(D)]} \qquad (4.3.2.2)$$

The area under the pore size distribution curve represents the volume of pores in a specific pore size range.

CHAPTER V

RESULTS AND DISCUSSION

In this chapter, the results obtained from the computational simulations with MATLAB$^{@}$ software are presented. The results of the characterization experiments of the gas diffusion layer are also discussed. In section 5.1, results showing the validation of the model are discussed. The effect of parameters such as cathode gas porosity, operating temperature, cathode gas pressure, and membrane thickness are discussed in section 5.2. The characterization results of the gas diffusion layer from physisorption experiments and scanning electron microscope studies are discussed in detail in sections 5.3 and 5.4. Mercury/non-mercury porosimetry and capillary flow porometry results are presented in section 5.5.

5.1 Model Validation

In this section, the predicted results are compared with those from other models available in the literature to establish the validity of the model developed in this work. Once the model is shown to predict the performance of the PEM fuel cell accurately, the effect of the operating variables on fuel cell performance can be studied.

The results for simulations were obtained assuming that the PEM fuel cell was operating isothermally at 80°C. The main operating and geometric parameters for the base case are presented in Table 5.1. Values for the membrane parameters and properties are given in Table 5.2. Table 5.3 gives the electrode parameters and properties that were used in the model simulations. These values were taken from the work of Bernardi and Verbrugge (1992).

Table 5.1. Parameters for Base-Case Conditions.

Membrane thickness, l_m	0.023 cm
Gas-diffusion-electrode thickness, l_g	0.026 cm
Active-catalyst-layer thickness, l_c	0.001 cm
Cell temperature, T_c	80°C
Oxygen stoichiometric flow, ς_{O_2}	3
Inlet nitrogen-oxygen mole ratio, $\frac{x^0_{N_2}}{x^0_{O_2}}$	3.761904
Air-side pressure, P_c	5 atm
Fuel side pressure. P_a	3 atm

Table 5.2. Base-Case Membrane Parameters and Properties at 80°C.

Parameter	Value & unit
Ionic conductivity, κ	0.17 mho/cm
Proton diffusion coefficient, D_{Hp}	4.5e-5 cm^2/sec
Fixed-charge concentration, c_f	1.2e-3 mol/cm^3
Fixed-site charge, z_f	-1
Dissolved oxygen diffusivity, D_{O_2}	1.22e-6 cm^2/sec
Henry's constant for oxygen, K_{O_2}	2.0e5 atm-cm^3/mol
Electro kinetic permeability, k_ϕ	7.18e-16 cm^2
Hydraulic permeability, k_P	1.8e-14 cm^2
Pore-water viscosity, μ	3.56e-3 gram/cm-sec
Pore-water density, ρ	0.054 mol/cm^3
Saturated vapor pressure, P_w^{sat}	0.467 atm
Water porosity, ε_{wm}	0.28

Table 5.3. Base-Case Electrode Parameters and Properties at 80°C.

Parameter	Value & unit
Electronic conductivity, $\sigma_{\mathrm{eff}}^{\mathrm{d}}$	0.53 mho/cm
Pressure-diffusivity product, $\mathrm{pD}_{\mathrm{O_2-N_2}}$	0.279 atm-cm^2/sec
Pressure-diffusivity product, $\mathrm{pD}_{\mathrm{w-N_2}}$	0.387 atm-cm^2/sec
Pressure-diffusivity product, $\mathrm{pD}_{\mathrm{w-O_2}}$	0.370 atm-cm^2/sec
Cathode gas porosity, $\varepsilon_{\mathrm{g}}^{\mathrm{d}}$	0.4
Membrane porosity in catalyst layer, $\varepsilon_{\mathrm{mc}}$	0.4
Hydraulic permeability, $\mathrm{k}_{\mathrm{p_s}}^{\mathrm{d}}$	4.73e-15 cm^2
Number of electrons, n_c	4
Water stoichiometric coefficient, s_{w}	2
Oxygen stoichiometric coefficient, $\mathrm{s}_{\mathrm{O_2}}$	-1
Proton stoichiometric coefficient, s_{Hp}	-4
Reference kinetic parameter, $\mathrm{ai}_0^{\mathrm{ref}}$	1.0e-5 Amp/cm^3
Cathodic transfer coefficient, α_{c}	2
Anodic transfer coefficient, α_{a}	2
Proton reference concentration, $\mathrm{C}_{\mathrm{Hp}}^{\mathrm{ref}}$	1.2e-3 mol/cm^3
Oxygen reference concentration, $\mathrm{C}_{\mathrm{O_2}}^{\mathrm{ref}}$	3.39e-6 mol/cm^3
Oxygen reference parameter for $\mathrm{i}_0^{\mathrm{c}}, \gamma_{\mathrm{O_2}}$	1
Proton reference parameter for $\mathrm{i}_0, \gamma_{\mathrm{Hp}}$	1/2

5.1.1 Polarization Curve

The PEM fuel cell was assumed to operate at 80°C and the membrane was assumed to be fully hydrated. The open circuit potential of the PEM fuel cell at 80°C was calculated as 1.194 volts. Figure 5.1 compares the calculated cell voltage with the model results of Wu (2003) as a function of current density for the base-case conditions. Anode activation losses were not considered in this model since they contribute only a small amount to the total cell voltage. At lower current density, the cathode activation overpotential due to the oxygen reduction reaction is responsible for the potential loss in the cell. As the current density increases, the ohmic overpotential due to the membrane and the electrodes becomes significant and the activation losses reach a constant value.

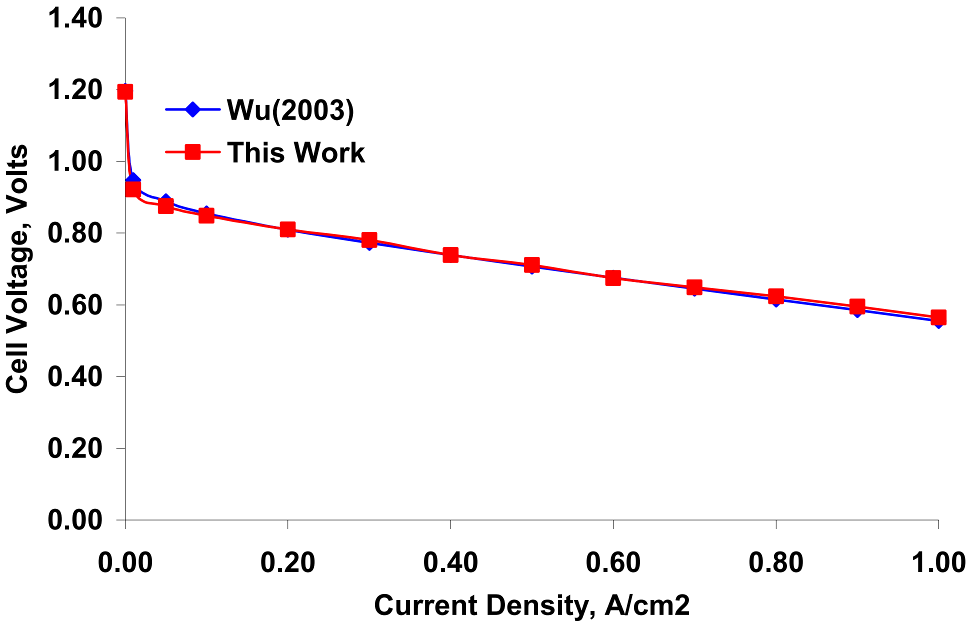

Figure 5.1. Polarization Curve for Base-Case Conditions.

5.1.2 Water Velocity

Figure 5.2 shows the water velocity profiles for the base-case conditions at different current densities. The increase in water velocity at the membrane/catalyst interface is due to the production of water at the cathode by the electrochemical reaction:

$$O_2 + 4H^+ + 4e^- \rightarrow 2H_2O$$

At small current density (0.1 A/cm^2), the net water flow is from the cathode to the anode, as evidenced by the negative water velocity over the entire range of dimensionless distance. The overall transport of water from the cathode to the anode requires that water be supplied at the cathode. At higher current density (0.6 A/cm^2), the net flow direction of the water is reversed. Therefore, water flows out at the cathode, as indicted by the positive velocity in the cathode gas diffuser. This causes drying at the anode and flooding at the cathode side of the fuel cell. Therefore, the fuel gases have to be properly hydrated in order to prevent the dehydration at the anode side of the fuel cell.

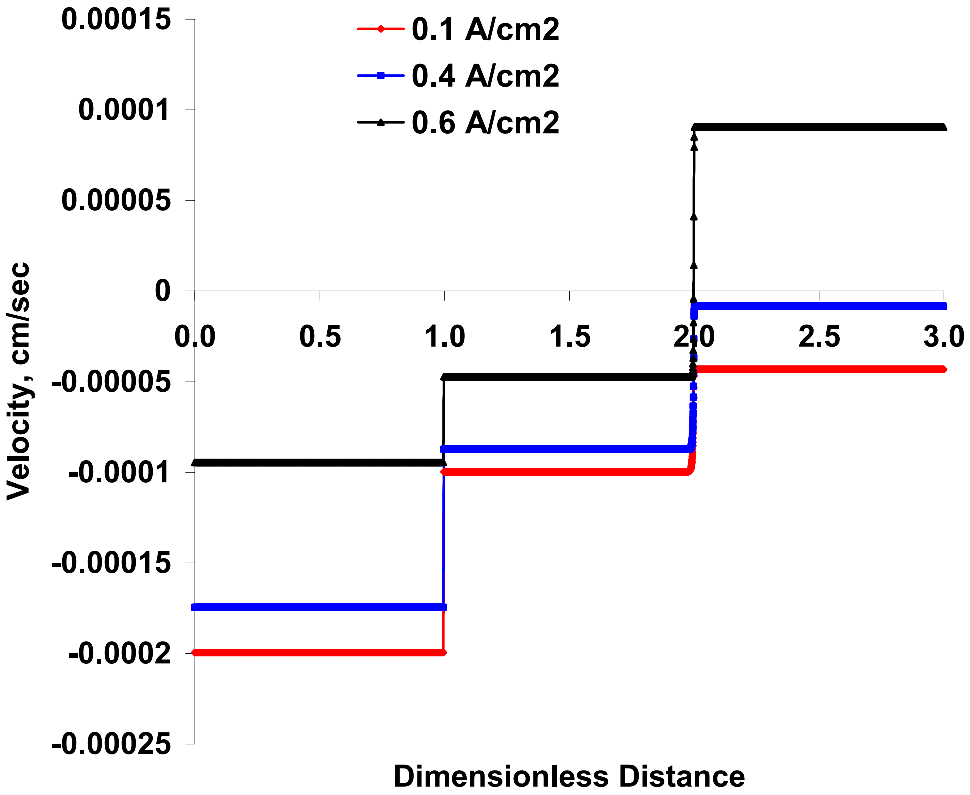

Figure 5.2. Water Velocity Profiles for the Base-Case Conditions.

At moderate current density (0.4 Amp/cm^2), the water flows out from the both sides of the fuel cell, since the velocity is positive on the cathode side and negative on the anode side. At this moderate current density, there would be no need to supply water to the fuel cell.

5.1.3 Hydraulic Pressure

Figure 5.3 shows the hydraulic pressure profiles for the base-case conditions at different current densities. From the slope of these profile in the gas diffuser, the direction of water flow can be determined. A negative slope in the cathode gas diffuser (dimensionless distance between 2 and 3) indicates that water flows from the anode to the cathode. This behavior is observed at higher current density (0.6 Amp/cm^2). In general,

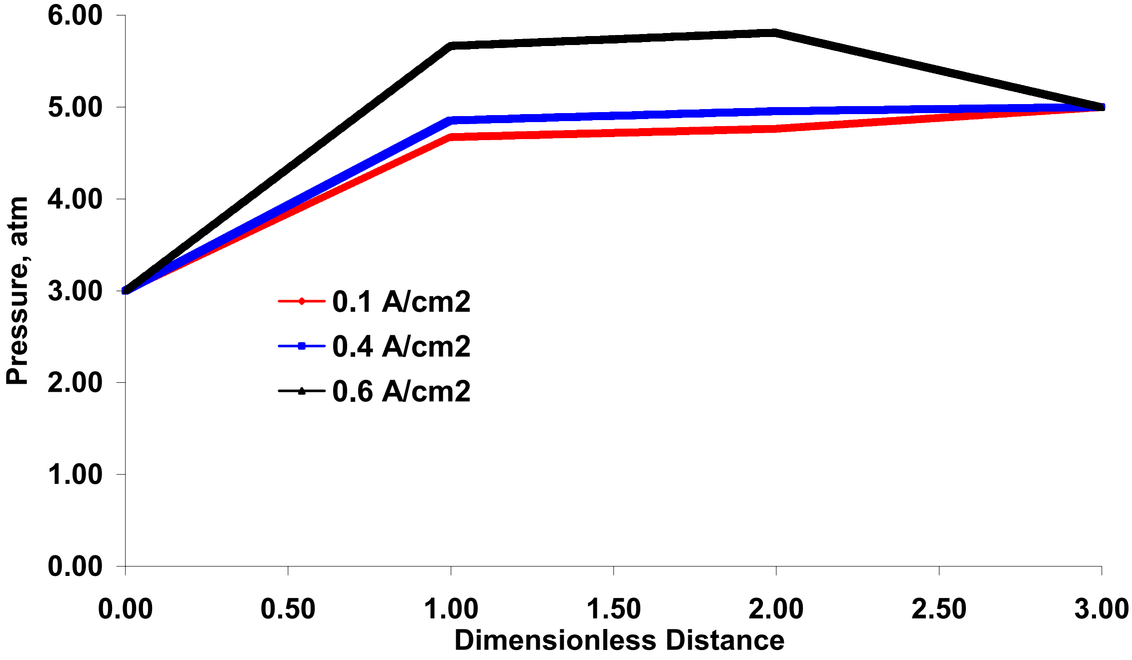

Figure 5.3. Hydraulic Pressure Profiles for the Base-Case Conditions.

the gas diffusion layer plays an important role in maintaining the proper water balance in the fuel cell.

5.1.4 Oxygen Concentration

Figure 5.4 gives the concentration profile of dissolved oxygen in the membrane phase near the membrane/electrode interface on the cathode side of the fuel cell for different current densities at the base-case conditions. The dimensionless distance axis has been expanded to show the region of interest. The dissolved oxygen concentration is depleted at the membrane/catalyst interface due to the electrochemical oxygen reduction reaction. At high current density, the dissolved oxygen gas penetrates only a very small distance into the catalyst layer, thereby using only a small percentage of the available catalyst. At low current density, the dissolved oxygen gas penetrates further into the catalyst layer. These results clearly indicate the low utilization of the catalyst layer at normal operating current densities of the fuel cell. Therefore, optimizing the catalyst loading is essential to efficiently use expensive electrocatalysts. This is an active area of research with efforts directed towards identifying catalyst loading methods that will maximize the catalyst utilization.

5.1.5 Ionic Current Density

The ionic current density distribution within the membrane phase in the membrane region as well as in the catalyst region is shown in Figure 5.5 for different current densities. In the membrane region, the current density is constant and is equal to the operating current density of the PEM fuel cell. In the membrane phase of the catalyst region, the membrane current density gradually decreases to zero at the catalyst/gas-

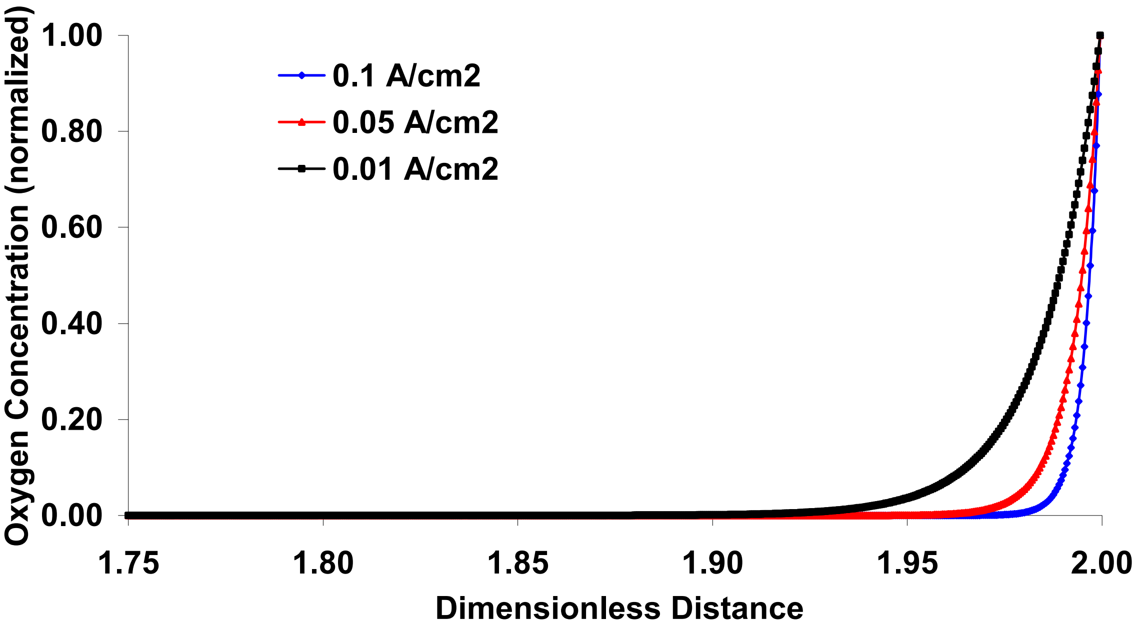

Figure 5.4. Dissolved Oxygen Concentration Profile for the Base-Case Conditions.

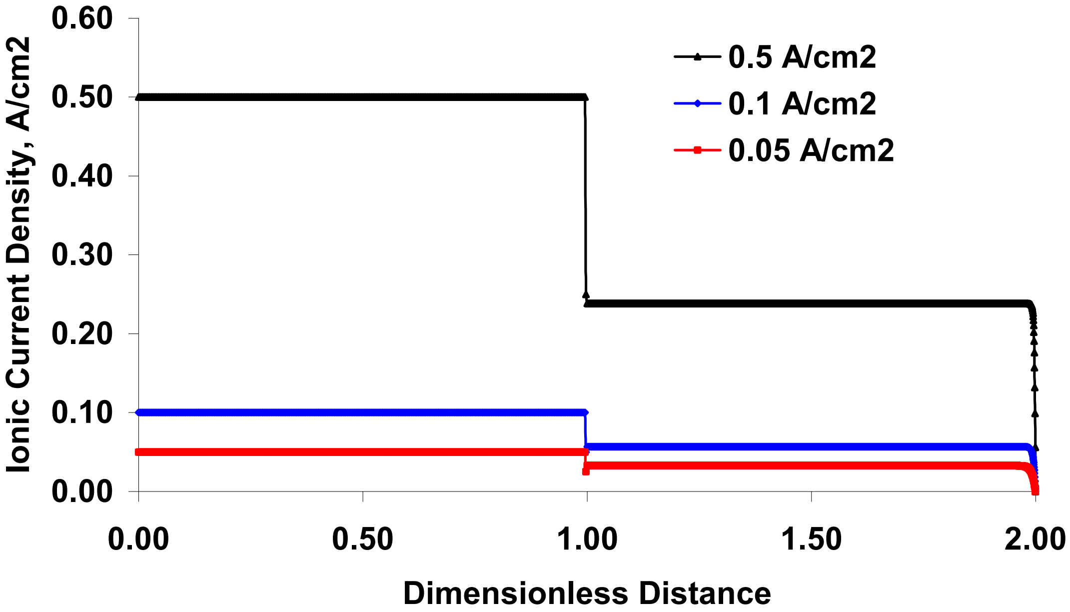

Figure 5.5. Ionic Current Density Profiles for the Base-Case Conditions.

diffuser interface. This is due to the transfer of the membrane phase current density to the solid, electronically conductive phase.

5.2 Effect of Process Parameters on Fuel Cell Performance

In this section, the effects of various parameters on the performance of the PEM fuel cell are presented. Process parameters examined include: cathode gas porosity, operating cell temperature, cathode pressure, and membrane thickness.

5.2.1 Cathode Gas Porosity

Cathode gas porosity has a significant effect on the limiting current of the fuel cell because of mass transfer limitations. Cathode gas porosity is defined as the volume fraction of the gas in the gas diffusion region. For a cathode gas porosity of 0.4, mass transfer losses are not observed. This is demonstrated by the linear potential curve between current densities of 0.2 to 1.0 A/cm^2, as shown in Figure 5.6. With a cathode gas porosity of 0.4, a large portion of the gas diffusion region is available for oxygen transport, and therefore, oxygen transport losses are not observed. However, for low values of the cathode gas porosity, such as 0.11, the oxygen transport is more difficult. This results in a small concentration of dissolved oxygen available at the catalyst layer. This increases the cathode activation losses. This also results in water management problems in the fuel cell due to flooding at the cathode. This flooding forces water into the gas pores, thereby reducing the available pathways for oxygen transport. Porosity affects the concentration overpotential and also has a slight effect on the ohmic overpotential of the fuel cell.

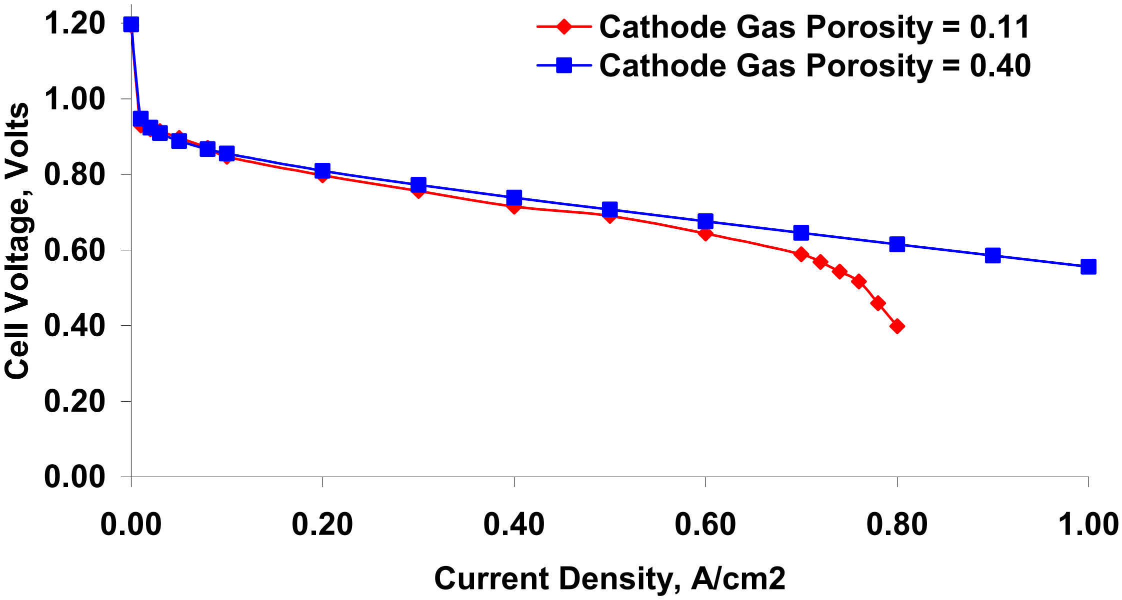

Figure 5.6. Effect of Cathode Gas Porosity.

5.2.2 Cathode Gas Pressure

The effect of cathode gas pressure on the performance of the PEM fuel cell is shown in Figure 5.7. The open circuit potential of the PEM fuel cell increased slightly from 1.190 to 1.194V, as the cathode gas pressure increased from 3 atm to 5 atm. As the pressure is increased, the partial pressure of water remains equal to the saturation pressure of water at the cell operating temperature. Thus, the partial pressure of oxygen increases as does the mole fraction of oxygen as the operating pressure is increased. As a result, the cathode activation overpotential decreases as the cathode gas pressure increases. In the model, the effect of cathode gas pressure on the exchange current density was neglected.

5.2.3 Operating Temperature

The effect of the operating temperature on the performance of the fuel cell is shown in Figure 5.8. Two temperatures were examined: 80°C and 95°C. Operation at higher temperatures increases the ionic conductivity of the membrane, thereby, reducing the ionic resistance in the membrane region. The higher temperature also increased the gas diffusivity. In the model, the effect of operating temperature on the exchange current density was neglected. Increased temperature at fixed operating pressure increases the partial pressure of water if the gas is fully humidified. This results in a decrease in the partial pressures of oxygen and nitrogen at fixed operating pressure. A slight improvement in cell performance over the entire current density range was observed as the operating temperature increased from 80°C to 95°C.

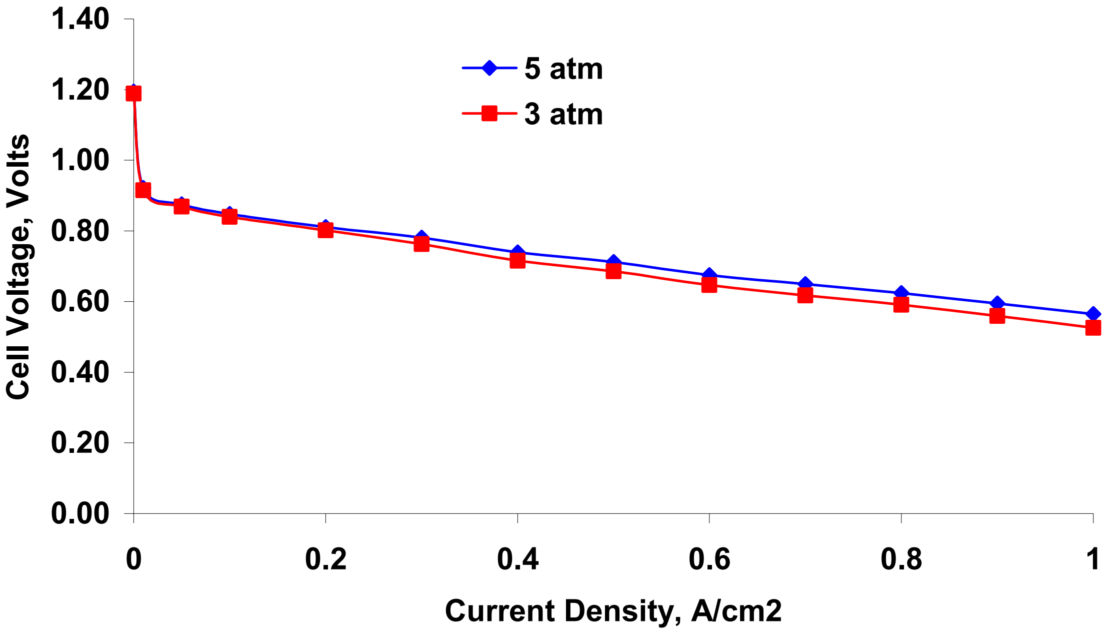

Figure 5.7. Effect of Cathode Gas Pressure on the PEM Fuel Cell Performance.

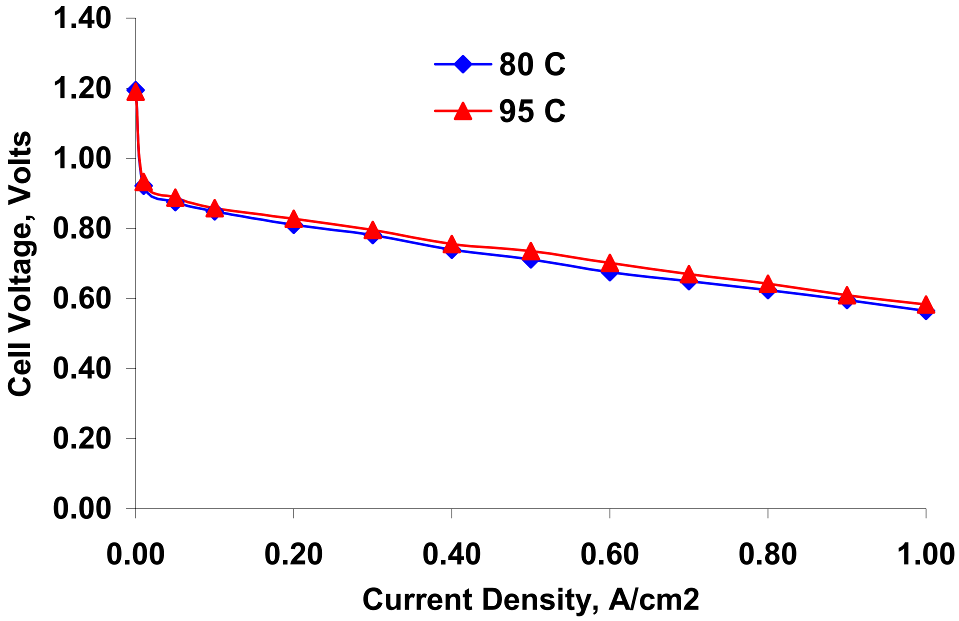

Figure 5.8. Effect of Operating Temperature.

5.2.4 Membrane Thickness

The effect of membrane thickness on the performance of the PEM fuel cell is illustrated in Figure 5.9. The results show the effect of decreasing the membrane thickness from 0.023 cm to 0.0125 cm. The ohmic losses decreased as the membrane thickness decreased. The polarization curve is not significantly changed at low current density, because the activation overpotential is primarily responsible for the potential reduction in cell potential. The ohmic overpotential is a combined result of the resistance to proton transfer across the membrane and the resistance to the electron flow through the electrode materials and the interconnections. The membrane conductivity depends on the membrane thickness as well as the membrane's hydration index. Since the membrane is assumed to be fully hydrated, the cell potential increased as the membrane thickness decreased. The optimum membrane thickness is thus a complex decision. Reducing the membrane thickness results in improved performance. However, the membrane must be thick enough to remain mechanically sound during cell assembly and operation. Fuel crossover from the anode to the cathode is a potential problem if the membrane thickness is too small.

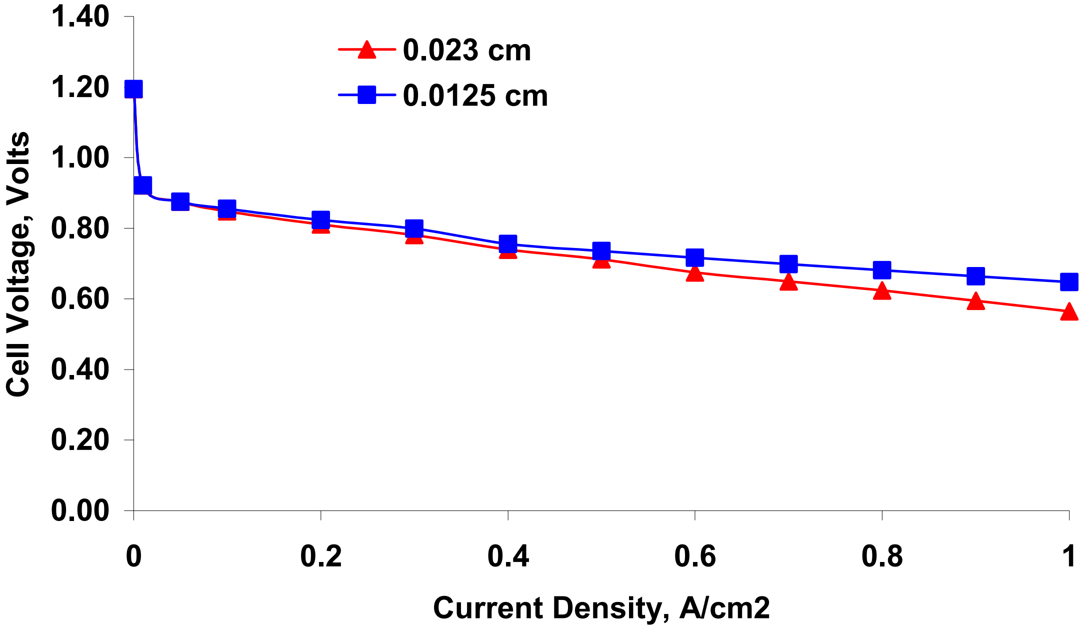

Figure 5.9. Effect of Membrane Thickness.

5.3 Characterization Studies

The gas diffusion layers in PEM fuel cells are typically made from carbon-based materials that are porous. The requirements of an ideal gas diffusion layer include promotion of effective diffusion of the reactant gases to the catalyst sites, good electrical conductivity, and an optimal degree of hydrophobicity for water management. The gas diffusion layers are generally double-layered carbon materials. Commonly used materials for the gas diffusion medium include woven carbon cloth and/or carbon paper. A typical "gas diffusion layer contains a mixture of carbon black powder, hydrophobic material and solvent, applied onto the carbon material to form a micro-porous layer on top of the macro-porous layer" (Williams, 2002). Four different types of materials were examined in these studies. These materials are among those commonly used in the production of gas diffusion medium for fuel cell applications. Carbon paper (untreated and Teflon treated) and carbon cloth (untreated and Teflon treated) from Electrochem, Inc., were examined.

5.3.1 Adsorption Studies

The performance of a gas diffusion medium depends on its ability to efficiently deliver gases (either fuel or oxidant) to the sites where the electrochemical reaction(s) take place. The pore size distribution of a material, therefore, is an extremely important property. In this work, the pore size distribution and the surface area of the four materials were characterized using physisorption.

Physisorption is a neutral process where the gas molecules are adsorbed onto the surface without undergoing any reaction. The most common physisorption method uses nitrogen as the adsorbed species, with adsorption and desorption isotherms measured at liquid nitrogen temperature. The characteristics of the examined materials were quantified using different classical analysis techniques, including: 1) the multi-point BET method; and 2) the BJH method.

The measured adsorption and desorption isotherms are shown in Figures 5.10 to 5.13 for the four materials examined. The adsorption volume increased rapidly at low relative pressure as the nitrogen gas interacted with the first energetic region, followed by

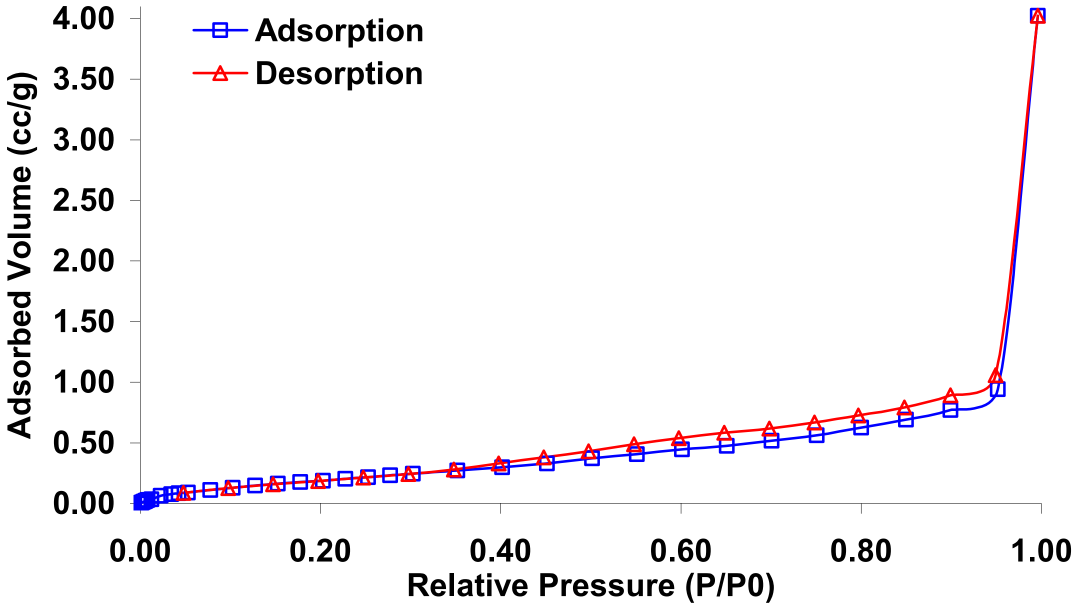

Figure 5.10. Adsorption and Desorption Isotherms for Untreated Carbon Paper.

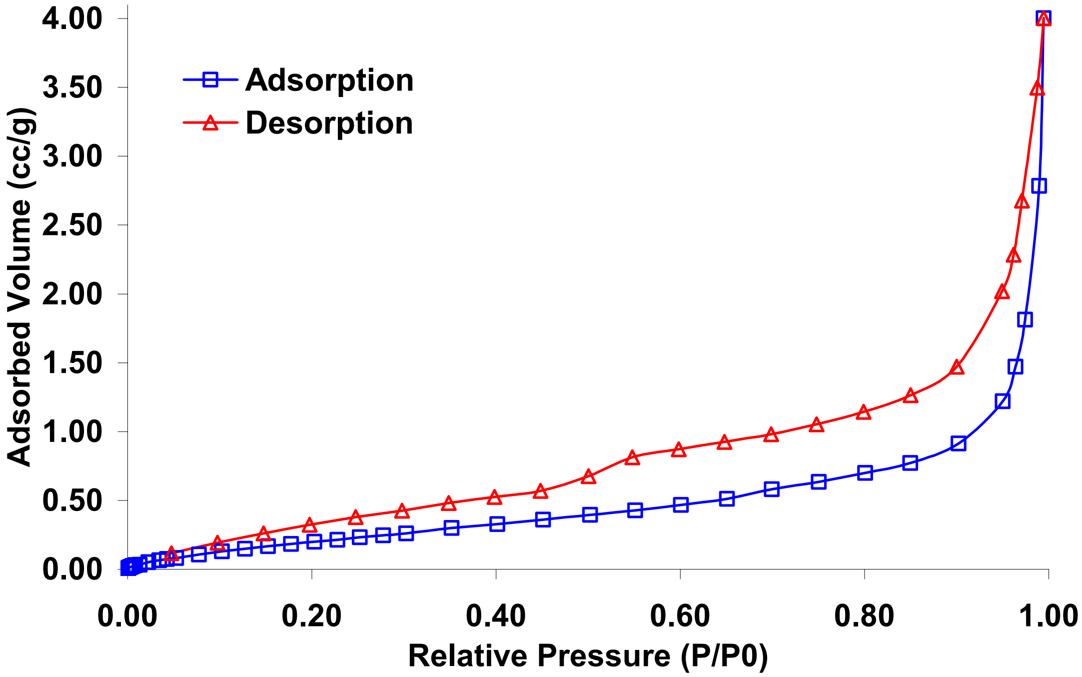

Figure 5.11. Adsorption and Desorption Isotherms for Teflon-Treated Carbon Paper.

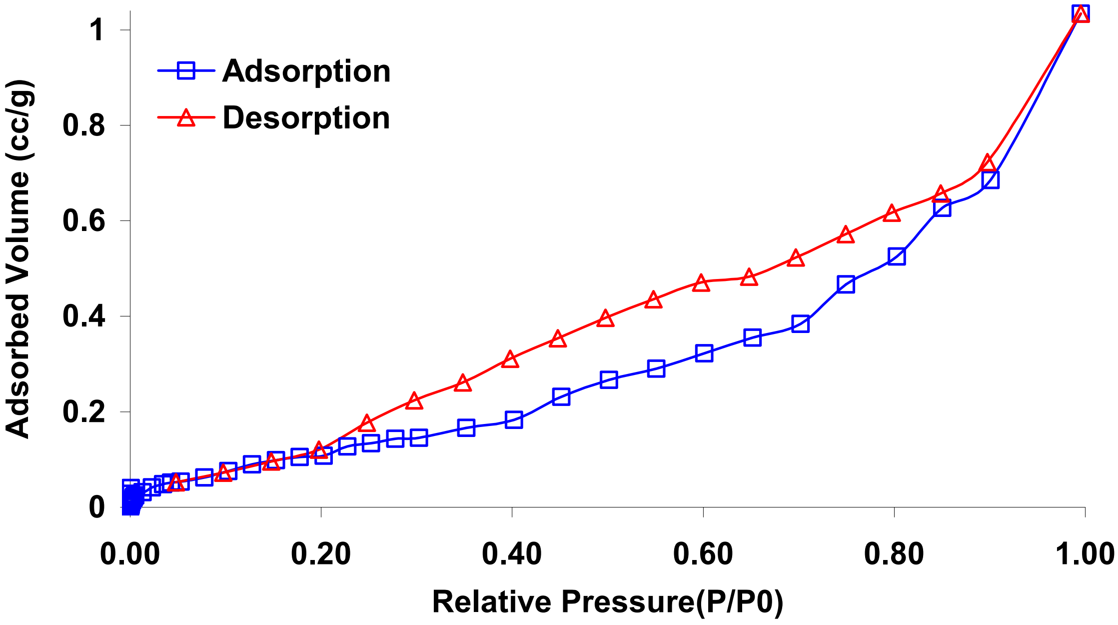

Figure 5.12. Adsorption and Desorption Isotherms for Untreated Carbon Cloth.

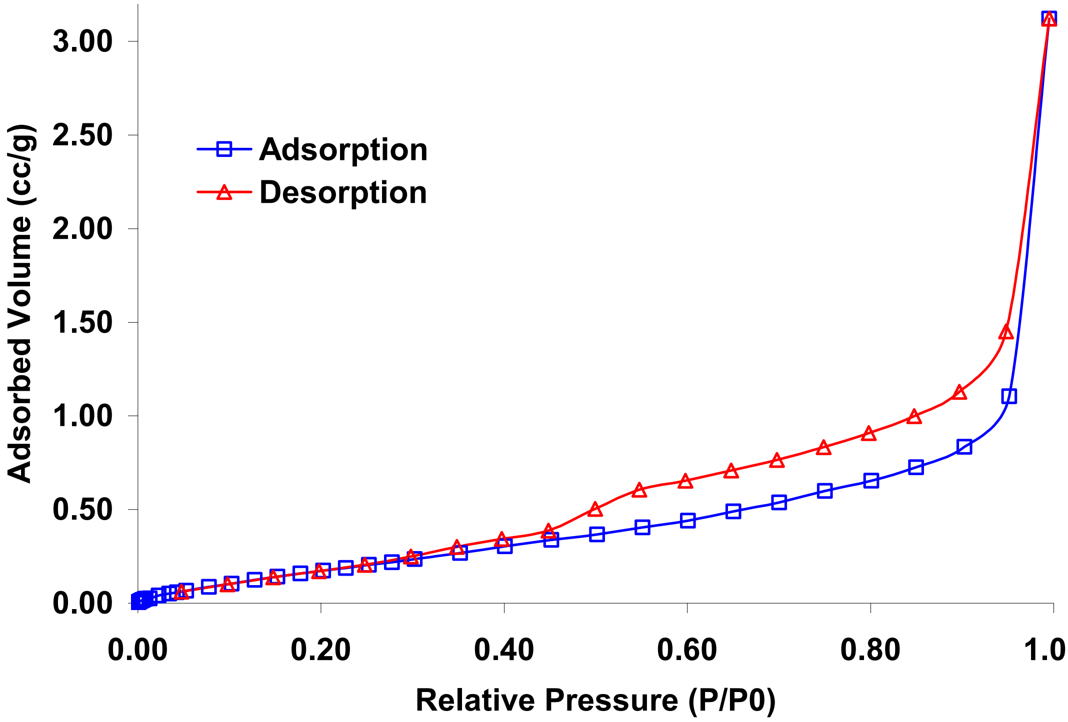

Figure 5.13. Adsorption and Desorption Isotherms for Teflon-Treated Carbon Cloth.

the less energetic region. The rapid increase in adsorbed volume at higher relative pressure (approximately 0.80 and greater) was due to capillary condensation during the adsorption process. The desorption process followed the same series of steps in the reverse direction.

5.3.1.1 BET Method

The multipoint BET plot for the untreated carbon paper, Teflon treated carbon paper, untreated carbon cloth and Teflon treated carbon cloth is shown in Figure 5.14. The BET constant, C, and the surface area derived using the model for the four materials examined are given in Table 5.4.

The BET C constant, which relates the adsorption energy in the monolayer and adsorption-adsorbent interactions, indicates that the attractive forces between the adsorbate and the adsorbent are greater than the attractive forces between gas molecules in the liquefied state. When a monolayer is formed, the fraction of uncovered surface by any gas is a function of the BET C constant (Hill, 1946). A lower C constant correlates with a higher fraction of the surface remaining uncovered. Since Teflon-treated carbon cloth has the lowest C valve, it has the highest fraction of uncovered surface among the materials examined. From the tabulation, it appears that the surface area of Teflon-treated carbon paper and Teflon-treated carbon cloth are higher than those for the untreated carbon paper and untreated carbon cloth. However, since the surface areas of these carbon-based materials are very low (around $1m^2/g$ or less), either krypton (Suzuki, 1982) or argon (Kluson et al., 2001) should be used as the adsorbate (replacing nitrogen) and the experiments repeated to obtain better estimates of the surface area.

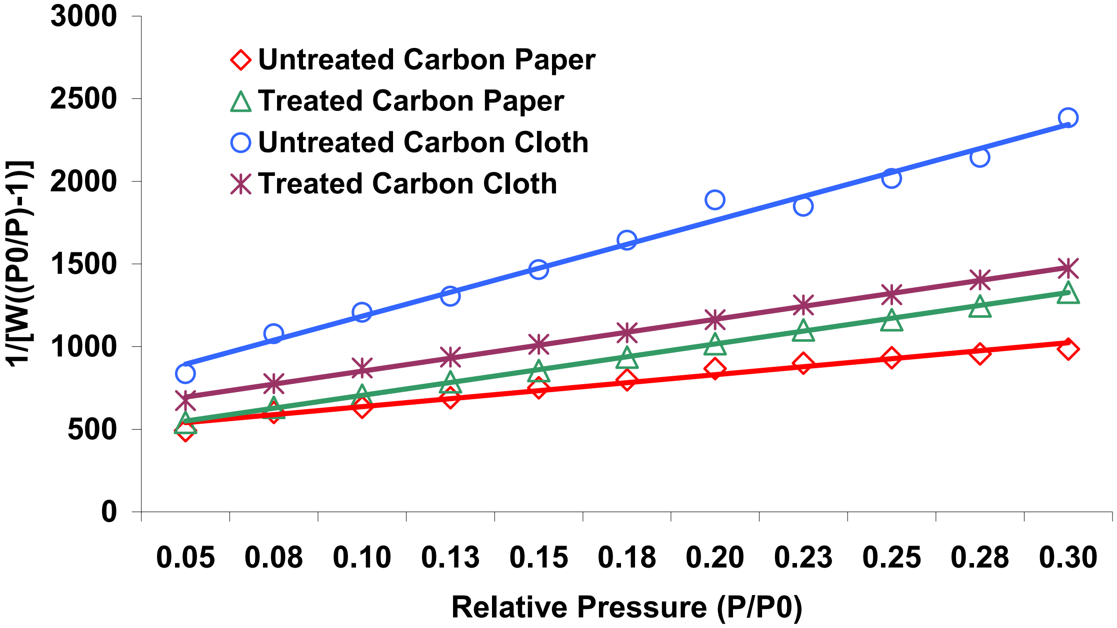

Figure 5.14. BET Model Analysis.

Table 5.4. Summary of BET Model Results.

Material	C constant	Surface Area (m^2/g)	Monolayer weight (g/g)	Uncovered Fraction	Covered fraction by layer 1 after monolayer
Untreated carbon Paper	12.44	0.8737	0.000251	0.2209	0.6070
Teflon-treated carbon paper	9.064	0.9959	0.000286	0.2493	0.5635
Untreated carbon cloth	10.89	0.5444	0.000156	0.2326	0.5889
Teflon-treated carbon cloth	6.925	0.9487	0.000272	0.2754	0.5251

5.3.1.2 BJH Model

The BJH model was used to calculate the pore size distribution and the surface area of the carbon materials. The BJH model is based on the assumptions that pores are open-ended cylindrical pores and are filled with liquid at unity relative pressure. The BJH model provides the relationship between the relative pressure and volume of the capillary condensate using the classical Kelvin equation (Barrett, 1951). The BJH model is applicable in the desorption range from unity relative pressure to a relative pressure of 0.3. A summary of BJH model results is given in Table 5.5. The BJH cumulative desorption surface area was greater than the BET surface area. The plots of desorption pore area and pore volume obtained using the BJH model are shown in Figures 5.15 and 5.16. Both the pore area and the pore volume of Teflon-treated carbon paper were higher than for the other materials. All materials exhibited similar behavior. As the pore size increased, the accumulative pore area of Teflon-treated materials (carbon paper and cloth) rose rapidly compared to the untreated materials. Similarly, the accumulative pore volume of Teflon-treated carbon paper was greatest. The area and volume distributions from the BJH model are shown in Figures 5.17 and 5.18. The distributions do not show any standard distribution curves because the pores are not cylindrical, but irregularly shaped (Barrett, 1951). The maximum in the pore area distribution was located at 19 Å for Teflon-treated carbon cloth, at 21.5 Å for Teflon-treated carbon paper, at 15.21 Å for untreated carbon cloth and at 30.4 Å for untreated carbon paper. Similarly, the maximum in the pore volume distribution was located at 21.5 Å for Teflon-treated carbon paper, at 19.07 Å for Teflon-treated carbon cloth, at 15.21 Å for untreated carbon cloth, and at 30.4 Å for untreated carbon paper.

Table 5.5. Summary of BJH Model Results.

Material	Cumulative Desorption Surface Area (m^2/g)	Cumulative Desorption Pore Volume (cc/g)	Desorption Pore Diameters ($\overset{0}{A}$)
Untreated Carbon Paper	1.157	0.00177	60.80
Teflon-Treated Carbon Paper	1.706	0.004251	43.0
Untreated Carbon Cloth	0.9727	0.00119	30.42
Teflon-Treated Carbon Cloth	1.537	0.00254	38.14

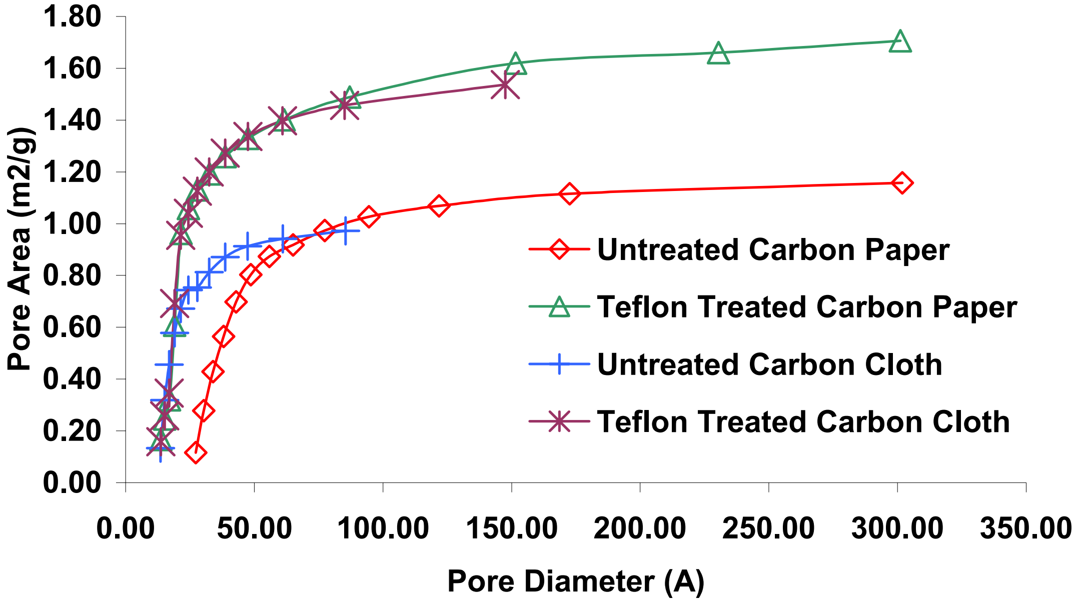

Figure 5.15. BJH Model Accumulative Desorption Pore Area.

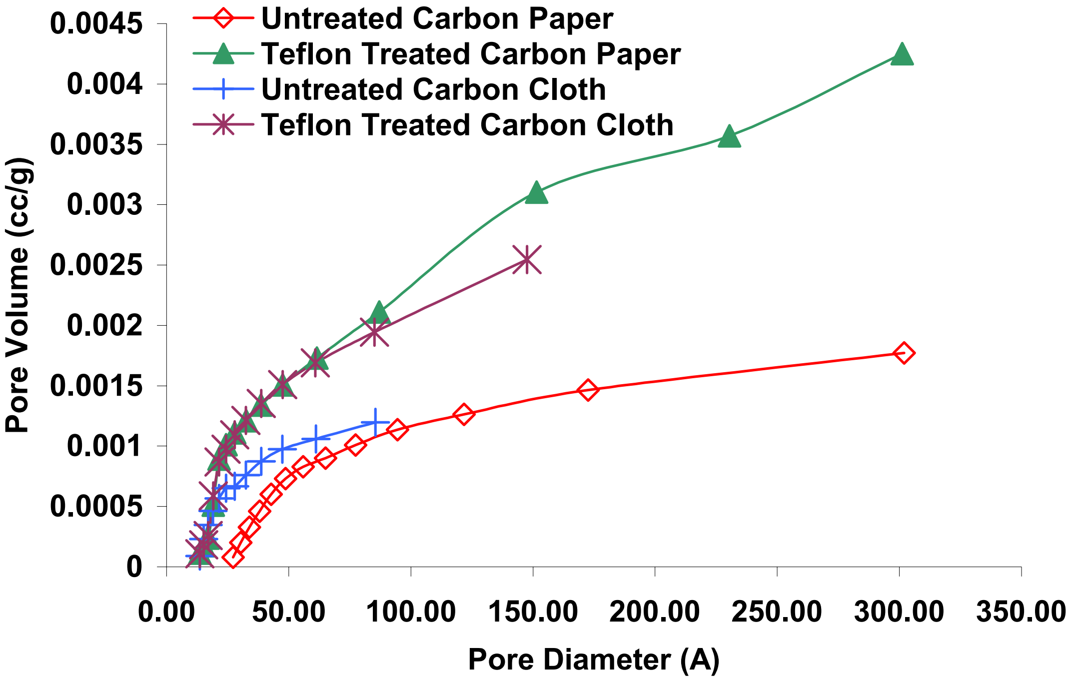

Figure 5.16. BJH Model Accumulative Desorption Pore Volume.

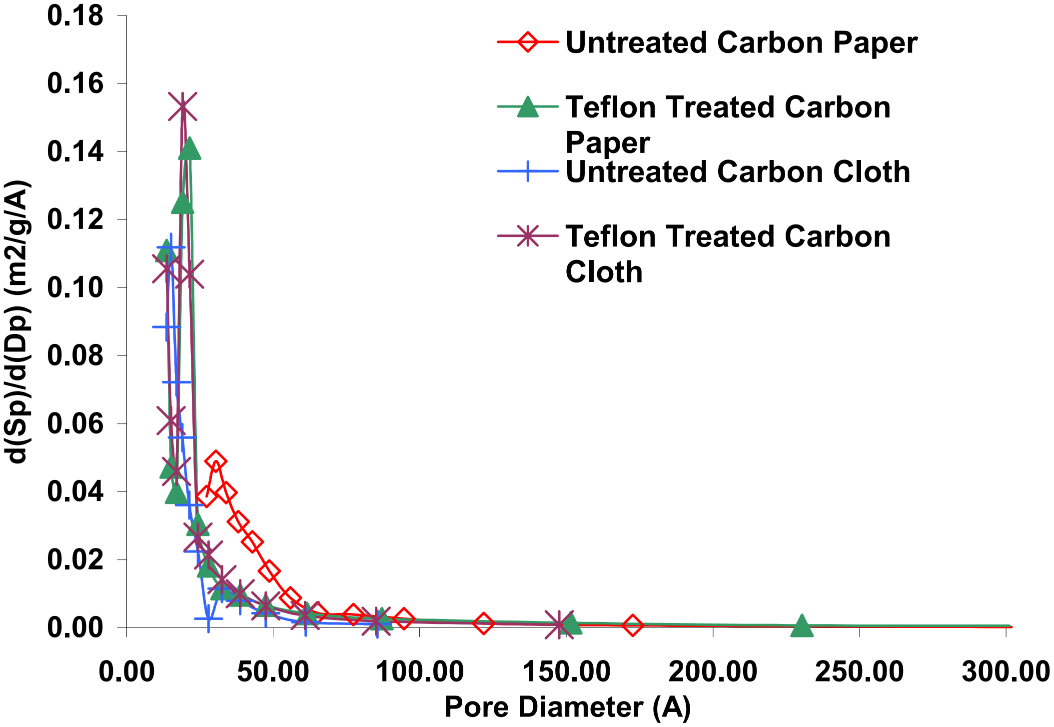

Figure 5.17. BJH Model Desorption Area Distribution.

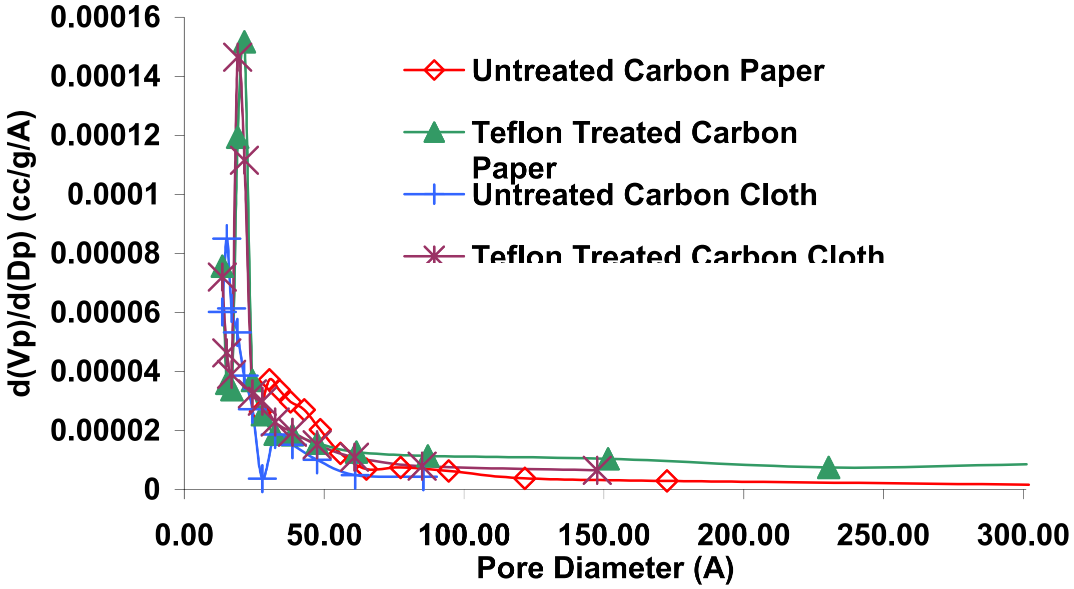

Figure 5.18. BJH Model Desorption Volume Distribution.

5.4 Composition Analysis by EDS

The chemical composition of each sample was obtained using Energy Dispersive X-ray Spectroscopy (EDS). Results of this surface analysis are shown in Table 5.6. The presence of fluorine is indicative of the Teflon coating, and the samples treated with Teflon contain approximately 42% by weight fluorine (Teflon-treated carbon paper) and 21% by weight fluorine (Teflon-treated carbon cloth). These results are qualitative in nature, because SEM micrographs show that the Teflon was not uniformly applied to the entire surface of the sample. These micrographs are discussed in the next section.

Table 5.6. Chemical Composition by EDS.

Material	Carbon		Oxygen		Fluorine		Silicon	
	Weight %	Atom %	Weight %	Atom %	Weight %	Atom %	Weight %	Atom %
Untreated Carbon Paper	96.5	97.43	3.23	2.45	0.0	0.0	0.27	0.12
Teflon-Treated Carbon Paper	57.02	67.67	0.88	0.78	41.93	31.46	0.17	0.09
Untreated Carbon Cloth	96.21	97.38	3.00	2.28	0.0	0.0	0.78	0.34
Teflon-Treated Carbon Cloth	77.25	84.12	1.71	1.40	21.03	14.48	0.0	0.0

5.5 Porometry and Porosimetry Results

5.5.1 Pore Characterization

Capillary flow porometry was performed on four samples: 1) untreated carbon cloth; 2) Teflon-treated carbon cloth; 3) untreated carbon paper; and 4) Teflon-treated carbon paper. These samples were purchased from Electrochem, Inc. (Woburn, MA).

The air permeability in two primary flow directions was measured for each of the samples using capillary flow porometry. The samples were circular, with a measured diameter, D, and thickness, L. For in-plane analysis, the air is introduced at the center of the sample, and must flow to the sample perimeter surface to exit. Thus, the flow is perpendicular to the sample thickness. For through-plane analysis, the air in introduced to the face of the circular sample, and flows through the thickness of the sample to the downstream face. Each type of analysis, in-plane and through-plane, provides information regarding characteristic pore dimensions in the direction of flow.

SEM micrographs of the samples provide further insight into the structure of each sample in the two distinct directions. SEM micrographs for untreated carbon cloth are shown in Figures 5.19 and 5.20, and represent the in-plane view and the through-plane view, respectively. A preferential direction is observed for both the in-plane view, and the through-plane view. The magnification of the images is too great to allow the weave of the cloth to be seen in the figures. The fibers in the sample have diameters on the order of 8 microns.

SEM micrographs for Teflon-treated carbon cloth are shown in Figures 5.21 and 5.22, and represent the in-plane view and the through-plane view. In Figure 5.21, the sample was slightly tilted to show both the in-plane view as well as the Teflon coating on the surface. The weave of the cloth is also visualized in this micrograph. From the micrograph, it appears that Teflon has been applied to both planar surfaces of the carbon cloth. In Figure 5.22, it is evident that the Teflon coating is not uniform at all and small regions contain a great deal of Teflon, while other regions contain none. The regular weave of the cloth also gives rise to large pores in the through-plane direction of flow.

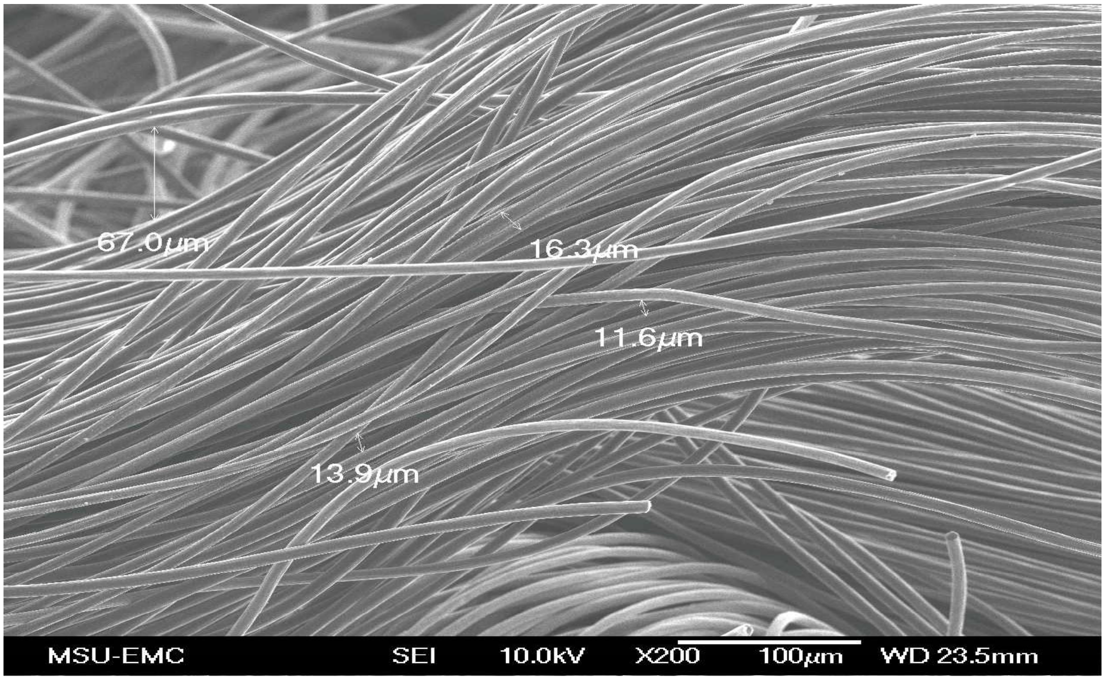

Figure 5.19. SEM Image of Untreated Carbon Cloth (In-Plane View).

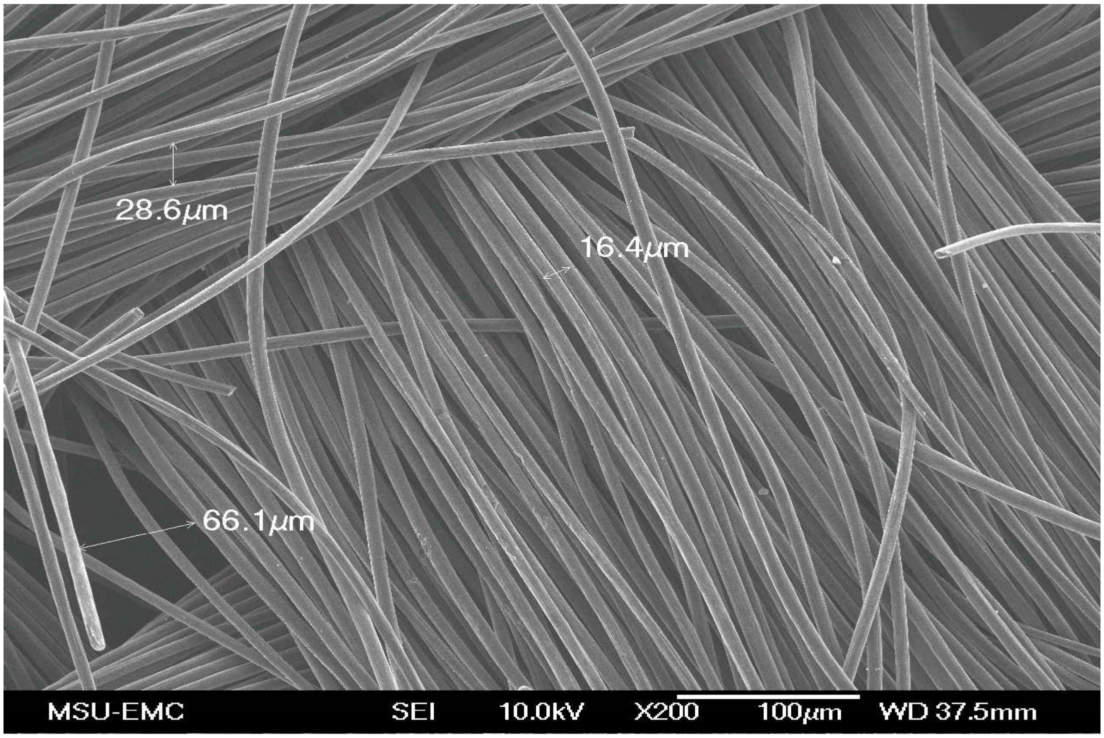

Figure 5.20. SEM Image of Untreated Carbon Cloth (Through-Plane View).

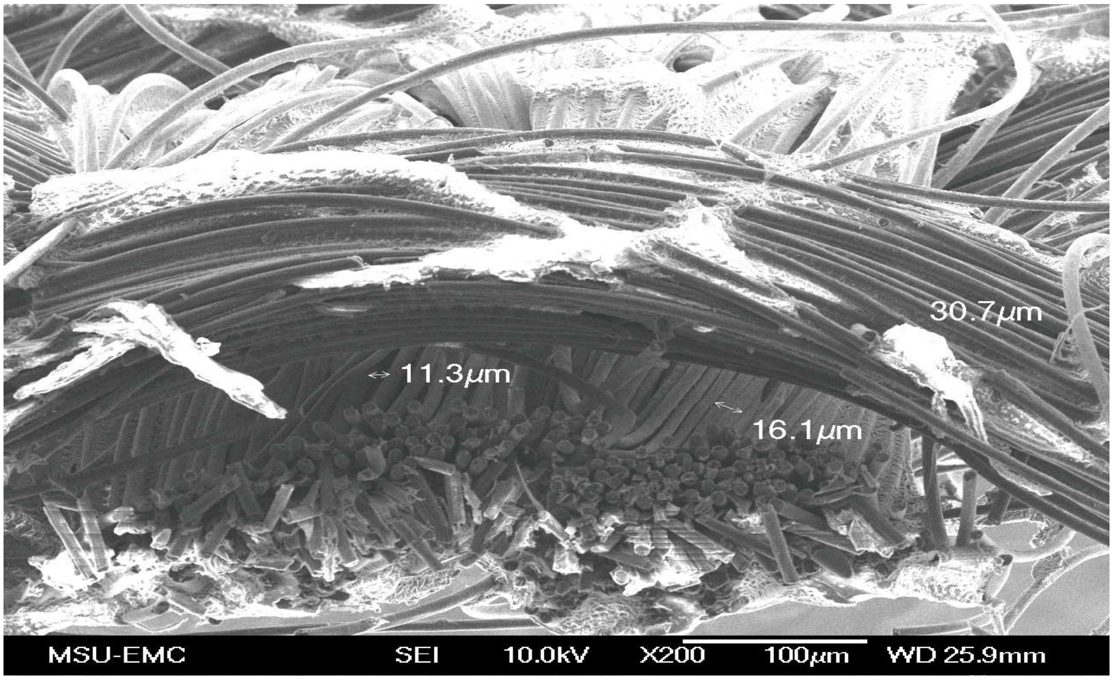

Figure 5.21. SEM Image of Teflon-Treated Carbon Cloth (In-Plane View).

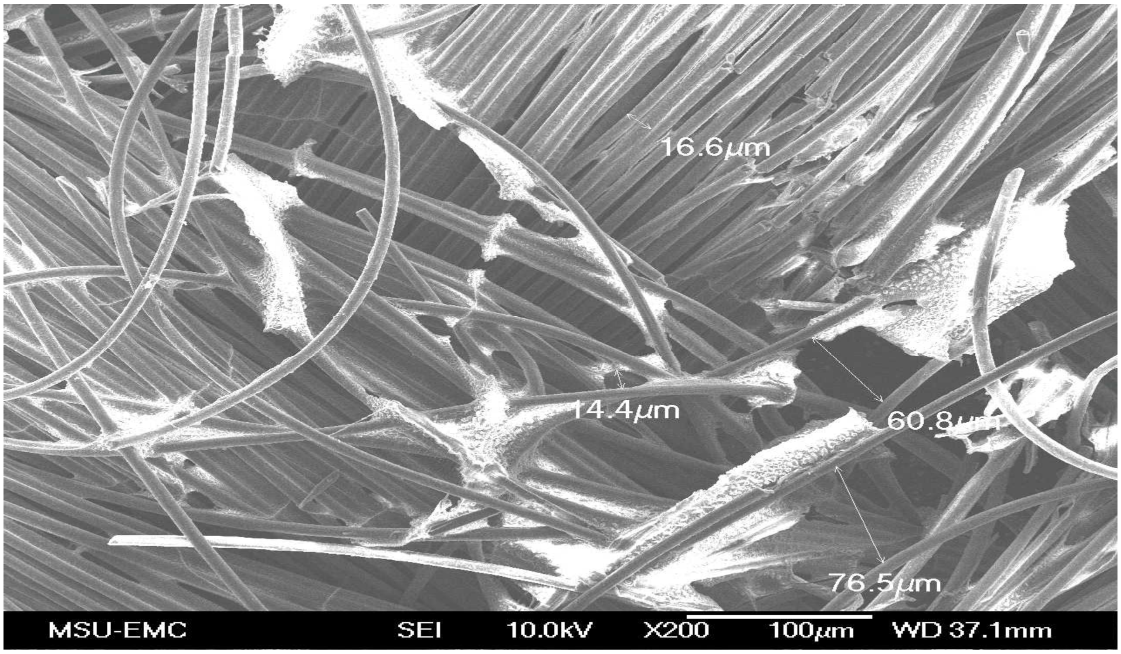

Figure 5.22. SEM Image of Teflon-Treated Carbon Cloth (Through-Plane View).

Figure 5.23 provides the results of the in-plane capillary flow porometry measurements for the untreated carbon cloth. There are a number of important features on this plot that can be used to characterize the pore structure in the sample. Three curves are plotted: 1) wet curve; 2) dry curve; and 3) half-dry curve. The pressure required to initiate air flow through the wetted sample is known as the 'bubble point' pressure and the corresponding diameter is the bubble point pore diameter. For the untreated carbon cloth, the bubble point pore diameter was 6.02 microns. The intersection of the wet curve and the dry curve occurs at elevated pressure and is associated with the smallest pore diameter. For the untreated carbon cloth, the smallest pore diameter was 0.18 microns. The intersection of the wet curve and the half-dry curve is associated with the mean flow pore diameter. The mean flow pore diameter for the untreated carbon cloth was 2.05 microns.

Figure 5.24 provides the results of the in-plane capillary flow porometry measurements for the Teflon-treated carbon cloth. The bubble point pore diameter was 11.49 microns, which corresponds to a smaller pressure required to initiate air flow through the wet sample compared to the untreated carbon cloth. The mean flow pore diameter was 2.095 microns, which was approximately equal to that measured for the untreated carbon cloth. The flow rate through the sample was much larger for the Teflon-treated carbon cloth compared to the untreated carbon cloth. For example, at a differential pressure of 25 psi, the dry curve flow rate was approximately 6 L/min for the Teflon-treated carbon cloth, while for the untreated carbon cloth, the dry curve flow rate was only 1.5 L/min. For the Teflon-treated carbon cloth, the wet and dry curves do not

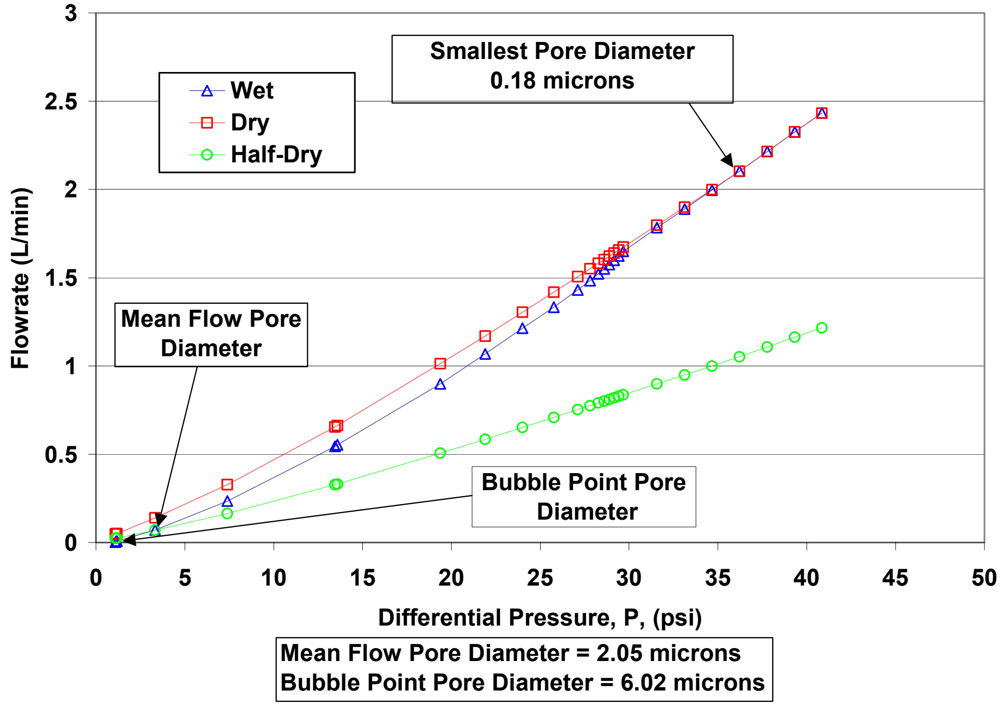

Figure 5.23. Wet, Dry and Half-Dry Curves for Untreated Carbon Cloth (In-Plane Analysis).

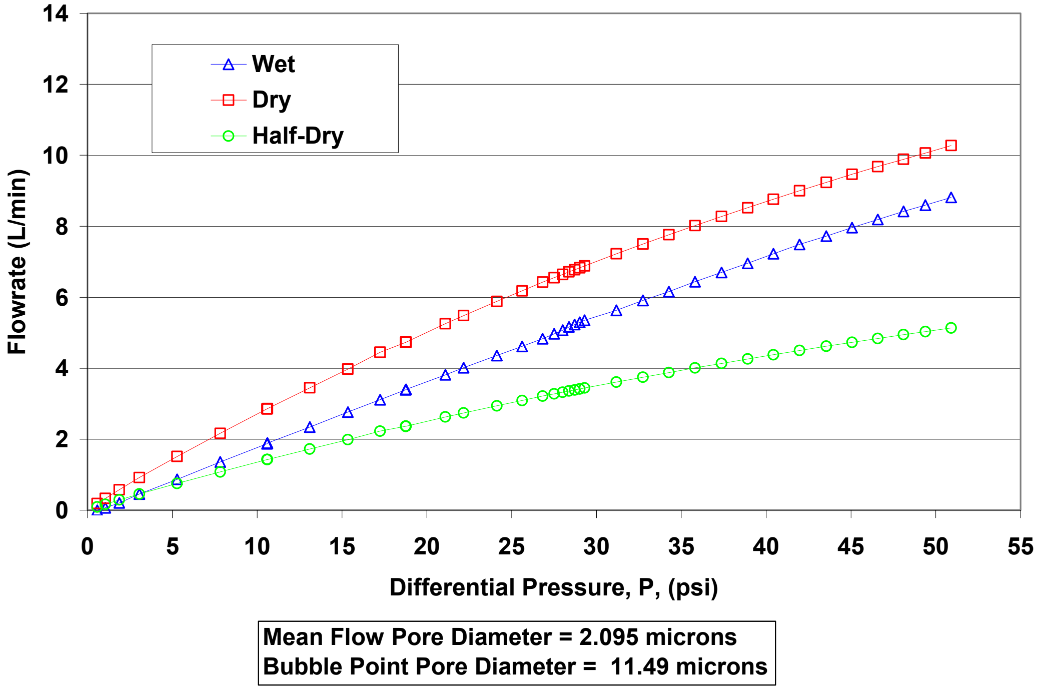

Figure 5.24. Wet, Dry and Half-Dry Curves for Teflon-Treated Carbon Cloth (In-Plane Analysis).

intersect. This implies that not all pores in the wet sample are emptied (PMI, 2003). Extending the pressure range examined might result in the intersection of the wet and dry curves.

Figure 5.25 provides the results of the through-plane capillary flow porometry measurements for the untreated carbon cloth. The flow rates of air through the sample are markedly higher over a very small pressure range compared to the in-plane results. The maximum pressure was only 0.8 psi. The mean flow pore diameter was 28.55 microns, while the bubble point pore diameter was 125.95 microns. The pore diameters are significantly greater than those obtained for the same sample in the in-plane analysis. This is expected because of the woven nature of the carbon cloth, which results in much larger openings through which the air can pass easily through the sample.

Figure 5.26 provides the results of the through-plane capillary flow porometry measurements for the Teflon-treated carbon cloth. Similar behavior is observed with respect to air flow rate and pressure. The mean flow pore diameter is slightly larger, at 42.94 microns, compared to that for the untreated carbon cloth. The bubble point pore diameter is also greater at 167.01 microns.

Figures 5.27 and 5.28 show the normalized pore size distributions for untreated carbon cloth and Teflon-treated carbon cloth, respectively, from both in-plane and through-plane analysis. The average dimensions of the pores in the in-plane direction are much smaller than in the through-plane direction for both untreated and Teflon-treated carbon cloth.

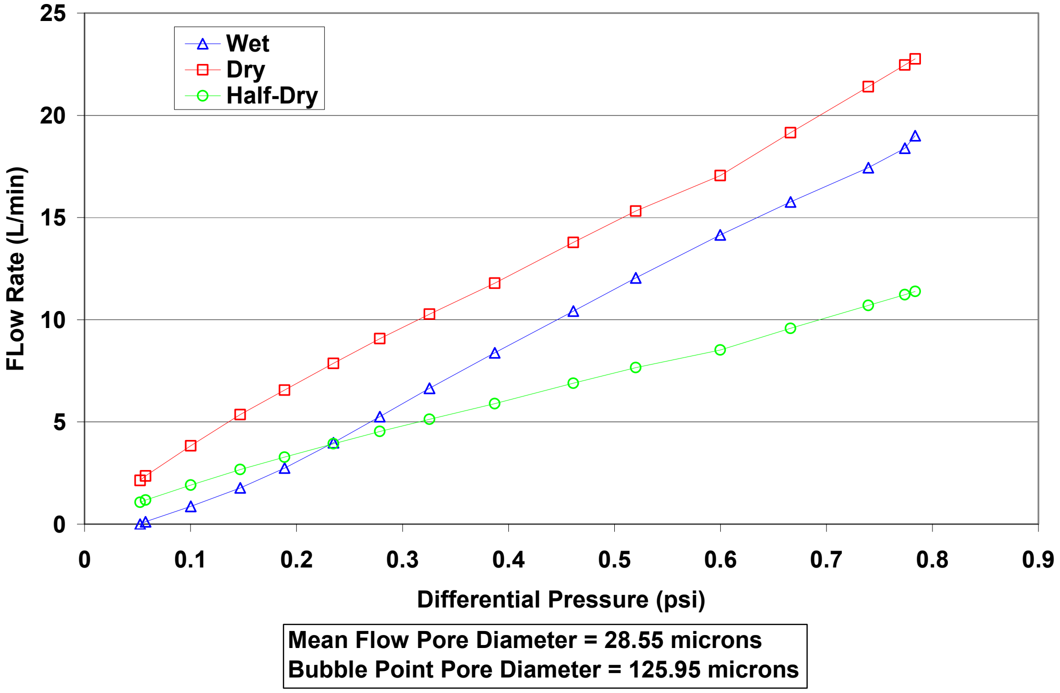

Mean Flow Pore Diameter = 28.55 microns
Bubble Point Pore Diameter = 125.95 microns

Figure 5.25. Wet, Dry and Half-Dry Curves for Untreated Carbon Cloth (Through-Plane Analysis).

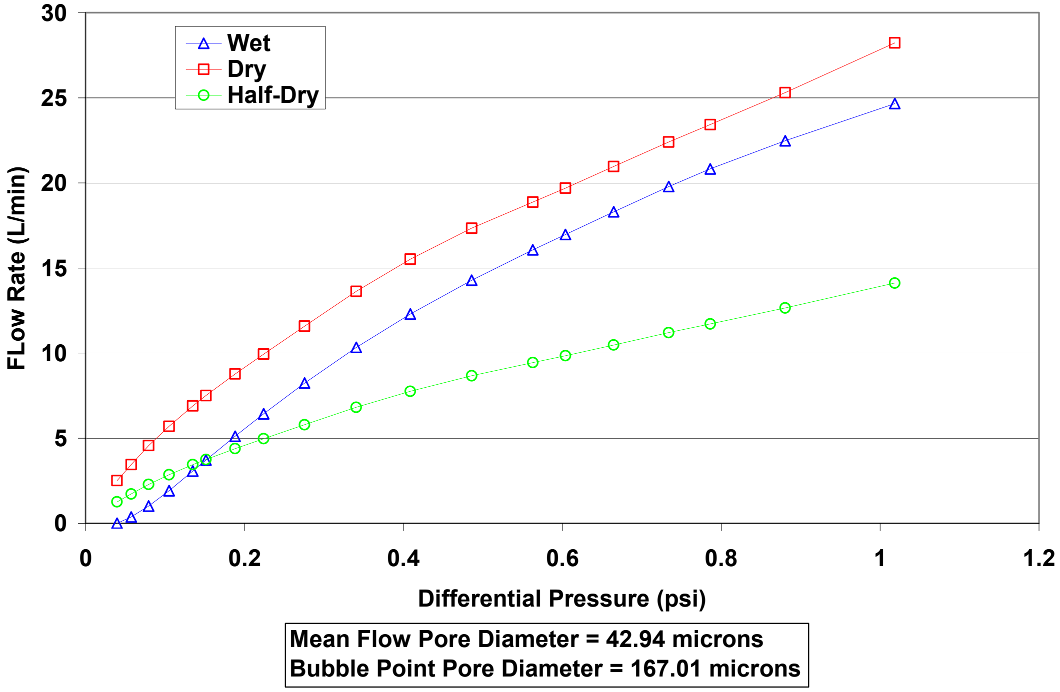

Mean Flow Pore Diameter = 42.94 microns
Bubble Point Pore Diameter = 167.01 microns

Figure 5.26. Wet, Dry and Half-Dry Curves for Teflon-Treated Carbon Cloth (Through-Plane Analysis).

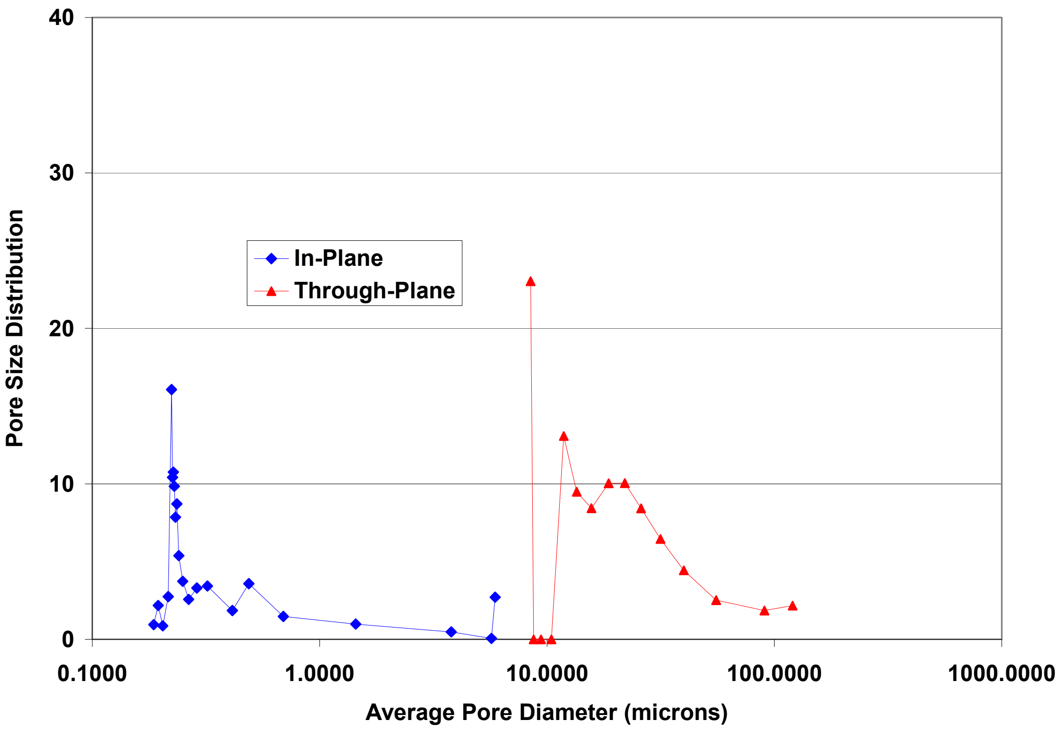

Figure 5.27. Normalized Pore Size Distributions for Untreated Carbon Cloth (Capillary Flow Porometry – Through Pores).

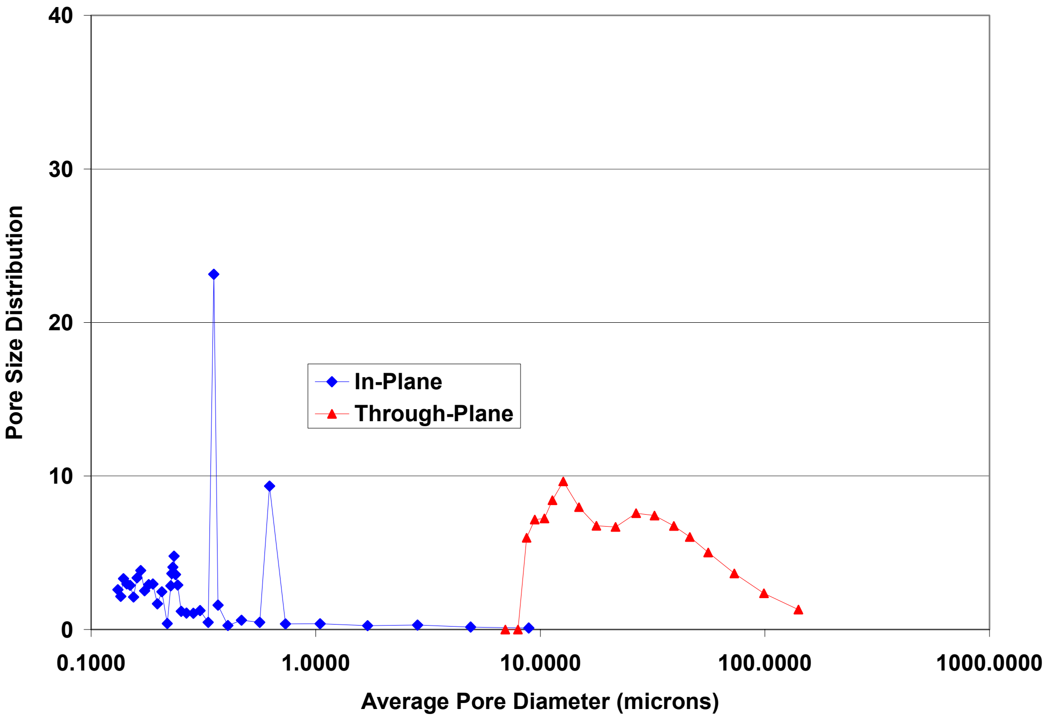

Figure 5.28. Normalized Pore Size Distributions for Teflon-Treated Carbon Cloth (Capillary Flow Porometry – Through Pores).

SEM micrographs for the untreated carbon paper are shown in Figures 5.29 and 5.30 and represent the in-plane view and the through-plane view, respectively. As noted by others, the fibrous structure of carbon paper is very complex on the microscopic scale, with a wide range of pore diameters existing in the structure (Wang, 2003). This is distinctively different from the more-ordered structure of the carbon cloth.

Figures 5.31 and 5.32 are SEM micrographs of the Teflon-treated carbon paper for the in-plane view and the through-plane view, respectively. From comparison of Figures 5.29 and 5.31, it appears that the Teflon treatment has been applied only to one surface of the carbon paper. The degree of adhesion between the Teflon and the fibers also appears to be increased compared to the Teflon and the carbon cloth. The Teflon coating also appears to be more uniformly distributed across the carbon paper surface. The average fiber diameter in the carbon paper is on the order of 7 microns.

Figure 5.33 provides the results of the in-plane capillary flow porometry measurements for the untreated carbon paper. For the untreated carbon paper, the bubble point pore diameter was 13.98 microns. This is approximately twice as large as that obtained for the untreated carbon cloth. The mean flow pore diameter for the untreated carbon paper was 1.89 microns, which was approximately the same as that for the untreated carbon cloth.

Figure 5.34 provides the results of the in-plane capillary flow porometry measurements for the Teflon-treated carbon paper. The bubble point pore diameter was 6.89 microns, while the mean flow pore diameter was 1.48. The smallest pore diameter was 0.23 microns.

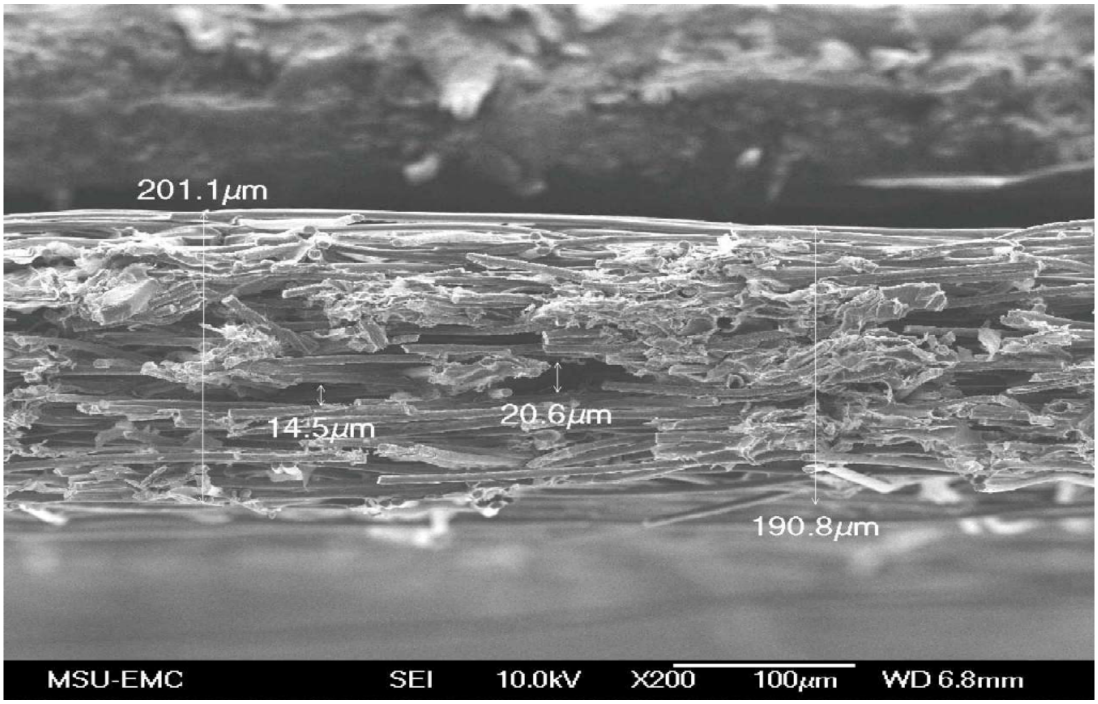

Figure 5.29. SEM Image of Untreated Carbon Paper (In-Plane View).

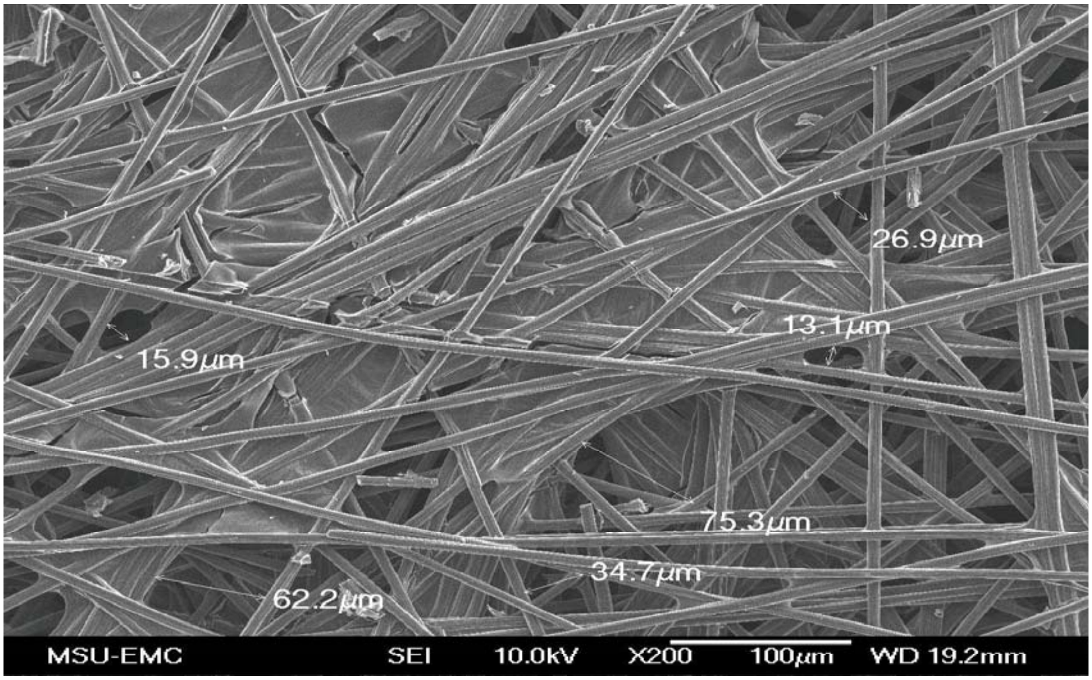

Figure 5.30. SEM Image of Untreated Carbon Paper (Through-Plane View).

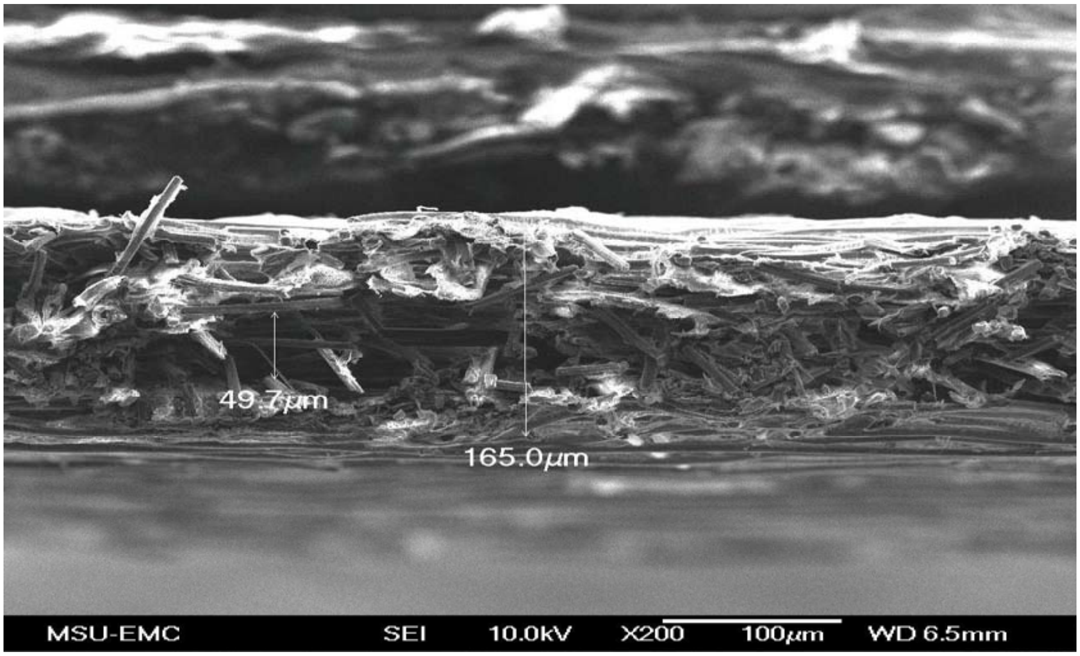

Figure 5.31 SEM Image of Teflon-Treated Carbon Paper (In-Plane View)

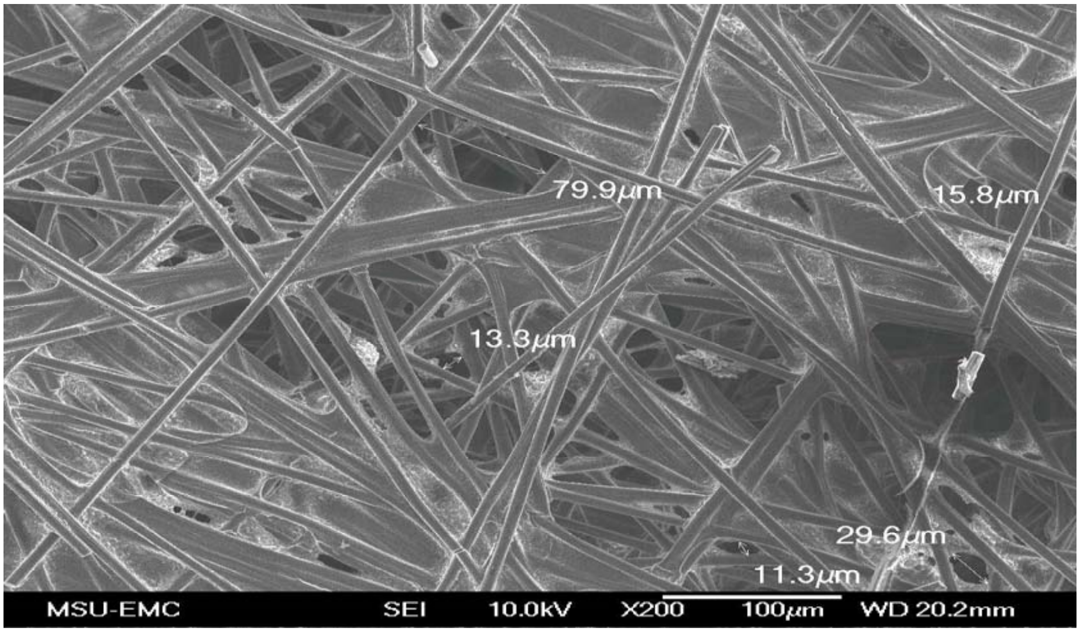

Figure 5.32 SEM Image of Teflon-Treated Carbon Paper (Through-Plane View)

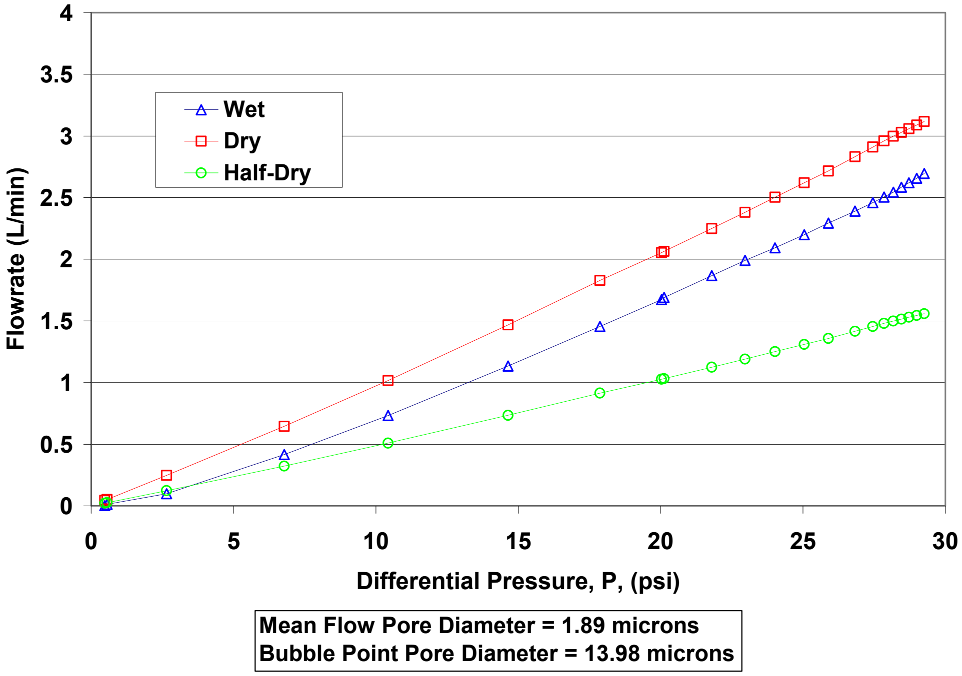

Mean Flow Pore Diameter = 1.89 microns
Bubble Point Pore Diameter = 13.98 microns

Figure 5.33. Wet, Dry and Half-Dry Curves for Untreated Carbon Paper (In-Plane Analysis).

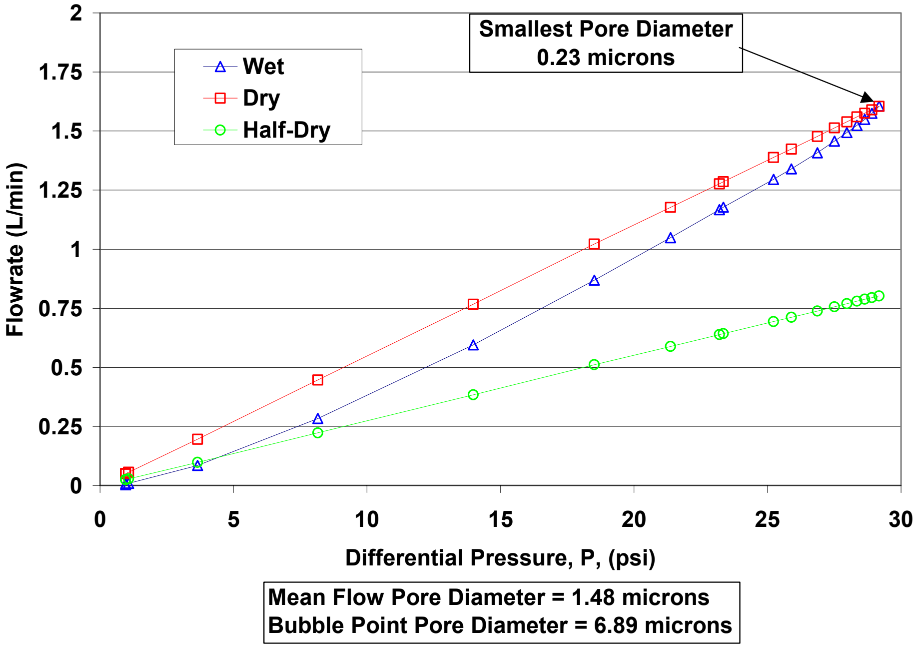

Smallest Pore Diameter
0.23 microns

Mean Flow Pore Diameter = 1.48 microns
Bubble Point Pore Diameter = 6.89 microns

Figure 5.34. Wet, Dry, and Half-Dry Curves for Teflon-Treated Carbon Paper (In-Plane Analysis).

Figure 5.35 provides the results of the through-plane capillary flow porometry measurements for the untreated carbon paper. Again, similar to the results for carbon cloth, the flow rates of air through the sample are markedly higher over a very small pressure range compared to the in-plane results. The mean flow pore diameter was 18.43 microns, while the bubble point pore diameter was 35.59 microns. The pore diameters are significantly greater than those obtained for the same sample in the in-plane analysis.

Figure 5.36 provides the results of the through-plane capillary flow porometry measurements for the Teflon-treated carbon paper. Similar behavior is observed with respect to air flow rate and pressure. The mean flow pore diameter is approximately equal, at 18.42 microns, compared to 18.43 microns for the untreated carbon paper. The bubble point pore diameter is only slightly greater at 40.29 microns.

Figures 5.37 and 5.38 show the normalized pore size distributions for untreated carbon paper and Teflon-treated carbon paper, respectively, from both in-plane and through-plane analysis. The average dimensions of the pores in the in-plane direction are much smaller than in the through-plane direction for both untreated and Teflon-treated carbon paper.

5.5.2 Evaluation of Average Gas Permeability

The capillary flow porometry measurements also provide the data necessary to evaluate the average permeability coefficient, reported in Darcy. Values for the average permeability coefficient from the in-plane analysis of the four samples studied are provided in Figure 5.39. The average permeability coefficients range from

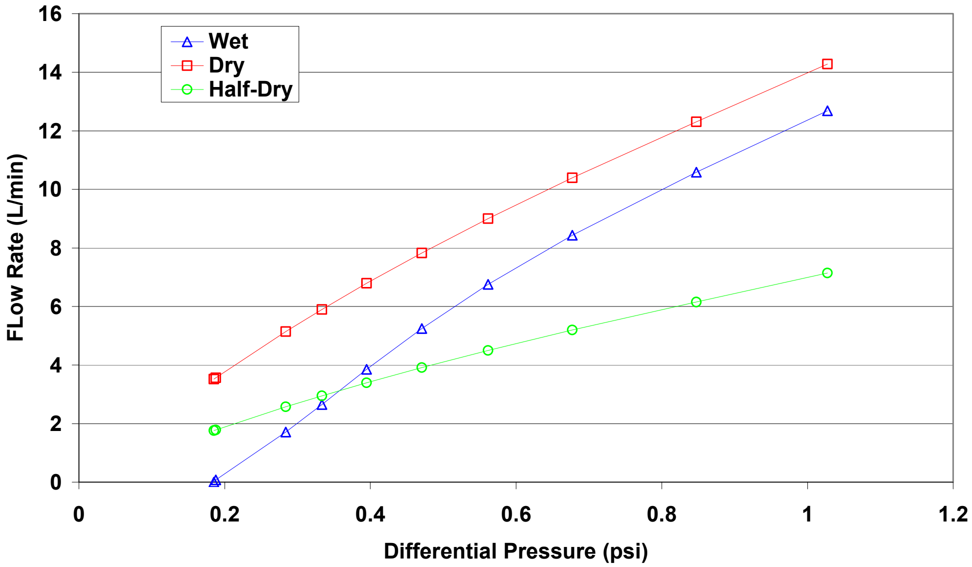

Mean Flow Pore Diameter = 18.43 microns
Bubble Point Pore Diameter = 35.59 microns

Figure 5.35. Wet, Dry and Half-Dry Curves for Untreated Carbon Paper (Through-Plane Analysis).

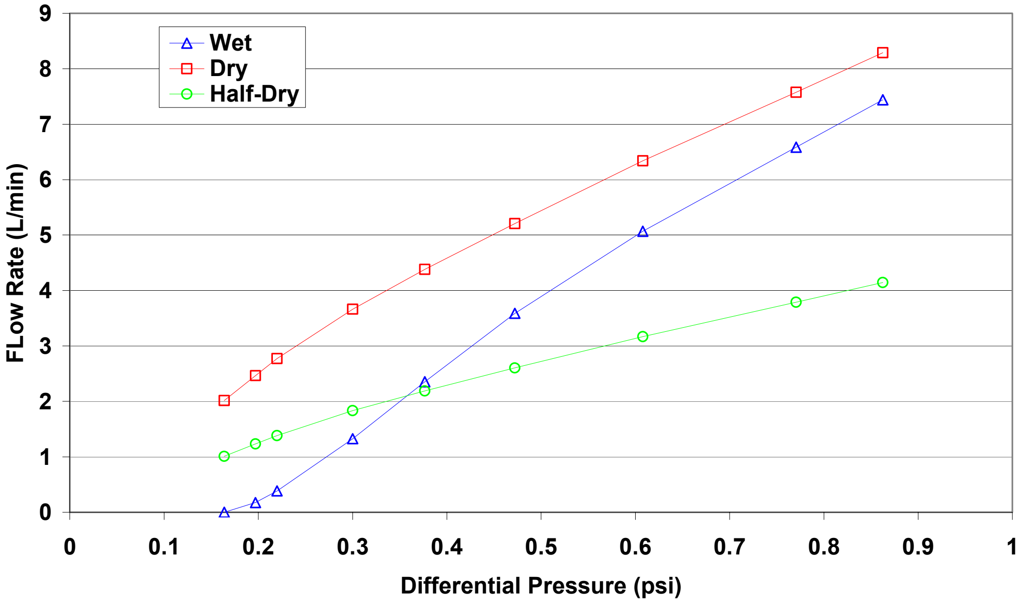

Mean Flow Pore Diameter = 18.42 microns
Bubble Point Pore Diameter = 40.29 microns

Figure 5.36. Wet, Dry and Half-Dry Curves for Teflon-Treated Carbon Paper (Through-Plane Analysis).

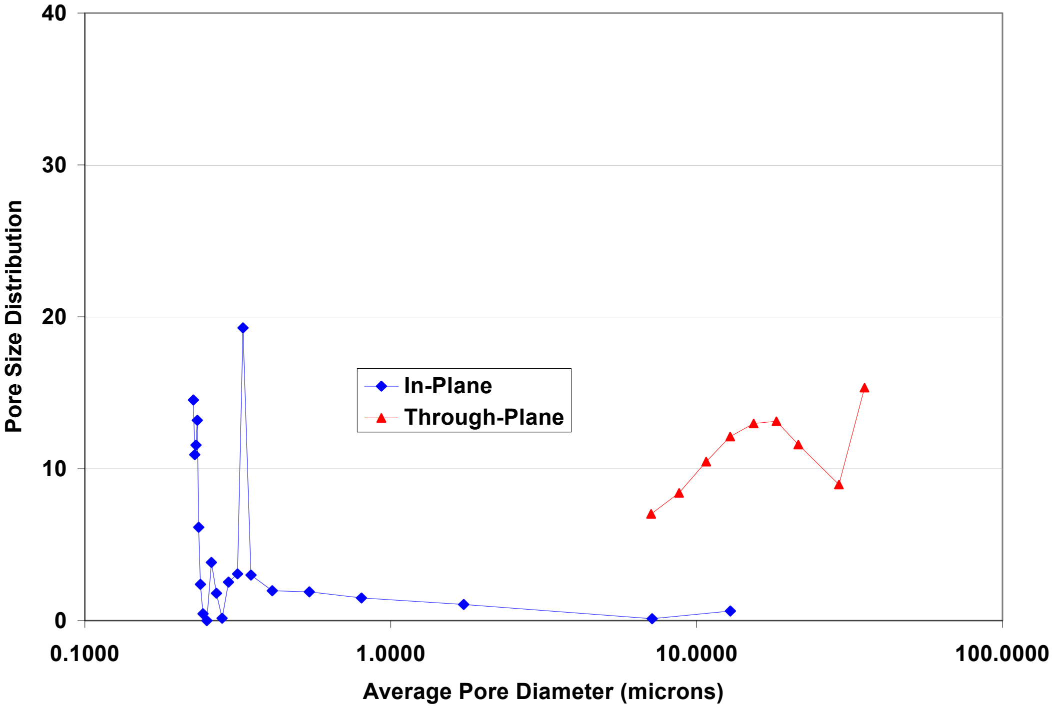

Figure 5.37. Normalized Pore Size Distributions for Untreated Carbon Paper (Capillary Flow Porometry – Through Pores).

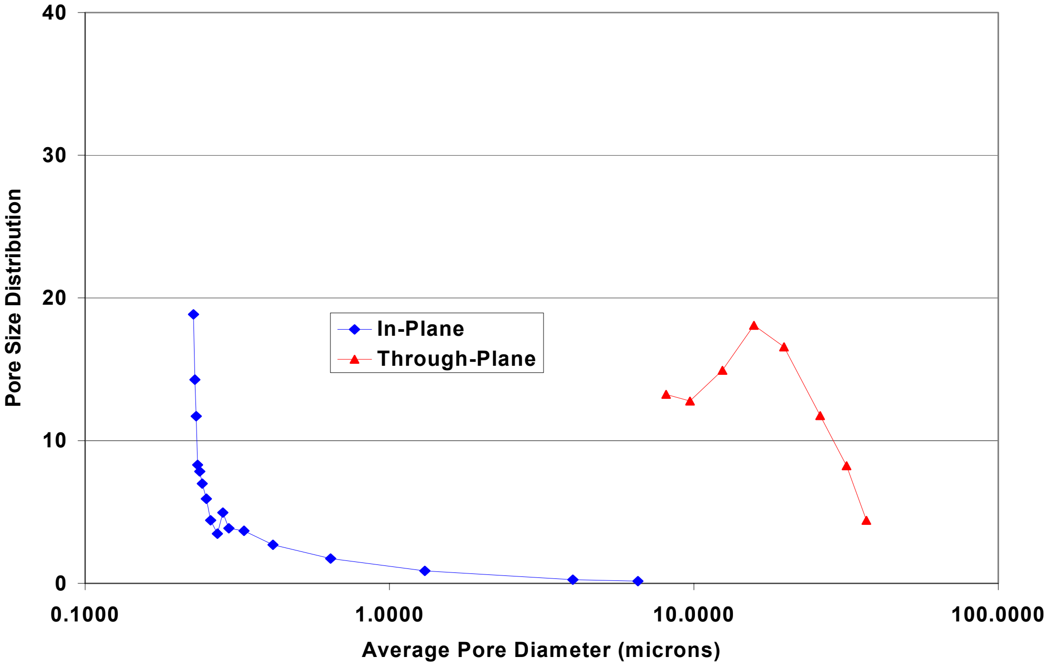

Figure 5.38. Normalized Pore Size Distributions for Teflon-Treated Carbon Paper (Capillary Flow Porometry – Through Pores).

approximately 0.076 Darcy (for Teflon-treated carbon paper) to 0.346 Darcy (for Teflon-treated carbon cloth). These average permeability coefficients reflect the high pressure required to force air to flow in the radial direction of the samples, and also the smaller mean pore sizes present in the direction of flow.

Figure 5.40 provides values of the average permeability coefficient from the through-plane analysis of the four samples studied. The average permeability coefficients are much greater for the carbon cloth (both untreated and Teflon-treated) compared to those for the carbon paper (both untreated and Teflon-treated). The Teflon-treatment of either the carbon cloth or the carbon paper resulted in a decrease in the average permeability coefficient. The average permeability coefficient was 4.67 Darcy for untreated carbon cloth and dropped to 3.56 Darcy for Teflon-treated cloth. For carbon paper, the average permeability coefficient was 0.371 Darcy for the untreated sample and dropped to 0.159 Darcy for the Teflon-treated sample.

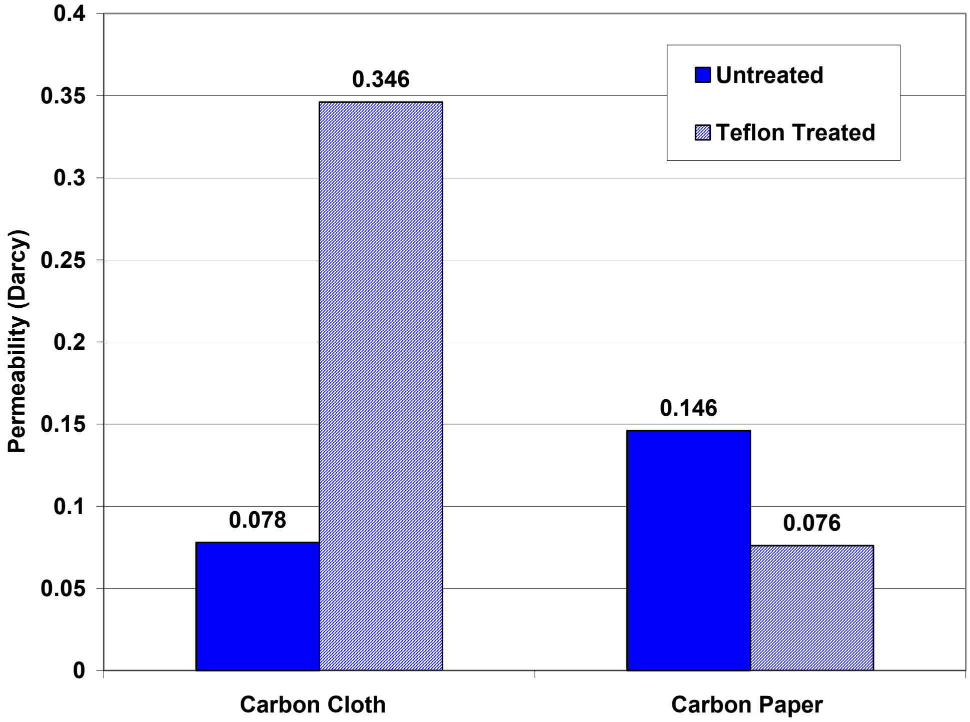

Figure 5.39. Effect of Teflon Treatment on Air Permeability (In-Plane Analysis).

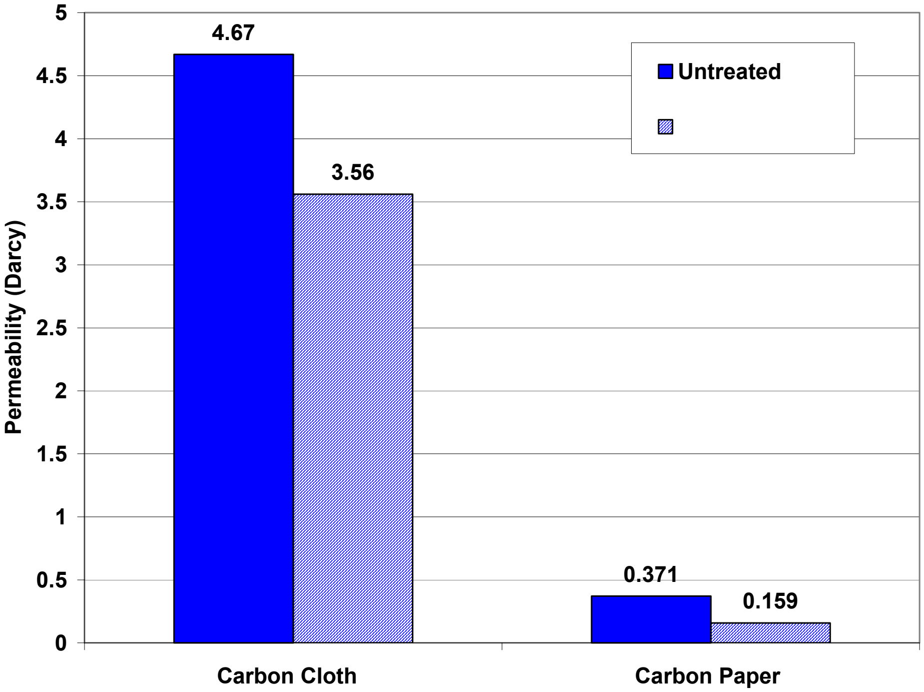

Figure 5.40. Effect of Teflon Treatment on Air Permeability (Through-Plane Analysis).

5.5.3 Mercury/Non-Mercury Porosimetry Results

Evaluation of the characteristics of the GDL is crucial in correlating physical parameters/characteristics with observed performance of a fuel cell system. The GDL distributes the feed gases to the active catalyst sites and facilitates removal of excess water from the electrodes. The pore size distribution and the degree of hydrophobicity exert significant influence on water transport. Inadequate water transport can impact cell operation through flooding of the catalyst or through dehydration of the membrane.

Porosimetry was used to determine the degree of hydrophobicity of the carbon paper and carbon cloth samples. Water porosimetry was used to quantify the hydrophobic portion of the pores. This included: pore size distribution and cumulative pore volume. Mercury porosimetry was used to quantify all pores in the sample (both hydrophobic and hydrophilic). Subtraction of these results should yield the hydrophilic component of the sample.

Pore volume intrusion data for all four samples are compiled in Figure 5.41. In this graph, the cumulative pore volume is plotted as a function of pore diameter, with a cutoff diameter of 0.5 microns. The shape of each curve is characteristic, with the relatively wide plateau over small pore diameters indicating that these small pores (in the range of 0.01 microns to 0.5 microns) contribute only a very small amount to the total cumulative pore volume of a sample. The impact of Teflon treatment on the carbon cloth and the carbon paper was to decrease both the cumulative pore volume and the specific surface area of the given material. For carbon cloth, Teflon treatment resulted in a reduction in cumulative pore volume from 2.67 cc/g to 1.376 cc/g for untreated and

Teflon-treated samples, respectively. The corresponding specific surface area decreased from 0.397 m^2/g to 0.1296 m^2/g. For carbon paper, the Teflon treatment resulted in a reduction in cumulative pore volume from 1.703 cc/g to 1.208 cc/g for untreated and Teflon-treated samples, respectively. The corresponding specific surface area decreased from 0.269 m^2/g to 0.183 m^2/g. These values decreased because the Teflon treatment applied to the sample would tend to fill or partially fill a portion of the pores in the sample, thereby reducing the amount of mercury that must be forced into the sample to fill the pore volume. The specific surface area would also be impacted this same way because the pores would have narrower diameters, resulting in lower available surface

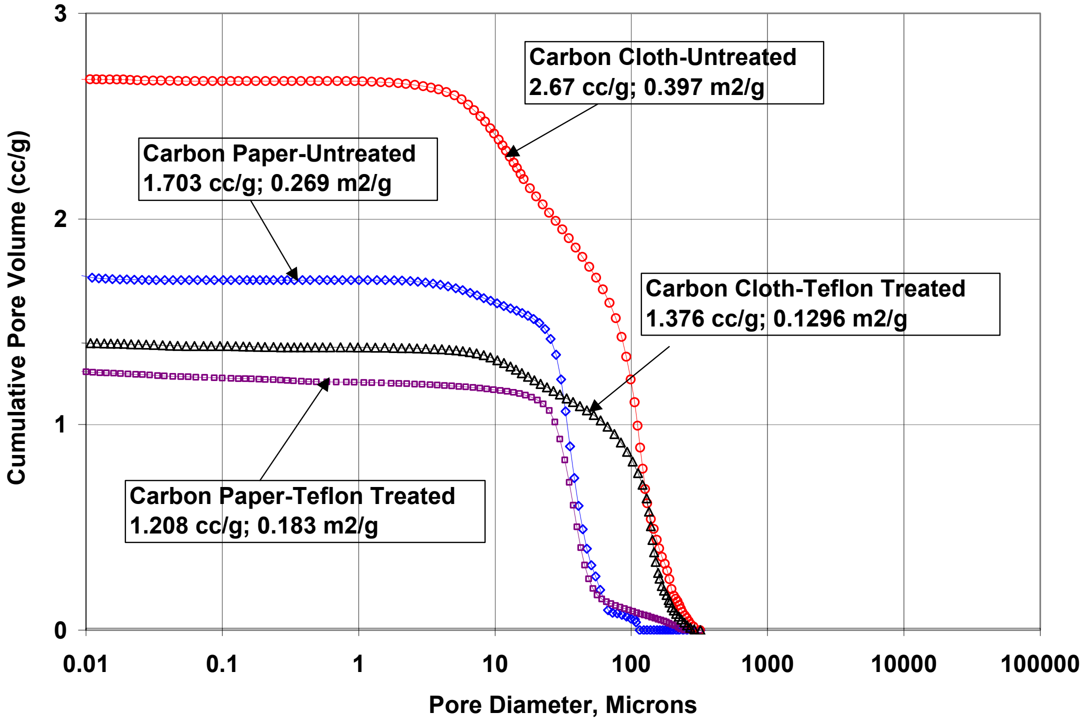

Figure 5.41. Pore Volume Intrusion Data for Through and Blind Pores (Hydrophilic and Hydrophobic) by Mercury Intrusion Porosimetry. Cutoff of 0.5 μ..

area (if pores were assumed cylindrical, this surface area would be represented by πDL, where D is the diameter of the pore, and L is its length).

Figures 5.42 and 5.43 are pore volume distributions for the carbon paper and the carbon cloth, respectively. Distributions for untreated and Teflon-treated samples appear on the sample plot to allow the impact of Teflon treatment to be examined. Treatment with Teflon results in a slight shift of the pore volume distribution in the direction increasing pore diameter for either carbon paper or carbon cloth.

Water intrusion porosimetry was also performed. For water intrusion porosimetry, a sample cell containing both the sample and the water is placed into the sample chamber of the mercury intrusion porosimeter. Figure 5.44 shows the cumulative pore volume for the samples examined as a function of pore diameter. Data analysis similar to that performed for the mercury intrusion porosimetry data was performed. The results, however, are not conclusive at this time. A cutoff pore diameter of 0.5 m was employed, as in the mercury porosimetry studies. One distinctive difference between the mercury intrusion porosimetry results and those from the water intrusion porosimetry experiments was noted. For mercury intrusion porosimetry, the untreated samples had larger cumulative pore volume compared to Teflon-treated samples, either carbon cloth or carbon paper. For water intrusion porosimetry, the untreated samples had smaller cumulative pore volume compared to Teflon-treated samples, either carbon cloth or carbon paper. Another significant difference between the porosimetry measurements is that the largest accessible pore diameter was approximately 320 microns for mercury intrusion porosimetry, while it was approximately 16 microns for water intrusion porosimetry. How this difference impacts the evaluation of cumulative pore volume and specific surface area is under investigation.

The pores in the diameter range of 0.5 to 16 microns are hydrophobic in nature. Mercury intrusion porosimetry provide cumulative volume information on both hydrophilic and hydrophobic pores. Thus, the results from these two experiments allow one to quantify the % of pores in the sample that are hydrophobic (directly from the water intrusion experiment) and the % of pores in the sample that are hydrophilic (by difference from the mercury intrusion and the water intrusion experiments). Data currently available are inconclusive with respect to the degree of hydrophobicity in the samples examined.

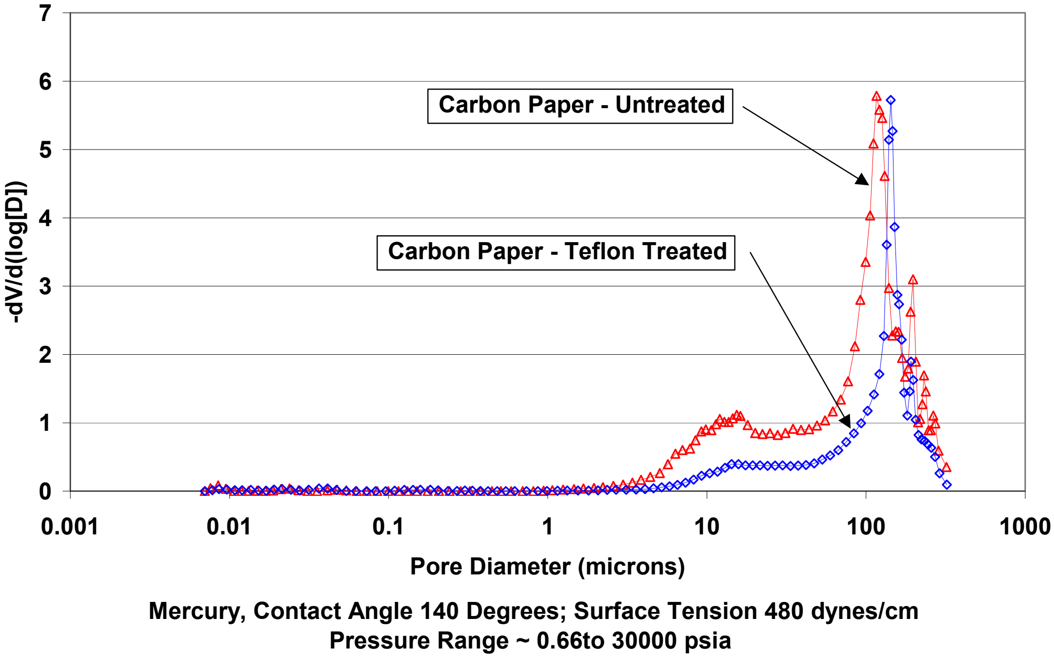

Figure 5.42. Pore Volume Distribution (Hydrophilic and Hydrophobic Pores) for Carbon Paper by Mercury Intrusion Porosimetry.

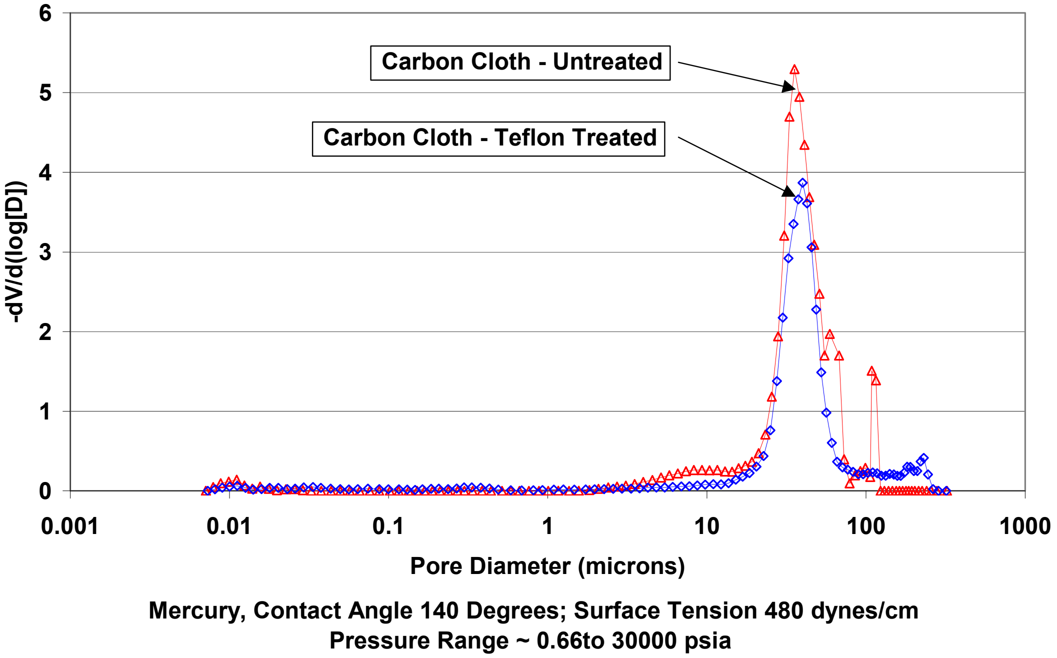

Figure 5.43. Pore Volume Distribution (Hydrophilic and Hydrophobic Pores) for Carbon Cloth by Mercury Intrusion Porosimetry.

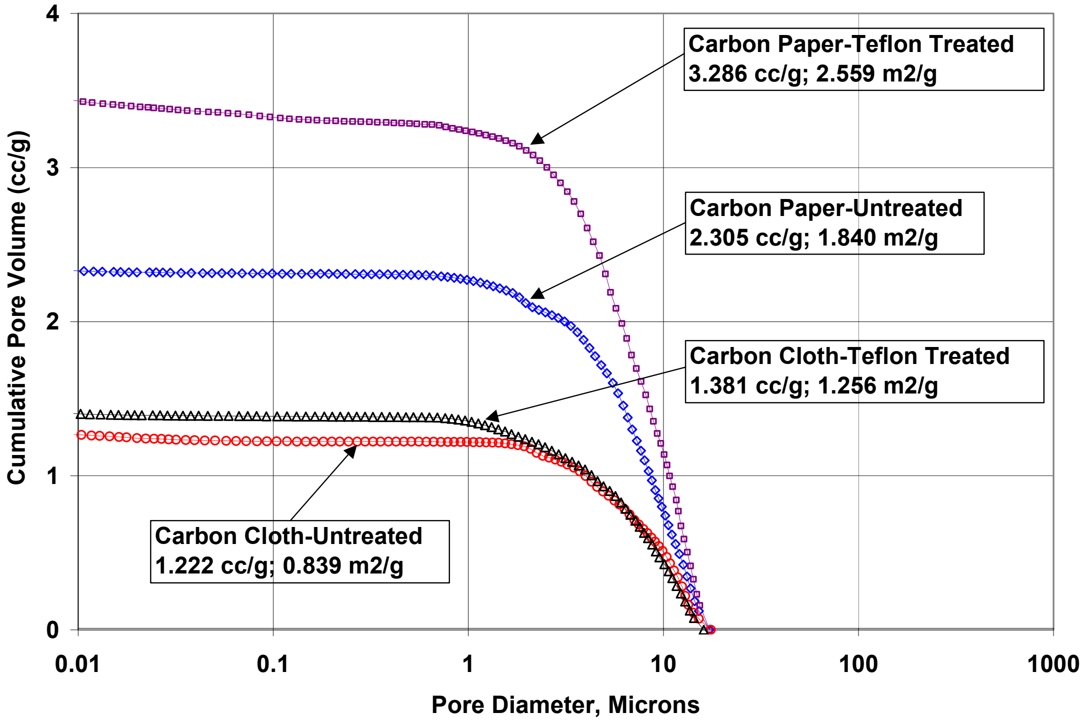

Figure 5.44. Pore Volume Intrusion Data for Through and Blind Pores (Hydrophobic) by Water Intrusion Porosimetry. Cutoff of 0.5 μ.

Figures 5.45 and 5.46 are pore volume distributions from the water intrusion porosimetry experiments for the carbon paper and the carbon cloth, respectively. Distributions for untreated and Teflon-treated samples appear on the sample plot to allow the impact of Teflon treatment to be examined. Treatment with Teflon results in a slight shift of the pore volume distribution in the direction decreasing pore diameter for either carbon paper or carbon cloth. However, there is significant scatter in the data, so results are inconclusive.

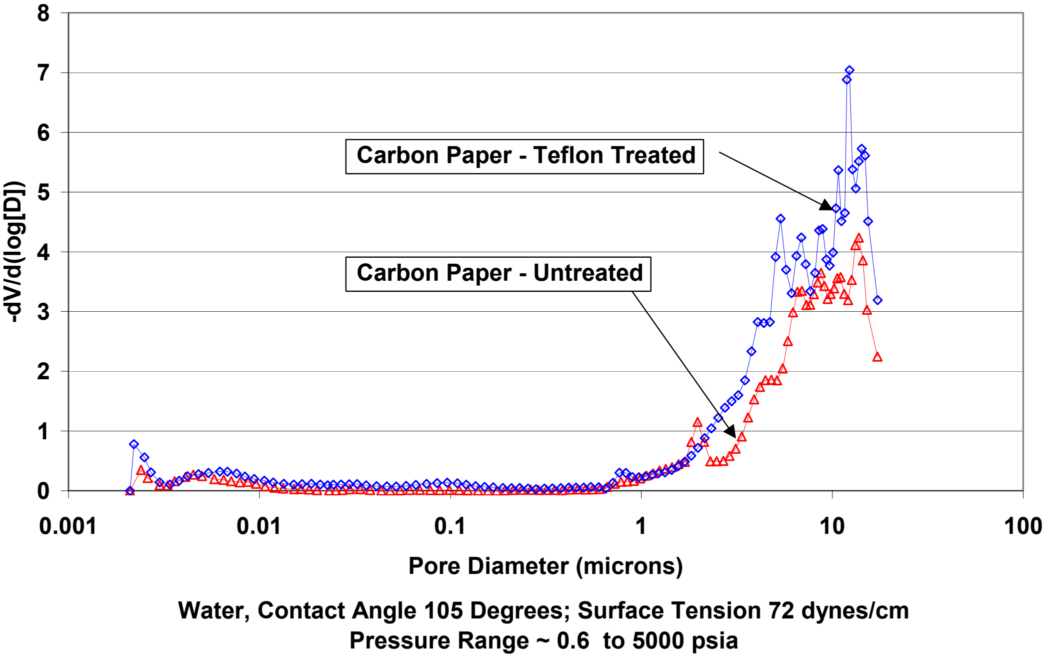

Figure 5.45. Pore Volume Distribution for Through and Blind Pores (Hydrophobic) by Water Intrusion Porosimetry.

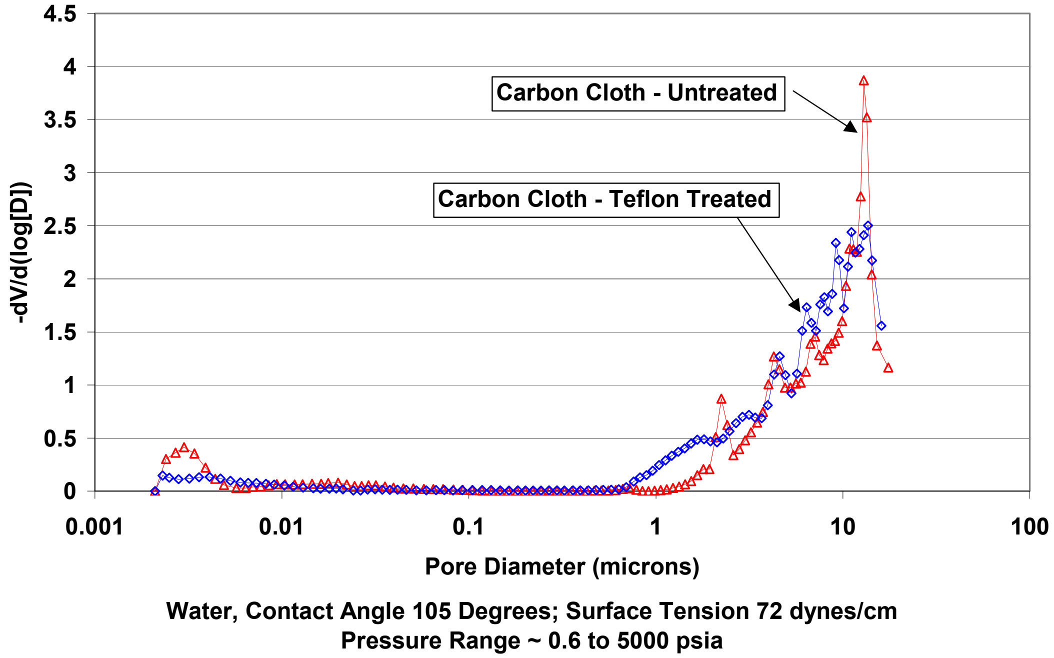

Figure 5.46. Pore Volume Distribution for Through and Blind Pores (Hydrophobic) by Water Intrusion Porosimetry.

5.6 SEM-EDS of Membrane Electrode Assembly

Figure 5.47 is an SEM image of the cross-section of a typical membrane electrode assembly (MEA). This MEA was purchased from E-Tek (Nafion 117, 0.5 mg Pt/cm^2; 20%Pt on Vulcan XC-72; 5 cm x 5 cm). The various regions of importance are readily identified in the image, from top to bottom: GDL, catalyst layer, membrane, catalyst layer, GDL. Compression during assembly results in a reduction in membrane thickness to approximately 109 microns and a reduction in the GDL thickness also. According to Springer et al. (1995), the GDL supplied by E-Tek has a porosity of greater than 75%. Under compression, the porosity may be reduced to approximately 40%, with the thickness reduced by approximately 50%. The original thickness of the GDL was not provided by the supplier, therefore, it is not possible to evaluate the extent to which the thickness was changed during production of the MEA. The intrusion of the electro-catalyst layer into the GDL can also be viewed in Figure 5.47. Figure 5.48 is a SEM image of the surface of the membrane-electrode assembly. The weave of the carbon cloth is readily identified.

Figures 5.49 and 5.50 show SEM images on which locations where energy dispersive x-ray spectroscopy (EDS) was conducted. The elemental composition of the MEA, at these different locations on the MEA, is presented in Tables 5.7 and 5.8. Different regions of membrane (spectrums 1, 2, 3 and 8) showed the presence of carbon, sulfur, and fluorine. Composition of these each element was found to be vary from one region to another.

Spectrums 4, 5, 7, 10, 11, and 12 correspond to the catalyst region. In the in-plane analysis, the Pt composition ranged from ~12.5 % (spectrum 10) to ~29% (spectrum 7). It was not possible to determine the thickness of the catalyst.

The gas diffusion layer showed that fluorine composition varied in different regions, as shown by spectrums 13 through 18. The fluorine content ranged from 0.40 weight % (Spectrum 16) to 8.96 weight % (Spectrum 13). The maximum fluorine composition was found at the surface of the GDL away from the membrane and catalyst layers.

The through-plane surface analysis (Figure 5.50 and Table 5.8) indicated the presence of fluorine-rich regions in the weave of the cloth on the surface of the gas diffusion layer (small clumps that are visible on the surface of the carbon cloth), which indicates the presence of Teflon on the surface of the gas diffusion layer (spectrums 1 and 2). Spectrums 3 through 7 in the Figure 5.50 did not show any trace of fluorine indicating that either the Teflon treatment was not uniformly applied to the entire surface of the carbon cloth or that during the assembly process, the Teflon coating may be extruded through the GDL, resulting in the clumps that are visible on the SEM image.

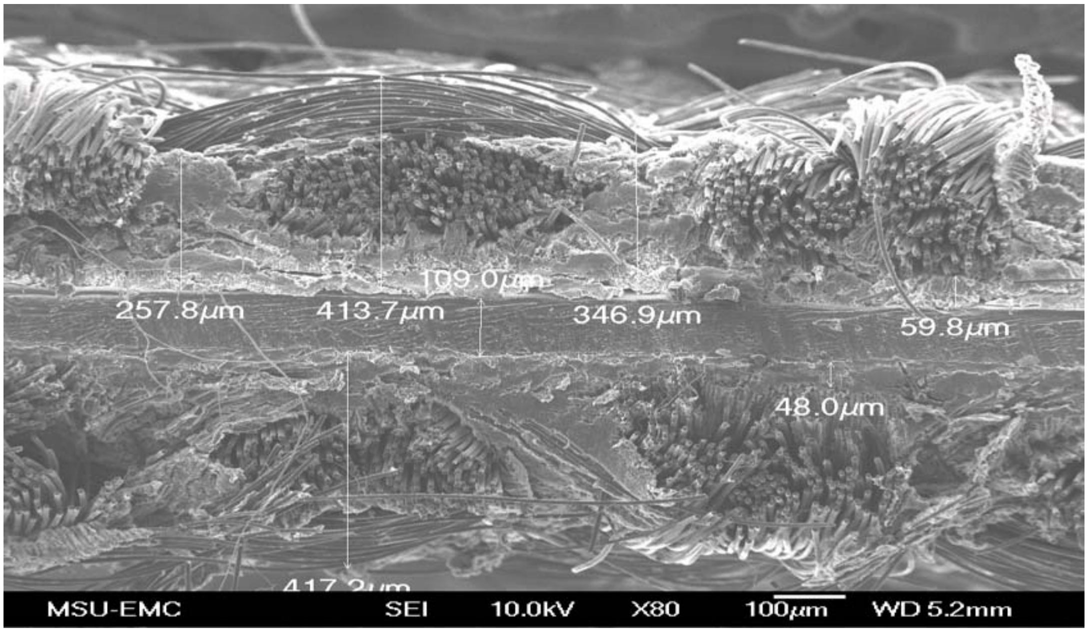

Figure 5.47. SEM Image of Membrane Electrode Assembly (In-Plane View).

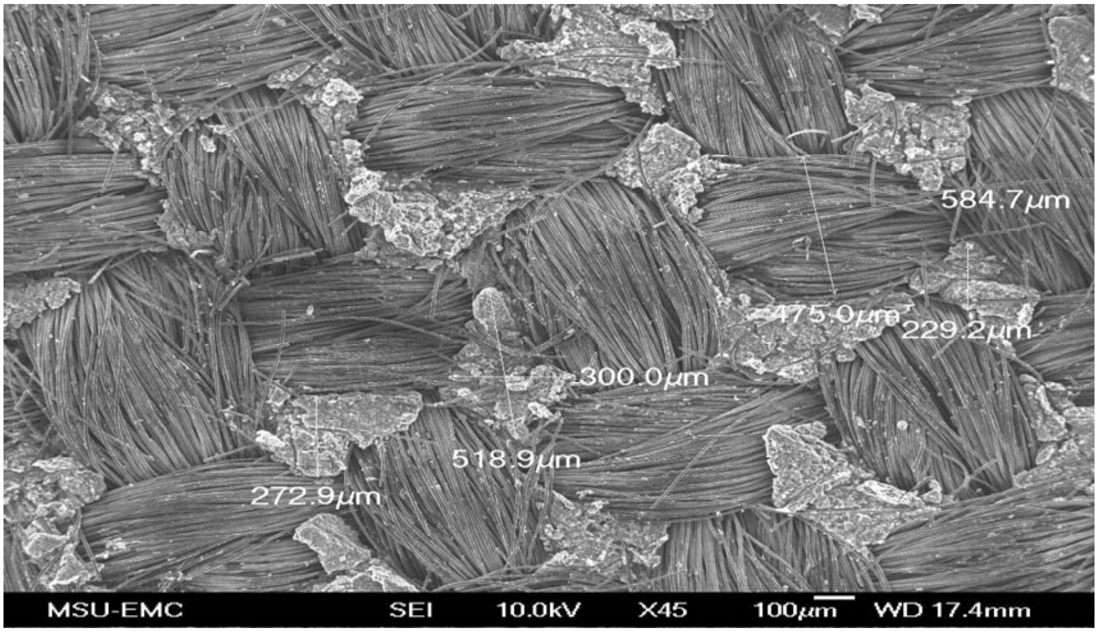

Figure 5.48. SEM Image of Membrane Electrode Assembly (Through-Plane View).

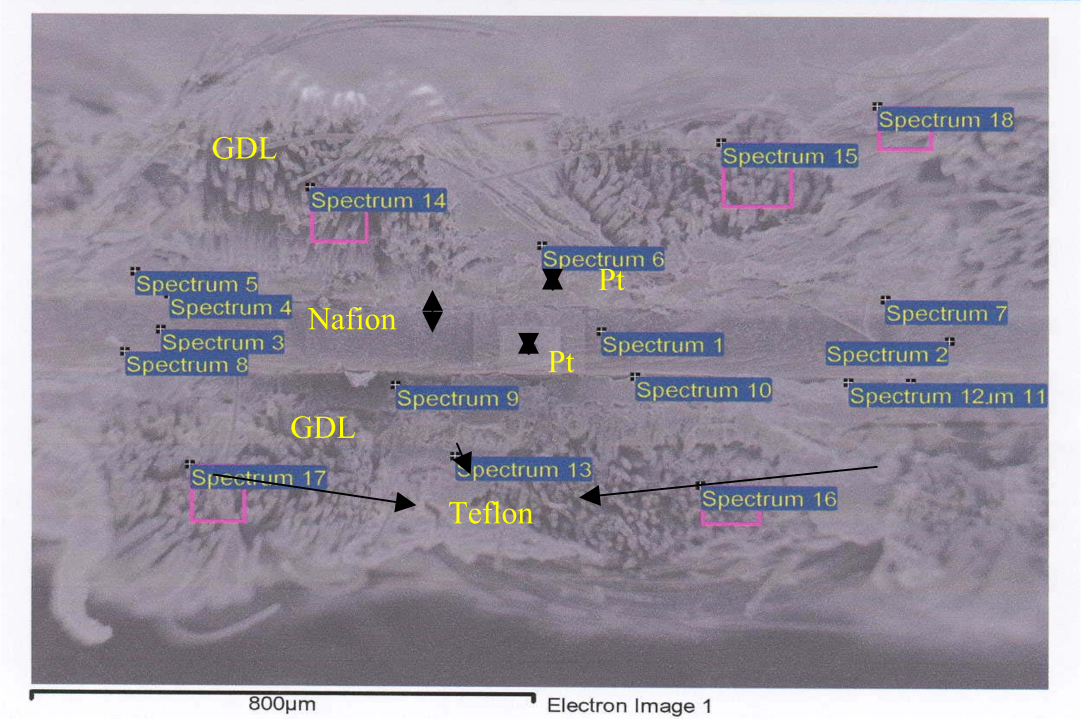

Figure 5.49. SEM Image of MEA (In-Plane View). Locations of EDS Analysis Identified.

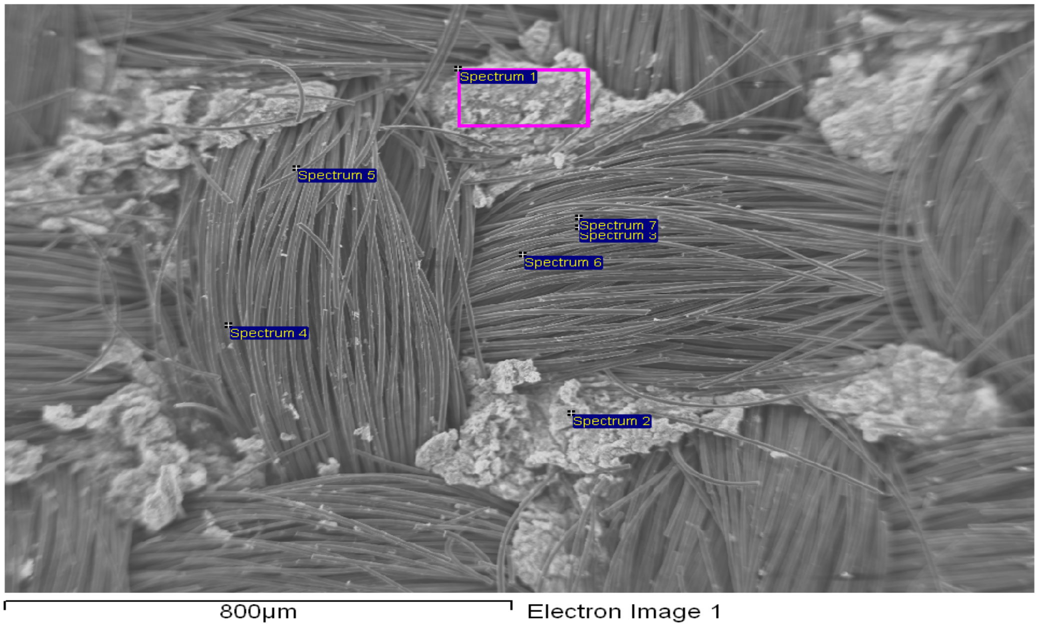

Figure 5.50. SEM Image of MEA (Through-Plane View). Locations of EDS Analysis Identified.

Table 5.7. Elemental Composition of MEA at Different Locations (In-Plane View). Locations Indicated in Figure 5.49.

Spectrum	C	O	F	S	K	Cu	Pt
Spectrum 1	46.62	0.00	31.59	13.45	8.35	0.00	0.00
Spectrum 2	38.95	0.00	36.57	20.21	4.28	0.00	0.00
Spectrum 3	36.74	0.00	37.42	18.57	7.27	0.00	0.00
Spectrum 4	62.15	2.83	16.09	0.89	0.00	0.00	18.04
Spectrum 5	73.02	5.12	3.31	1.25	0.00	0.00	17.30
Spectrum 6	83.75	6.88	9.37	0.00	0.00	0.00	0.00
Spectrum 7	54.66	1.31	14.27	0.98	0.00	0.00	28.78
Spectrum 8	42.79	0.00	48.06	6.95	2.20	0.00	0.00
Spectrum 9	86.43	12.05	1.52	0.00	0.00	0.00	0.00
Spectrum 10	62.78	3.00	20.97	0.68	0.00	0.00	12.57
Spectrum 11	58.84	2.41	24.68	0.66	0.00	0.39	13.02
Spectrum 12	58.32	1.84	14.67	0.80	0.00	0.00	24.37
Spectrum 13	83.12	7.92	8.96	0.00	0.00	0.00	0.00
Spectrum 14	87.9	8.64	3.46	0.00	0.00	0.00	0.00
Spectrum 15	91.27	8.20	0.53	0.00	0.00	0.00	0.00
Spectrum 16	91.51	8.09	0.40	0.00	0.00	0.00	0.00
Spectrum 17	90.77	8.44	0.79	0.00	0.00	0.00	0.00
Spectrum 18	85.71	6.13	8.16	0.00	0.00	0.00	0.00

Table 5.8. Elemental Composition of MEA at Different Locations (Through-Plane View). Locations Indicated in Figure 5.50.

Spectrum	C	O	F	S	Si	Cu	Co
Spectrum 1	77.03	5.08	17.63	0.00	0.00	0.26	0.00
Spectrum 2	77.53	5.25	16.89	0.00	0.00	0.33	0.00
Spectrum 3	91.85	4.43	0.00	3.72	0.00	0.00	0.00
Spectrum 4	86.83	13.17	0.00	0.00	0.00	0.00	0.00
Spectrum 5	95.54	4.46	0.00	0.00	0.00	0.00	0.00
Spectrum 6	86.69	12.54	0.00	0.00	0.12	0.00	0.65
Spectrum 7	89.75	10.05	0.00	0.00	0.12	0.00	0.00

CHAPTER VI

CONCLUSIONS AND RECOMMENDATIONS

6.1 Conclusions

In this work, a one-dimensional, steady state, isothermal PEM fuel cell model was developed. This model was used to examine the impact of process parameters on the various performance measures such as velocity distribution, oxygen concentration distribution, and hydraulic pressure. An iterative approach using the finite element method was used to simultaneously solve the governing differential equation set.

At low current density, the net direction of water flow is from the cathode to the anode. At high current density, the net direction of the flow is reversed. The dissolved oxygen concentration at the membrane/catalyst interface is also strongly influenced by operating current density. The higher the current density, the shorter the penetration distance into the catalyst layer for the dissolved oxygen. Higher cathode gas porosity enhances oxygen transport and improves PEM fuel cell performance. Higher cathode gas pressure results in improved PEM fuel cell performance. As cell operating temperature increased, overall performance improved only slightly. Reduction in the membrane thickness resulted in improved cell performance due to decreased ohmic losses.

The second major component of this thesis focused on experimental characterization of four materials commonly used in the gas diffusion medium/layer. A suite of techniques was employed, including: physisorption; scanning electron microscopy, energy dispersive x-ray spectroscopy, capillary flow porometry, and mercury/non-mercury intrusion porosimetry. The physisorption data were analyzed using two methods: 1) the BET method; and 2) the BJH method. The materials examined were: untreated carbon paper, Teflon-treated carbon paper, untreated carbon cloth and Teflon-treated carbon cloth. Among the samples analyzed, untreated carbon paper had the strongest adsorbent-adsorbate interactions, while the Teflon-treated carbon cloth had the weak interactions. With the nitrogen adsorption experiments, only the micropores were examined, with diameters up to 300 Å.

The surface structure of the materials were qualitatively examined using scanning electron microscopy. Elemental analysis was carried out using energy dispersive x-ray spectroscopy.

The permeability coefficient of the samples in two primary directions, in-plane and through-plane, was determined from capillary gas porometry experiments. The in-plane permeability coefficients were significantly lower than the through-plane values for the carbon cloth, indicating that gas movement in the in-plane direction is much more difficult. For carbon paper, the permeability coefficients for the in-plane and through-plane directions were lower than those for the carbon cloth.

The primary objective of the mercury/non-mercury intrusion porosimetry experiments was to determine the degree of hydrophobicity in the pores of a given sample. While the analysis of the porosimetry data did provide additional information regarding the porous structure of the samples, the results were inconclusive with respect to the degree of hydrophobicity.

6.2 Recommendations

A number of recommendations can be provided to help guide the direction of future work. The fuel cell test bed necessary for providing experimental validation of the computer model was not available until just recently. This test bed can be used to provide experimental validation of the computer model and provide additional polarization curve data with which the model predictions can be compared. Critical information regarding the kinetic parameters of the electrochemical reactions (exchange current density as a function of both operating temperature and pressure) is needed and should be experimentally determined. The effect of relative humidity should be incorporated into the developed model to allow an examination of its impact on membrane hydration.

Physisorption measurements should be repeated using either krypton or argon as the adsorbate. Additional water intrusion porosimetry measurements should be conducted in order to evaluate the degree of hydrophobicity of each sample.

APPENDIX A

INITIAL CALCULATIONS

All calculations are based on base case conditions.

1. $$f = \frac{F}{R\_j * T}$$

Where

F = Faraday Constant = 96484 (coulombs/equivalent)

R_j = Universal gas constant = 8.314 (joule/(mole-K))

T = Temperature = 353 (K)

$$f = \frac{96484\left(\frac{\text{coulombs}}{\text{equivalent}}\right)}{8.314\left(\frac{\text{Joule}}{\text{mole-K}}\right)*353(\text{K})}$$

$$= 32.8754\left(\frac{1}{\text{volts}}\right)$$

2. Diffusivity ratio for water

$$r_w = \frac{pD_{w-N_2}}{pD_{w-O_2}}$$

Where

r_w = Diffusivity ratio of water

pD_{w-N_2} = Gas-pair pressure diffusivity product = 0.387(atm-cm^2/sec)

pD_{w-O_2} = Gas-pair pressure diffusivity product = 0.370(atm-cm^2/sec)

$$r_w = \frac{0.387(\text{atm} - \text{cm}^2/\text{sec})}{0.370(\text{atm} - \text{cm}^2/\text{sec})}$$

$$= 1.0459$$

3. Diffusivity ratio for nitrogen

$$r_{N_2} = \frac{pD_{w-N_2}}{pD_{O_2-N_2}}$$

r_{N_2} = Diffusivity ratio of nitrogen

$pD_{O_2-N_2}$ = Gas-pair pressure diffusivity product = 0.279(atm-cm^2/sec)

pD_{w-N_2} = Gas-pair pressure diffusivity product = 0.387(atm-cm^2/sec)

$$r_{N_2} = \frac{0.387(\text{atm} - \text{cm}^2/\text{sec})}{0.279(\text{atm} - \text{cm}^2/\text{sec})}$$

$$= 1.3871$$

4. Mole fraction of water in the gas phase at saturation

$$y_w^{sat} = \frac{P_w^{sat}}{P_c}$$

y_w^{sat} = Mole fraction of saturated water

P_w^{sat} = Saturated water vapor pressure = 0.467 (atm) at 80 ^{0}C

P_c = Cathode pressure = 5 (atm)

$$y_w^{sat} = \frac{0.467(\text{atm})}{5(\text{atm})}$$

$$= 0.094$$

5. Calculating effective properties of materials

a) Effective oxygen diffusivity

$$D_{O_2}^{eff} = \varepsilon_{m,c} * D_{O_2}$$

Where

$D_{O_2}^{eff}$ = Effective oxygen diffusivity (cm^2/sec)

$\varepsilon_{m,c}$ = Volume fraction of membrane in catalyst region

D_{O_2} = Oxygen diffusivity (cm^2/sec)

$$D_{O_2}^{eff} = 0.4 * 1.2e-6(cm^2/sec)$$

$$= 0.48e-6(cm^2/sec)$$

b) Effective hydraulic permeability

$$k_p^{eff} = \varepsilon_{m,c} * k_p$$

Where

k_p^{eff} = Effective hydraulic permeability (cm^2)

k_p = Hydraulic permeability (cm^2)

$$k_p^{eff} = 0.4 * 1.8e-14$$

$$= 0.72e-14\ cm^2$$

c) Effective electrokinetic permeability

$$k_{\phi}^{eff} = \varepsilon_{m,c} * k_{\phi}$$

Where

k_{ϕ}^{eff} = Effective electrokinetic permeability (cm^2)

k_{ϕ} = Electro kinetic permeability (cm^2)

$$k_{\phi}^{eff} = 0.4 * 7.18e-9$$

$$= 2.872e-9\,\text{cm}^2$$

d) Effective membrane conductivity

$$\kappa_{eff} = \varepsilon_{m,c} * \kappa$$

Where

κ_{eff} = Effective membrane conductivity (mho/cm)

κ = Membrane conductivity (mho/cm)

$$\kappa_{eff} = 0.4 * 0.1$$

$$= 0.04\,(\text{mho/cm})$$

e) Effective diffusivity of water and nitrogen gas-pair

$$pD^{eff} = pD_{w-N_2} * (\varepsilon_{gas})^{1.5}$$

pD^{eff} = Effective water and nitrogen gas-pair diffusivity product (atm-cm^2/sec)

pD_{w-N_2} = Gas-pair diffusivity product (atm-cm^2/sec)

ε_{gas} = Gas phase volume fraction

$pD^{eff} = 0.387 * 0.4$

$= 0.1548\,(\mathrm{atm\text{-}cm^2/sec})$

6. Gas phase mole fraction of nitrogen at the inlet of the cathode

$$X^{c}_{N_2} = \frac{\left(1 - X^{sat}_{w}\right)\left(\frac{\varsigma}{\varsigma - 1}\right)\left(\frac{X^{0}_{N_2}}{X^{0}_{O_2}}\right)}{\left(1 + \left(\left(\frac{\varsigma}{\varsigma - 1}\right)\left(\frac{X^{0}_{N_2}}{X^{0}_{O_2}}\right)\right)\right)}$$

$X^{c}_{N_2}$ = Gas phase mole fraction of nitrogen at the cathode inlet

ς = Stoichiometric flow ratio =3

$\frac{X^{0}_{N_2}}{X^{0}_{O_2}}$ = Inlet Nitrogen-Oxygen mole ratio ($\frac{0.79}{0.21}$)=3.719

X^{sat}_{w} = Saturated mole fraction of water

$$X^{c}_{N_2} = \frac{\left(1 - 0.0934\right)\left(\frac{3}{3 - 1}\right)\left(3.719\right)}{\left(1 + \left(\left(\frac{3}{3 - 1}\right) * \left(3.719\right)\right)\right)}$$

$$= 0.7701$$

7. Concentration of oxygen at the cathode gas diffuser and catalyst layer interface

$$C^{sat}_{O_2} = \left(1 - X_{N_2} - X^{sat}_{w}\right)\left(\frac{P_c}{K_{O_2}}\right)$$

Where

$C_{O_2}^{sat}$ = Gas-phase composition of oxygen in the gas diffuser region (mol/cm^3)

X_w^{sat} = Mole fraction of saturated water

P_c = Cathode pressure (atm)

K_{O_2} = Henry's law constant for oxygen (atm-cm^3/mol)

X_{N_2} = Gas phase mole fraction of nitrogen obtained by solving the following equations.

$$\frac{dX_{N_2}}{dZ} = X_{N_2} * \left(\frac{R\_atm * T}{pD^{eff}}\right)\left(\left(\frac{I}{n\_c * F}\right) r_{N_2} + N_{wg}\right)$$

$$N_{wg} = \frac{\left(I * X_w^{sat}\right)}{\left(n\_c * F\right)\left(1 - X_w^{sat} - X_{N_2}\left(1 - \frac{1}{r_w}\right)\right)}$$

Where

R_atm = Universal gas constant =82.06(atm-cm^3/(mol-K))

T = Cell temperature (K)

n_c = Number of electron participating in the cathode reaction = 4

F = Faraday's constant =96484 (coulombs/equivalent)

N_{wg} = Superficial flux of water in gas phase (mol/(cm^2-sec))

r_w = Diffusivity ratio of water

r_{N_2} = Diffusivity ratio of nitrogen

I = Operating current density (Amps/cm^2)

8. Open circuit potential of PEM fuel cell

$$V_{OC} = U^0_{thermo} + 2.3\left(\frac{R\_j*T}{n\_c*F}\right)\log\left(p^2_{H_2} * p_{O_2}\right)$$

$$U^0_{thermo} = 1.23 - 0.9e - 3*\left(T - 298\right)$$

= 1.23-0.9e-3(353-298)

= 1.1805 (volts)

$$p_{H_2} = P_a = 3(\text{atm})$$

$$p_{O_2} = \left(1 - X^{sat}_w - X^c_{N_2}\right) * P_c$$

= (1-0.0934-0.7701)*5

= 0.6825 (atm)

Where

V_{OC} = Open circuit potential (volts)

U^0_{thermo} = Reference potential (volts)

p_{O_2} = Partial pressure of oxygen (atm)

p_{H_2} = Partial pressure of hydrogen (atm)

$$V_{oc} = 1.1805 + 2.3*\left(\frac{8.314*353}{4*96484}\right)\log\left(3^2*0.6825\right)$$

$$= 1.1805 + 0.013$$

$$= 1.1942 \text{ (volts)}$$

APPENDIX B

GOVERNING EQUATIONS

The main governing equations used in the development of the steady state isothermal PEM fuel cell model are derived in this section. All starting equations are from the paper of Bernardi and Verbrugge (1991). The resulting nonlinear differential equations are then solved in MATLAB$^{@}$ using the Finite Difference Method and an iterative approach. The following set of equations is used to model the cathode side of the PEM fuel cell.

- The Nernst-Planck equation is used to describe the flux of species.

$$N_j = -z_j \frac{F}{R\_j * T} D_j C_j \frac{d\phi}{dZ} - D_j \frac{dC_j}{dZ} + C_j v \qquad \text{(B.1)}$$

Where

N_j = Molar flux of species i (mol/(cm^2-sec))

z_j = Charge on species j

F = Faraday's constant =96484 (coulombs/equivalent)

T = Cell temperature (K)

R_j = Universal gas constant =8.314(joule/(mol-K))

D_j = Diffusion coefficient of species i (cm^2/sec)

C_j = Concentration of species j (mol/cm^3)

ϕ = Membrane phase potential (volts)

v = Water velocity (cm/sec)

Z = Distance (cm)

- The modified form of Schogl's velocity equation

$$v = \left(\frac{k_\phi}{\mu} z_f c_f F\right)\frac{d\phi}{dZ} - \left(\frac{k_P}{\mu}\right)\frac{dP}{dZ} \tag{B.2}$$

k_ϕ = Electro kinetic permeability (cm^2)

k_P = Hydraulic permeability (cm^2)

z_f = Charge of membrane fixed-charge-site (+1)

c_f = Concentration of membrane fixed-charge-site (mol/cm^3)

μ = Pore water viscosity (gram/(cm-sec))

P = Hydraulic pressure (atm)

- The Butler-Volmer equation for electro-kinetics

$$\frac{di}{dZ} = ai_0 * \left(\exp(\alpha_a f(\phi_s - \phi)) - \exp(-\alpha_c f(\phi_s - \phi))\right) \tag{B.3}$$

Where

$$ai_0 = ai_0^{ref} * \left(\frac{C_{O_2}}{C_{O_2}^{ref}}\right)^{\gamma_{O_2}} \left(\frac{C_{H_{P2}}}{C_{H_P}^{ref}}\right)^{\gamma_{H_P}}$$

i = Ionic current density (Amps/cm^2)

ai_0^{ref} = Reference exchange current density times area (Amps/cm^3)

α_a, α_c = Anode and cathode charge transfer coefficient

$f = \dfrac{F}{R\_j * T}$

ϕ_s = Solid phase potential (volts)

$\gamma_{O_2}, \gamma_{H_P}$ = Oxygen and proton concentration parameter for i_0

$C_{O_2}^{ref}, C_{H_P}^{ref}$ = Reference concentrations of oxygen and proton, respectively (mol/cm^3).

- The Stefan-Maxwell equation for gas transport

$$\frac{dX_j}{dZ} = \sum_{m=1}^{n} \frac{R\_atm * T}{pD_{jm}^{eff}} \left(X_j N_{m,g} - X_m N_{j,g} \right) \tag{B.4}$$

X_j = Gas-phase mole fraction of species j

$N_{j,g}$ = Gas-phase flux of species j (mol/(cm^2-sec)

R_atm = Universal gas constant, (atm-cc/(mol-K))

pD_{jm}^{eff} = Effective gas-pair diffusivity of the pair j-m in porous medium (atm-cm^2/sec)

In addition to the above four equations conservation equations for mass, current and momentum are also used to solve for the following variables.

- Membrane phase potential (ϕ)
- Water velocity (v)
- Ionic current density (i)
- Ohmic overpotential (V_{ohmic})

- Oxygen concentration (C_{O_2})
- Hydraulic pressure (P)

The solid phase potential (carbon support/Platinum catalyst) (ϕ_s) is assumed constant and equal to the cell voltage.

B.1 Membrane Phase Potential (ϕ)

B.1.1 Membrane Region

In the membrane region, the membrane phase potential is given by

$$\kappa \frac{d\phi}{dZ} = -i + F * c_f * v \tag{B.1.1.1}$$

Where

ϕ = Membrane phase potential (volts)

i = Ionic current density (Amps/cm^2)

κ = Membrane conductivity (mho/cm)

c_f = Concentration of membrane fixed-charge-site (mol/cm^3)

F = Faraday's constant $\left(96484 \ \frac{\text{coulombs}}{\text{equivalent}}\right)$

v = Water velocity (cm/sec)

Z = Distance (cm)

Taking the divergence of both sides of equation (B.1.1.1) yields:

$$\kappa \frac{d^2\phi}{dZ^2} = -\frac{di}{dZ} + F * c_f * \frac{dv}{dZ} \tag{B.1.1.2}$$

In the membrane region of the PEM fuel cell, the conservation conditions are:

$\frac{di}{dZ} = 0$ Current conservation equation

$\frac{dv}{dZ} = 0$ Incompressible fluid (momentum conservation)

Substituting the conservation equations in equation (B.1.1.2) yields:

$$\frac{d}{dZ}\left(\kappa \frac{d\phi}{dZ}\right) = 0 \tag{B.1.1.3}$$

Equation (B.1.1.3) is the governing equation for the membrane phase potential in the membrane region.

Discretizing equation (B.1.1.3) using the finite center difference formula yields:

$$\frac{\phi_{j-1} - 2\phi_j + \phi_{j-1}}{\Delta Z^2} = 0$$

Which reduces to

$$\phi_{j-1} - 2\phi_j + \phi_{j-1} = 0 \tag{B.1.1.4}$$

B.1.2 Active-Catalyst Region

In the active-catalyst region, the membrane phase potential is given by

$$\kappa_{eff} \frac{d\phi}{dZ} = -i + F * c_f * \varepsilon_{m,c} * v \tag{B.1.2.1}$$

Where

κ_{eff} = Effective membrane conductivity (mho/cm)

$\varepsilon_{m,c}$ = Volume fraction of membrane in catalyst layer

Taking the divergence of both sides of equation (B.1.2.1)

$$\kappa_{eff} \frac{d^2\phi}{dZ^2} = -\frac{di}{dZ} + \left(F * c_f * \varepsilon_{m,c}\right)\frac{dv}{dZ} \tag{B.1.2.2}$$

In the catalyst region, the current in the membrane phase of catalyst layer is transferred to the electronically conductive solid phase of the catalyst layer. The kinetic expression for the electrochemical reaction in the catalyst region is given by the Butler-Volmer equation.

$$\frac{di}{dZ} = ai_0 * \left(\exp\left(\alpha_a f\left(\phi_s - \phi\right)\right) - \exp\left(-\alpha_c f\left(\phi_s - \phi\right)\right) - V_{OC}\right) \tag{B.1.2.3}$$

$$ai_0 = ai_0^{ref} * \left(\frac{C_{O_2}}{C_{O_2}^{ref}}\right)^{\gamma_{O_2}} \left(\frac{C_{H_{P2}}}{C_{H_P}^{ref}}\right)^{\gamma_{H_P}}$$

Assuming that the cathode overpotential is larger than the anode overpotential equation (B.1.2.3) becomes

$$\frac{di}{dZ} = ai_0 * \left(-\exp\left(-\alpha_c f\left(\phi_s - \phi\right)\right) - V_{OC}\right) \tag{B.1.2.4}$$

Liquid water is produced at the cathode of the fuel cell due to the electrochemical reaction. By applying the mass balance

$$\frac{dv_s}{dZ} = -\left(\frac{s_w}{n\_c * F * \rho}\right)\frac{di}{dZ} \tag{B.1.2.5}$$

But

$$v_s = \varepsilon_{m,c}\varepsilon_{w,m} v$$

Substituting v_s in equation (B.1.2.5)

$$\frac{dv}{dZ} = -\left(\frac{s_w}{n\_c * F * \rho * \varepsilon_{m,c} * \varepsilon_{w.m}}\right)\frac{di}{dZ} \qquad \text{(B.1.2.6)}$$

Where

v_s = Superficial water velocity (cm/sec)

$\varepsilon_{w.m}$ = Volume fraction of water in membrane region

s_w = Stoichiometric coefficient of water

ρ = Molar density of water (mol/cm^3)

Substituting equation (B.1.2.6) in equation (B.1.2.2) yields:

$$\frac{d^2\phi}{dZ^2} = -\left(\frac{1}{\kappa_{eff}}\right)\frac{di}{dZ} + \left(\frac{F * c_f * \varepsilon_{m,c}}{\kappa_{eff}}\right) * \left(\frac{-s_w}{n\_c * F * \rho * \varepsilon_{m,c} * \varepsilon_{w,m}}\right) * \frac{di}{dZ}$$

After rearranging

$$\frac{d^2\phi}{dZ^2} = \left(\frac{-1}{\kappa_{eff}}\right) * \left(1 + \frac{s_w * c_f}{n\_c * \rho * \varepsilon_{w,m}}\right) * \frac{di}{dZ}$$

Substituting equation (B.1.2.4) in place of $\frac{di}{dZ}$

$$\frac{d^2\phi}{dZ^2} = \left(\frac{-1}{\kappa_{eff}}\right) * \left(1 + \frac{s_w * c_f}{n\_c * \rho * \varepsilon_{w,m}}\right) * \left(-ai_0\right) * \left(\exp\left(-\alpha_c f\left(\phi_s - \phi - V_{OC}\right)\right)\right)$$

Which reduces to

$$\kappa_{eff}\frac{d^2\phi}{dZ^2} = \left(ai_0\right) * \left(1 + \frac{s_w * c_f}{n\_c * \rho * \varepsilon_{w,m}}\right) * \left(\exp\left(-\alpha_c f\left(\phi_s - \phi - V_{OC}\right)\right)\right) \qquad \text{(B.1.2.7)}$$

Expanding the exponential term using a Taylor series expansion

$$\exp(-\alpha_c f(\phi_s - \phi - V_{OC})) = \exp(-\alpha_c f(\phi_s - \phi_0 - V_{OC}))\text{.........}$$
$$+\exp(-\alpha_c f(\phi_s - \phi_0 - V_{OC}))*(\alpha_c f)*(\phi - \phi_0)$$

$$= \exp(-\alpha_c f(\phi_s - \phi_0 - V_{OC}))*(1 + (\alpha_c f)*(\phi - \phi_0))$$

Now substituting in equation (B.1.2.7)

$$\kappa_{eff}\frac{d^2\phi}{dZ^2} = (ai_0)*\left(1 + \frac{s_w * c_f}{n\_c * \rho * \varepsilon_{w,m}}\right)*(\exp(-\alpha_c f(\phi_s - \phi_0 - V_{OC})))*(1 + (\alpha_c f)(\phi - \phi_0))$$

Let $\text{coef} = ai_0\left(1 + \frac{(s_w * c_f)}{(n\_c * \rho * \varepsilon_{w,m})}\right)*\exp(-\alpha_c f(\phi_s - \phi_0 - V_{OC}))$, then

$$\kappa_{eff}\frac{d^2\phi}{dZ^2} = \text{coef} * (1 + (\alpha_c f)*(\phi - \phi_0)) \qquad \text{(B.1.2.8)}$$

Equation (B.1.2.8) is the governing equation to be solved for the membrane phase potential in the active-catalyst region. Discretizing equation (B.1.2.8) using the finite center difference formula:

$$\kappa_{eff}\left(\frac{\phi_{i-1} - 2\phi_i + \phi_{i+1}}{\Delta Z^2}\right) = \text{coef} * (1 + (\alpha_c f)*(\phi_i - \phi_0))$$

Rearranging the above equation

$$\left(\frac{\kappa_{eff}}{\Delta Z}\right)(\phi_{i-1} - 2\phi_i + \phi_{i+1}) = \text{coef} * (1 + (\alpha_c f)*(\phi_i - \phi_0))*\Delta Z$$

Let $\text{scoef} = \text{coef} * \Delta Z$

$$\left(\frac{\kappa_{eff}}{\Delta Z}\right)(\phi_{i-1} - 2\phi_i + \phi_{i+1}) = \text{scoef} * (1 + (\alpha_c f)*(\phi_i - \phi_0))$$

Simplifying the above equation

$$\left(\frac{\kappa_{\mathrm{eff}}}{\Delta Z}\right)\phi_{i-1} - \left(\frac{2\kappa_{\mathrm{eff}}}{\Delta Z} + \mathrm{scoef} * \left(\alpha_c f\right)\right)\phi_i + \left(\frac{\kappa_{\mathrm{eff}}}{\Delta Z}\right)\phi_{i+1} = \mathrm{scoef} * \left(1 - \left(\alpha_c f\right) * \left(\phi_0\right)\right) \quad \text{(B.1.2.9)}$$

B.1.3 Continuity Condition

At the membrane/catalyst layer interface, the current in the membrane phase is continuous:

$$\kappa\left(\frac{d\phi}{dZ}\right)\Bigg|_m = \kappa_{\mathrm{eff}}\left(\frac{d\phi}{dZ}\right)\Bigg|_c$$

discretizing using finite difference formulas

$$\kappa\frac{\phi_i - \phi_{i-1}}{Z(i) - Z(i-1)} = \kappa * \varepsilon_{m,c} * \frac{\phi_{i+1} - \phi_i}{Z(i+1) - Z(i)}$$

Where i is the interface grid point

After further simplification and rearrangement:

$$\frac{1}{Z(i) - Z(i-1)}\phi_{i-1} - \left(\frac{1}{Z(i) - Z(i-1)} + \frac{\varepsilon_{m,c}}{Z(i+1) - Z(i)}\right)\phi_i + \frac{\varepsilon_{m,c}}{Z(i+1) - Z(i)}\phi_{i+1} = 0 \quad \text{(B.1.3)}$$

B.1.4 Boundary Conditions

At the anode side of the membrane

At Z=0,

$$\phi = 0 \quad \text{(B.1.4.1)}$$

At the end of the active-catalyst region

At Z = l_m + l_c,

$i = 0$

Where

l_m = length of the membrane (cm)

l_c = length of the active-catalyst layer (cm)

Using this condition in equation (B.1.2.1)

$$\kappa_{eff} \frac{d\phi}{dZ} = -i + F * c_f * \varepsilon_{m,c} * v$$

$$\kappa_{eff} \frac{d\phi}{dZ} = F * c_f * \varepsilon_{m,c} * v \qquad \text{(B.1.4.2)}$$

Equations (B.1.1.4) and (B.1.2.9) are the final governing equations in discretized form used to solve for the membrane phase potential along with the continuity and boundary conditions.

B.2 Velocity (v)

B.2.1 Membrane Region

The water velocity is given by Schlogl's equation, which describes the motion of water as a function of potential and pressure gradients.

$$v = \left(\frac{k_\phi}{\mu} z_f c_f F \right) \frac{d\phi}{dZ} - \left(\frac{k_P}{\mu} \right) \frac{dP}{dZ} \qquad \text{(B.2.1.1)}$$

Where

k_ϕ = Electro kinetic permeability (cm^2)

k_P = Hydraulic permeability (cm^2)

z_f = Charge of membrane fixed-charge-site (+1)

c_f = Concentration of membrane fixed-charge-site (mol/cm^3)

μ = Pore water viscosity (gram/(cm-sec))

P = Hydraulic pressure (atm)

B.2.2 Active-Catalyst Region

In the active-catalyst region, Schlogl's equation (with effective permeabilities) is applied to obtain the water velocity.

$$v = \left(\frac{k_\phi^{eff}}{\mu} z_f c_f F \right) \frac{d\phi}{dZ} - \left(\frac{k_P^{eff}}{\mu} \right) \frac{dP}{dZ} \qquad \text{(B.2.2.1)}$$

Where

k_ϕ^{eff} = Effective membrane electro-kinetic permeability (cm^2)

k_P^{eff} = Effective membrane hydraulic permeability (cm^2)

B.2.3 Gas Diffuser Region

The water flow in the gas diffuser region is obtained from Darcy's law.

$$v_s = -\left(\frac{k_{p_s}^d}{\mu} \right) \frac{dP}{dZ} \qquad \text{(B.2.3.1)}$$

Where

$k_{p_s}^d$ = Hydraulic permeability for diffuser region (cm^2)

μ = Pore water viscosity (gram/(cm-sec))

v_s = Superficial liquid velocity (cm/sec)

B.2.4 Continuity Conditions

a. At the membrane/catalyst-layer interface, the flux of liquid water is continuous and therefore, the velocities are related by:

$$v\big|_m = \varepsilon_{m,c} v\big|_c \tag{B.2.4.1}$$

Where subscripts "m", and "c" represent the membrane and catalyst regions, respectively.

b. At the catalyst layer/gas diffuser region, the flux of water is continuous

$$\rho * v_s\big|_c = \rho * v_s\big|_d + N_w^{dp} \tag{B.2.4.2}$$

Where subscripts "c", and "d", represent the catalyst and diffuser regions, respectively.

ρ = molar water density (mol/cm^3)

N_w^{dp} = molar flux of water in gas diffuser region (mol/(cm^2-sec))

B.3 Ionic Current Density (i)

B.3.1 Membrane Region

$$i = -\kappa \frac{d\phi}{dZ} + F * c_f * v \tag{B.3.1.1}$$

Where

i = Ionic current density (A/cm^2)

κ = Membrane conductivity (mho/cm)

c_f = Concentration of membrane fixed-charge-site (mol/cm^3)

ϕ = Membrane phase potential (volts)

v = Water velocity (cm/sec)

Z = Distance (cm)

B.3.2 Active-Catalyst Region

$$i = -\kappa_{eff} \frac{d\phi}{dZ} + F * c_f * \varepsilon_{m,c} * v \qquad \text{(B.3.2.1)}$$

Where

$\varepsilon_{m,c}$ = Volume fraction of membrane in the active-catalyst region

κ_{eff} = Effective membrane conductivity (mho/cm)

Ohmic overpotential is calculated using the following equation

$$V_{ohmic} = i * \frac{\Delta Z}{\kappa_j}$$

Where

V_{ohmic} = Ohmic overpotential (volts)

κ_j = effective membrane conductivity for active-catalyst region

or membrane conductivity

B.4 Oxygen Concentration C_{O_2}

B.4.1 Membrane Region

The dissolved concentration of oxygen in the membrane region is obtained from the Nernst-Planck equation.

$$N_j = -z_j \frac{F}{R\_j * T} D_j C_j \frac{d\phi}{dZ} - D_j \frac{dC_j}{dZ} + C_j v \tag{B.4.1.1}$$

Where $i = O_2$, water, or proton

Since oxygen is not charged, the migration term of the Nernst-Planck equation becomes zero. Therefore, equation (B.4.1.1) becomes

$$N_{O_2} = -D_{O_2} \frac{dC_{O_2}}{dZ} + C_{O_2} v \tag{B.4.1.2}$$

Taking the divergence of both sides of equation (B.4.1.2)

$$\frac{dN_{O_2}}{dZ} = -D_{O_2} \frac{d^2 C_{O_2}}{dZ^2} + \frac{d}{dZ}\left(C_{O_2} v\right)$$

Rearranging

$$\frac{dN_{O_2}}{dZ} = -D_{O_2} \frac{d^2 C_{O_2}}{dZ^2} + v \frac{dC_{O_2}}{dZ} + C_{O_2} \frac{dv}{dZ} \tag{B.4.1.3}$$

From the steady state material balance, the flux of oxygen in the membrane region is given by:

$$\frac{dN_{O_2}}{dZ} = 0 \tag{B.4.1.4}$$

The equation of continuity for an incompressible fluid is:

$$\frac{dv}{dZ} = 0 \tag{B.4.1.5}$$

Substituting equations (B.4.1.4) and (B.4.1.5) in equation (B.4.1.3):

$$0 = -D_{O_2}\frac{d^2C_{O_2}}{dZ^2} + v\frac{dC_{O_2}}{dZ}$$

Further simplifying the above equation:

$$D_{O_2}\frac{d^2C_{O_2}}{dZ^2} = v\frac{dC_{O_2}}{dZ} \tag{B.4.1.6}$$

Equation (B.4.1.6) is the governing equation for the oxygen concentration in the membrane region. Discretizing equation (B.4.1.6) using the centered finite difference formula for the second order derivative and using the forward and backward finite difference formulas for the first order derivatives.

$$D_{O_2}\left(\frac{C_{O_{2_{i-1}}} - 2C_{O_{2_i}} + C_{O_{2_{i+1}}}}{\Delta Z^2}\right) = \left(\frac{v_i + \mathrm{abs}(v_i)}{2}\right)\left(\frac{C_{O_{2_i}} - C_{O_{2_{i-1}}}}{\Delta Z}\right)\text{................} + \left(\frac{v_i - \mathrm{abs}(v_i)}{2}\right)\left(\frac{C_{O_{2_{i+1}}} - C_{O_{2_i}}}{\Delta Z}\right)$$

Velocity is discretized so that both back diffusion of water from cathode to anode and water dragged by protons from anode to the cathode is taken into account. Further simplifying the above equation

$$\left(\frac{D_{O_2}}{\Delta Z} + \left(\frac{v_i + \mathrm{abs}(v_i)}{2}\right)\right)C_{O_{2_{i-1}}} - \left(\frac{2D_{O_2}}{\Delta Z} + \left(\frac{v_i + \mathrm{abs}(v_i)}{2}\right) - \left(\frac{v_i - \mathrm{abs}(v_i)}{2}\right)\right)C_{O_{2_i}} \cdots + \left(\frac{D_{O_2}}{\Delta Z} - \left(\frac{v_i - \mathrm{abs}(v_i)}{2}\right)\right)C_{O_{2_{i+1}}} = 0 \tag{B.4.1.7}$$

B.4.2 Active-Catalyst Region

In the active-catalyst region, the Nernst-Planck equation with effective oxygen diffusivity is

$$N_{O_2} = -D_{O_2}^{eff} \frac{dC_{O_2}}{dZ} + C_{O_2} v$$

Taking the divergence of both sides of this equation

$$\frac{dN_{O_2}}{dZ} = -D_{O_2}^{eff} \frac{d^2C_{O_2}}{dZ^2} + \frac{d}{dZ}\left(C_{O_2} v\right)$$

Which on simplifying gives

$$\frac{dN_{O_2}}{dZ} = -D_{O_2}^{eff} \frac{d^2C_{O_2}}{dZ^2} + v\frac{dC_{O_2}}{dZ} + C_{O_2} \frac{dv}{dZ} \qquad \text{(B.4.2.1)}$$

Liquid water is produced at the cathode of the fuel cell due to electrochemical reaction. By applying the mass balance:

$$\frac{dv_s}{dZ} = -\left(\frac{s_w}{n\_c * F * \rho}\right)\frac{di}{dZ}$$

$$v_s = \varepsilon_{m,c}\varepsilon_{w,m} v$$

Substituting v_s in the above equation

$$\frac{dv}{dZ} = -\left(\frac{s_w}{n\_c * F * \rho * \varepsilon_{w.m}}\right)\frac{di}{dZ} \qquad \text{(B.4.2.2)}$$

By applying the material balance over this region, the flux of oxygen is obtained as

$$\frac{dN_{O_2}}{dZ} = -\left(\frac{s_{O_2}}{n\_c * F}\right)\frac{di}{dZ} \qquad \text{(B.4.2.3)}$$

Where

s_{O_2} = Stoichiometric coefficient of oxygen

From equation (B.1.2.4):

$$\frac{di}{dZ} = ai_0 * \left(-\exp\left(-\alpha_c f\left(\phi_s - \phi\right)\right) - V_{OC}\right)$$

Substituting equations (B.4.2.2) and (B.4.2.3) along with the equation for $\frac{di}{dZ}$ into equation (B.4.2.1) and simplifying, the following equation for the concentration of oxygen is obtained.

$$D_{O_2}^{eff} \frac{d^2 C_{O_2}}{dZ^2} = v \frac{dC_{O_2}}{dZ} - C_{O_2}\left(\frac{s_{O_2}}{n\_c * F} - \frac{s_w * C_{O_2}}{n\_c * F * \rho * \varepsilon_{w,m}}\right)\left(\frac{ai_0^{ref}}{C^{ref}{}_{O_2}}\right)\exp\left(-\alpha_c f\left(\phi_s + V_{ohmic} - V_{OC}\right)\right) \tag{B.4.2.4}$$

Equation (B.4.2.4) is the governing equation for the oxygen concentration in the active-catalyst region. The discretized form of this equation is:

$$\left(\frac{D_{O_2}^{eff}}{\Delta Z} + B\right) C_{O_{2_{i-1}}} - \left(\frac{2D_{O_2}^{eff}}{\Delta Z} + B - E - A\right) C_{O_{2_i}} + \left(\frac{D_{O_2}^{eff}}{\Delta Z} - E\right) C_{O_{2_{i+1}}} = 0 \tag{B.4.2.5}$$

Where $A = \left(s_{O_2} - \frac{s_w * C_{O_2}}{\rho * \varepsilon_{w,m}}\right)\left(\frac{ai_0^{ref}}{C_{O_2}^{ref}}\right)\left(\frac{\exp\left(-\alpha_c f\left(\phi_s + V_{ohmic} - V_{OC}\right)\right) * \Delta Z}{n\_c * F}\right)$

$$B = \left(\frac{v_i + abs\left(v_i\right)}{2}\right)$$

$$E = \left(\frac{v_i - abs\left(v_i\right)}{2}\right)$$

B.4.3 Continuity Condition

At the membrane/catalyst-layer interface, the flux of dissolved oxygen is continuous.

$$D_{O_2} \left.\frac{dC_{O_2}}{dZ}\right|_m = D_{O_2}^{eff} \left.\frac{dC_{O_2}}{dZ}\right|_c$$

After discretizing the equation becomes

$$\frac{1}{Z(i)-Z(i-1)} C_{O_2\, i-1} - \left(\frac{1}{Z(i)-Z(i-1)} + \frac{\varepsilon_{m,c}}{Z(i+1)-Z(i)} \right) C_{O_2\, i} + \frac{\varepsilon_{m,c}}{Z(i+1)-Z(i)} C_{O_2\, i+1} = 0 \tag{B.4.3.1}$$

Where i = Grid point at the interface between the membrane and catalyst-layer

B.4.4 Boundary Conditions

1) At the anode side of the membrane, the oxygen concentration is assumed to be zero.

   i.e., at Z=0 $\quad C_{O_2} = 0$

2) At the end of the cathode catalyst-layer, the oxygen concentration is equal to the gas-phase concentration in the gas diffuser.

   at $Z = 1\_m + 1\_c \qquad C_{O_2} = C_{O_2}^{sat}$

Equation (B.4.1.7) and equation (B.4.2.5) along with continuity condition and boundary conditions are solved for the oxygen concentration profile in the cathode side of the PEM fuel cell.

B.5 Pressure (P)

B.5.1 Membrane Region

The water velocity is obtained from Schlogl's equation of motion as shown in equation (B.2).

$$v = \left(\frac{k_\phi}{\mu} z_f c_f F\right)\frac{d\phi}{dZ} - \left(\frac{k_P}{\mu}\right)\frac{dP}{dZ}$$

By rearranging the velocity equation, the differential equation for pressure is obtained as:

$$\left(\frac{k_P}{\mu}\right)\frac{dP}{dZ} = \left(\frac{k_\phi}{\mu} z_f c_f F\right)\frac{d\phi}{dZ} - v$$

Taking the divergence of both sides of above equation yields:

$$\left(\frac{k_P}{\mu}\right)\frac{d^2P}{dZ^2} = \left(\frac{k_\phi}{\mu} z_f c_f F\right)\frac{d^2\phi}{dZ^2} - \frac{dv}{dZ} \qquad \text{(B.5.1.1)}$$

Substituting $\frac{dv}{dZ} = 0$, incompressible fluid (momentum conservation) and equation (B.1.1.3) in equation (B.5.1.1)

$$\frac{d^2P}{dZ^2} = 0 \qquad \text{(B.5.1.2)}$$

Equation (B.5.1.2) is the governing equation for the hydraulic pressure in the membrane region. Discretizing equation (B.5.1.2) using the centered finite difference formula

$$\frac{P_{j-1} - 2P_j + P_{j-1}}{\Delta Z^2} = 0$$

Which reduces to

$$P_{j-1} - 2P_j + P_{j-1} = 0 \tag{B.5.1.3}$$

B.5.2 Active-Catalyst Region

In the active-catalyst region, the velocity equation (with effective permeabilities) is

$$v = \left(\frac{k_\phi^{eff}}{\mu} z_f c_f F \right) \frac{d\phi}{dZ} - \left(\frac{k_P^{eff}}{\mu} \right) \frac{dP}{dZ}$$

Rearranging the above equation;

$$\left(\frac{k_P^{eff}}{\mu} \right) \frac{dP}{dZ} = \left(\frac{k_\phi^{eff}}{\mu} z_f c_f F \right) \frac{d\phi}{dZ} - v$$

Taking the divergence of both sides of the equation and further simplifying yields:

$$\left(\frac{k_P^{eff}}{\mu} \right) \frac{d^2 P}{dZ^2} = \left(\frac{k_\phi^{eff}}{\mu} z_f c_f F \right) \frac{d^2 \phi}{dZ^2} - \frac{dv}{dZ} \tag{B.5.2.1}$$

In the active-catalyst region, the water velocity is obtained from the mass continuity of liquid water produced using the following equation.

$$\frac{dv_s}{dZ} = -\left(\frac{s_w}{n\_c * F * \rho} \right) \frac{di}{dZ}$$

Where $v_s = \varepsilon_{m,c} \varepsilon_{w,m} v$

Substituting v_s in the differential equation:

$$\frac{dv}{dZ} = -\left(\frac{s_w}{n\_c * F * \rho * \varepsilon_{w.m}} \right) \frac{di}{dZ} \tag{B.5.2.2}$$

Substituting equation (B.5.2.2) in equation (B.5.2.1) and simplifying:

$$\left(\frac{k_P^{eff}}{\mu}\right)\frac{d^2P}{dZ^2}=\left(\frac{k_\phi^{eff}}{\mu}z_f c_f F\right)\frac{d^2\phi}{dZ^2}-\left(-\left(\frac{s_w}{n\_c*F*\rho*\varepsilon_{w,m}}\right)\frac{di}{dZ}\right) \qquad \text{(B.5.2.3)}$$

$$\frac{di}{dZ}=ai_0*\left(-\exp\left(-\alpha_c f\left(\phi_s-\phi\right)\right)-V_{OC}\right)$$

$$ai_0=ai_0^{ref}*\left(\frac{C_{O_2}}{C_{O_2}^{ref}}\right)^{\gamma_{O_2}}\left(\frac{C_{H_{P2}}}{C_{H_P}^{ref}}\right)^{\gamma_{H_P}}$$

Equation (B.5.2.3) is the governing equation for the hydraulic pressure in the active-catalyst region. The discretized form of equation (B.5.2.3) using the centered finite difference formula is:

$$\left(\frac{k_P^{eff}}{\mu}\right)\frac{P_{i-1}-2P_i+P_{i+1}}{\Delta Z^2}=\left(\frac{k_\phi^{eff}}{\mu}z_f c_f F\right)\frac{\phi_{i-1}-2\phi_i+\phi_{i+1}}{\Delta Z^2}\ldots.$$

$$+\left(\frac{s_w}{n\_c*F*\rho*\varepsilon_{w,m}}\right)\frac{di}{dZ}$$

Final form after rearranging the above equation is

$$\left(\frac{k_P^{eff}}{\mu*\Delta Z}\right)P_{i-1}-\left(\frac{2k_P^{eff}}{\mu*\Delta Z}\right)P_i+\left(\frac{k_P^{eff}}{\mu*\Delta Z}\right)P_{i+1}=\left(\frac{k_\phi^{eff}}{\mu}z_f c_f F\right)\frac{\phi_{i-1}-2\phi_i+\phi_{i+1}}{\Delta Z}\ldots.$$

$$+\left(\frac{s_w*\Delta Z}{n\_c*F*\rho*\varepsilon_{w,m}}\right)\frac{di}{dZ}$$

(B.5.2.4)

B.5.3 Gas Diffuser Region

In the gas diffuser region, the overall water balance gives the relationship between the superficial velocity and the water vapor flux:

$$\rho\frac{dv_s}{dZ}=-\frac{dN_{w,g}}{dZ} \tag{B.5.3.1}$$

Where

$$v_s=-\left(\frac{k^d_{p_s}}{\mu}\right)\frac{dP}{dZ} \tag{B.5.3.2}$$

$$N_{wg}=\frac{\left(I*X^{sat}_w\right)}{\left(n\_c*F\right)\left(1-X^{sat}_w-X_{N_2}\left(1-\frac{1}{r_w}\right)\right)}$$

Substituting equation (B.5.3.2) in equation (B.5.3.1)

$$\rho\frac{d\left(-\left(\frac{k^d_{p_s}}{\mu}\right)\frac{dP}{dZ}\right)}{dZ}=-\frac{dN_{w,g}}{dZ}$$

Which reduces to

$$\left(\frac{k^d_{p_s}}{\mu}\right)\frac{d^2P}{dZ^2}=\frac{1}{\rho}\frac{dN_{w,g}}{dZ} \tag{B.5.3.3}$$

Equation (B.5.3.3) is the governing equation for the hydraulic pressure in the gas diffuser region. The discretized form of equation (B.5.3.3) is shown below.

$$\left(\frac{k^d_{p_s}}{\mu}\right)\left(\frac{P_{i-1}-2P_i+P_{i+1}}{\Delta Z^2}\right)=\frac{1}{\rho}\left(\frac{N_{w,g_{i+1}}-N_{w,g_i}}{\Delta Z}\right)$$

After rearranging

$$\left(\frac{k^d_{p_s}}{\mu*\Delta Z}\right)P_{i-1}-\left(\frac{2k^d_{p_s}}{\mu*\Delta Z}\right)P_i+\left(\frac{k^d_{p_s}}{\mu*\Delta Z}\right)P_{i+1}=\frac{N_{w,g_{i+1}}-N_{w,g_i}}{\rho} \tag{B.5.3.4}$$

B.5.4 Continuity Conditions

1. At the Membrane/Active-catalyst layer interface, the following condition is derived from water flux continuity.

$$\left(\frac{k_P}{\mu}\right)\left(\frac{dP}{dZ}\right)\bigg|_m = \left(\frac{k_P^{eff}}{\mu}\right)\left(\frac{dP}{dZ}\right)\bigg|_c$$

After discretizing and using the relationship, $k_P^{eff} = \varepsilon_{m,c} * k_P$, this relationship becomes

$$\frac{1}{Z(i)-Z(i-1)}P_{i-1} - \left(\frac{1}{Z(i)-Z(i-1)} + \frac{\varepsilon_{m,c}}{Z(i+1)-Z(i)}\right)P_i + \frac{\varepsilon_{m,c}}{Z(i+1)-Z(i)}P_{i+1} = 0 \quad \text{(B.5.4.1)}$$

Where i is the grid point at the interface between the membrane and catalyst layer.

2. At the active-catalyst layer/gas diffuser interface, the total flux of water is continuous.

$$\rho\varepsilon_{w,m}\frac{k_\phi^{eff}}{\mu}z_f c_f F\frac{d\phi}{dZ}\bigg|_c - \rho\varepsilon_{w,m}\frac{k_P^{eff}}{\mu}\frac{dP}{dZ}\bigg|_c = -\rho\frac{k_{p,s}^d}{\mu}\frac{dP}{dZ}\bigg| + N_w^{dp}$$

After discretizing and rearranging

$$\left(\frac{\varepsilon_{w,m} * k_P^{eff}}{\mu * (Z(i)-Z(i-1))}\right)P_{i-1} - \left(\left(\frac{\varepsilon_{w,m} * k_P^{eff}}{\mu * (Z(i)-Z(i-1))}\right) + \left(\frac{k_{ps}^d}{\mu * (Z(i+1)-Z(i))}\right)\right)P_i$$

$$+\left(\frac{k_{ps}^d}{\mu * (Z(i+1)-Z(i))}\right)P_{i+1} = \frac{N_w^{dp}}{\rho} - \frac{\varepsilon_{w,m} * k_\phi^{eff}}{\mu * (Z(i)-Z(i-1))}z_f c_f F(\phi_i - \phi_{i-1})$$

(B.5.4.2)

B.5.5 Boundary Conditions

1. At the anode side of the membrane, the pressure is equal to the anode pressure.

   i.e., at $Z = 0$ $P = P_a$

2. At the edge of the gas diffusion layer, adjacent to the cathode gas chamber, the pressure is equal to the cathode inlet pressure.

   At $Z = L$ $P = P_c$

   Where

   L = Total length of the cathode side of fuel cell (l_m + l_c + l_g).

APPENDIX C

PARAMETERS EVALUATION

1. Gas-pair pressure Diffusivity is calculated based on the mass diffusivity equation from Bird et al. as shown below (equation C.1)

$$\frac{pD_{ij}}{\left(P_{c_i}P_{c_j}\right)^{\frac{1}{3}}\left(T_{c_i}T_{c_j}\right)^{\frac{5}{12}}\left(\frac{1}{M_i}+\frac{1}{M_j}\right)^{\frac{1}{2}}} = a\left(\frac{T}{\sqrt{T_{c_i}T_{c_j}}}\right)^{b} \tag{C.1}$$

Where

pD_{ij} = Gas-pair pressure diffusivity of species i-j, (atm-cm^2/sec).

$P_{c,}T_c$ = Critical pressure and critical temperature.

M_i = Molecular weight of component i.

T = Temperature, K

a,b are the constants and their values are given in Table C.1.

Table C.1. Values of Constants.

	a	b
For Non-polar gas-pairs	2.745e-4	1.823
For Water with a non-polar gas	3.640e-4	2.334

Critical properties for oxygen, nitrogen and water are given in Table C.2.

Table C.2. Critical Properties of Components (Perry, 1998).

	Temperature, T_c, K	Pressure, P_c, atm	Molecular Weight, M
Oxygen	154.58	49.94	31.999
Nitrogen	126.2	33.46	33.46
Water	647.13	216.53	18.015

Sample calculation for pressure diffusivity of oxygen and nitrogen gas-pair at 80° C is shown below.

$$\frac{pD_{O_2-N_2}}{(49.94*33.46)^{\frac{1}{3}}(154.58*126.2)^{\frac{5}{12}}\left(\frac{1}{31.99}+\frac{1}{28.014}\right)^{\frac{1}{2}}}=2.745e-4\left(\frac{353}{\sqrt{154.58*126.2}}\right)^{1.8223}$$

$$pD_{O_2-N_2}=0.2795\text{atm}-\text{cm}^2/\sec$$

2. Saturated water vapor pressure is calculated using the Antoine equation (Himmelblau, 1982) as shown in equation (C.2).

$$\ln P^{sat}=A-\frac{B}{T+C} \qquad \text{(C.2)}$$

Where

P^{sat} = Saturated vapor pressure, atm

T = Temperature, K

A, B, C are the Antoine constants.

For temperature range of 284-441 K the Antoine constants are

A = 18.3036

B = 3816.44

C = -46.13

At 80^{o} C, the saturated pressure is calculated by using Antoine equation as

$$\ln P^{sat} = 18.3036 - \frac{3816.44}{353 - 46.13}$$

$$\ln P^{sat} = 5.8669$$

$$P^{sat} = 0.4649 \text{atm}$$

3. Based on the experimental data from Ogumi, et al, Bernardi and Verbrugge developed an empirical expression to calculate the Henry's law constant for oxygen as equation (C.3).

$$K_{O_2} = 1.33e - 6 * \exp\left(\frac{-666}{T}\right) \tag{C.3}$$

Where K_{O_2} = Henry's law constant, atm-cc/mol

T = Temperature, K

At 80 ^{0}C, the Henry's law constant obtained using equation (C.3)

$$K_{O_2} = 1.33e - 6 * \exp\left(\frac{-666}{353}\right)$$

$$K_{O_2} = 2.01e5 \text{ atm-cc/mol}$$

4. Oxygen Diffusivity through the Nafion membrane is calculated using equation (C.4) (Z.Ogumi et al, 1984).

$$D_{O_2} = 3.1e - 3 * \exp\left(\frac{-5500}{RT}\right) \text{ cm}^2\text{/sec} \tag{C.4}$$

Where D_{O_2} = Oxygen Diffusivity through Nafion, cm^2/sec

R = Gas Constant = 1.987 cal/(mol-K)

T = Temperature, K

At 80° C,

$$D_{O_2} = 3.1e-3 * \exp\left(\frac{-5500}{1.987 * 353}\right)$$

$$D_{O_2} = 3.1e-3 * \exp(-7.8413)$$

$$D_{O_2} = 1.2187e-6 \ \text{cm}^2/\text{sec}$$

APPENDIX D

PROGRAM FLOW CHART

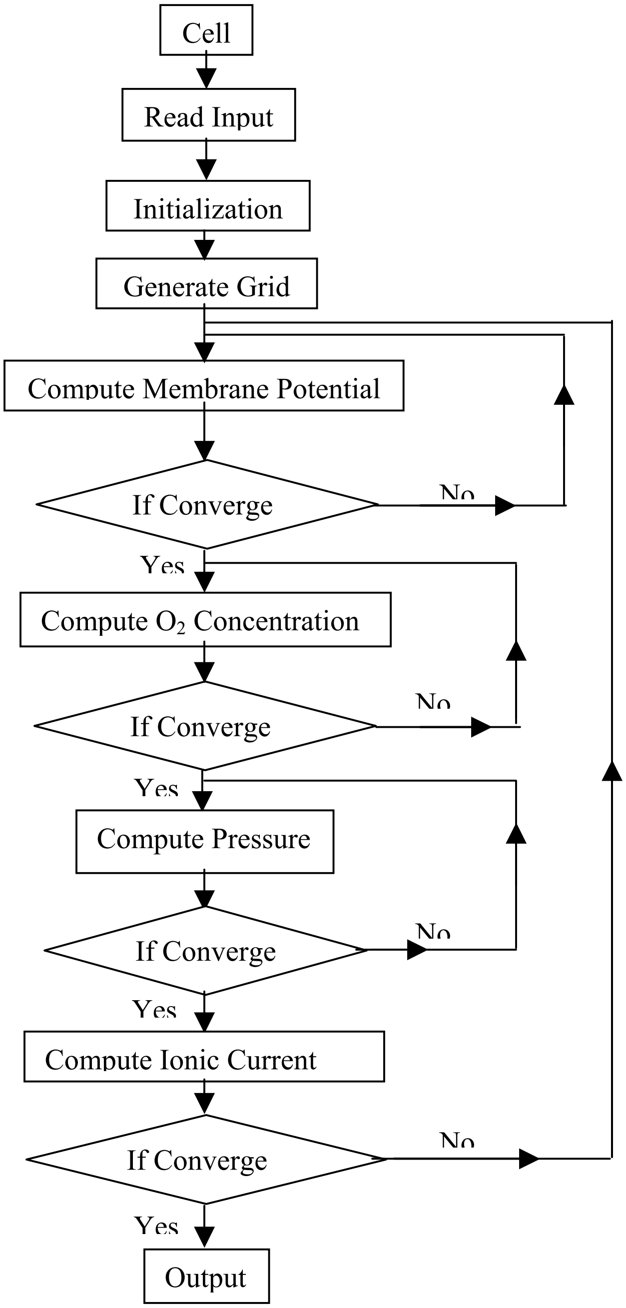

REFERENCES

1) Arvind, P., Martin, C.R., “Investigations of the O_2 Reduction Reaction at the Platinum/Nafion$^{@}$ Interface Using a Solid-State Electrochemical Cell”, *J. Electrochem. Soc.,* 1991, 138, 916-921.

2) Arvind, P., Dave, B., Srinivasan, S., Appleby, A.J., “The Platinum Microelectrode/Nafion Interface: An Electrochemical Impedance Spectroscopic Analysis of Oxygen Reduction Kinetics and Nafion Characteristics”,*J. Electrochem. Soc.,* 1992a, 139, 1634-1641.

3) Arvind, P., Srinivasan, S., Appleby, A.J., Martin, C.R., “Temperature Dependence of the Electrode Kinetics of Oxygen Reduction at the Platinum/Nafion$^{@}$ Interface-A Microelectrode Investigation”, *J. Electrochem. Soc.,* 1992b, 139, 2530-2537.

4) Arvind, P., Srinivasan,S., Appleby, A.J., Martin, C.R., “Pressure Dependence of the Oxygen Reduction reaction at the Platinum Microelectrode/Nafion$^{@}$ Interface: Electrode Kinetics and Mass Transport”*, J. Electrochem. Soc.,* 1992c, 139, 2856-2862.

5) Augustin J. McEvoy, “Fuel Cell Technology Status and Prospects for EPFL Part-I”, http://dcwww.epfl.ch/icp/ICP-2/fcell1.html, 1998.

6) Baker, G.T., “Scanning electron microscope”, Lecture notes, 2001

7) Barrett, E., Joyner, L., Halenda, P., “The Determination of Pore Volume and Area Distributions in Porous Substances! Computations from Nitrogen Isotherms”, *J. of the American Chemical Society*, 1951, 73, 373-380.

8) Bernardi, D.M., Verbrugge, M.W., "Mathematical Model of a Gas Diffusion Electrode Bonded to a Polymer Electrolyte", *AIChE Journal*, 1991, 37, 1151-1163.

9) Bernardi, D.M., Verbrugge, M.W., "A Mathematical Model of the Solid Polymer-Electrolyte Fuel Cell", *J. Electrochem. Soc.*, 1992, 139, 2477-2490.

10) Bird, R.B., Stewart, W.E., Lightfoot, E.N., Transport Phenomena, (John Wiley & Sons, New York, NY: 1960).

11) Brunauer, S., The Adsorption of Gases and Vapors, volume 1, (Princeton University Press, Princeton: 1945).

12) Brunauer, S., Emmett, P., Teller, E., "Adsorption of Gases in Multimolecular Layers", *J. of the American Chemical Society*, 1938, 60, 309-319.

13) Brunauer, S., Deming, L.S., Deming, W.S., Teller, E., "On a Theory of the Van der Waals Adsorption of Gases", *J. of the American Chemical Society*, 1940, 62, 1723-1732.

14) Dannenburg, K., Ekdunge, P., Lindbergh, G., "Mathematical Model of the PEMFC", *J. of Applied Electrochemistry*, 2000, 30, 1377-1387.

15) Daniil Sarkissian, "Numerical Analysis-1" lecture notes. 2002

16) Daniil Sarkissian, "Numerical Analysis-2" lecture notes. 2003.

17) De Boer, J.H., Lisen, B.G., Osinga, T.J., "Studies on Pore Systems in Catalysts V1. The Universal t Curve", *J. of Catalysis*, 1965, 4, 643-648.

18) De Boer, J. H., Lippens, B.C., Broekhoff,J.C., "The t Curve of Multimolecular N_2-Adsorption", *J. of Colloid and Interface Science*, 1966, 21, 405-414.

19) Doan, Phuong "Characterization of Cu-Co-Cr-K Catalyst", 2001, M.S. Thesis, Mississippi State University.

20) EG&G Technical Services, Inc., Fuel Cell Handbook (sixth edition), 2002

21) Fuller, T.F., Newman, J., "Water and Thermal Management in Solid-Polymer Electrolyte Fuel Cells", *J. Electrochem. Soc.*, 1993, 140, 1218-1225.

22) Gregg, S., Sing, K., Adsorption, Surface Area and Porosity, (Academic Press, New York: 1967).

23) Gurau, V., Liu, H., Kakac, S., "Two Dimensional Model for Proton Exchange Membrane Fuel Cells", *AIChE Journal,* 1998, 44, 2410-2422.

24) Grubb, W.T., US patent No. US2913511, 1955.

25) Halsey, G.D., "Physical Adsorption on Non-Uniform Surfaces", *J. of Chemical Physic*, 1948, 16, 931-937.

26) Himmelblau, D.M, Basic Principles and Calculations in Chemical Engineering, (Prentice-Hall, Englewood Cliffs, N.J.: 1982).

27) Hill, T., "Theory of Multimolecular Adsorption from Mixture of Gases", *J. of Chemical Physics*, 1946, 14, 268-275.

28) James, P. J., Elliott, J.A., McMaster, T.J., "Hydration of Nafion studied by AFM and X-ray Scattering", *J. of Materials Science*, 2000, 35, 5111-5119.

29) Jura, G., Harkins, W.D., " Surfaces of Soilds. X1V. A Unitary Thermodynamic Theory of the Adsorption on Solids and of Insoluble Films on Liquid Subphases", *J. of the American Chemical Society*, 1946, 68,1941-1952.

30)Kordesch, K.V., Simander, G.R., “Environmental Impact of Fuel Cell Technology”, *Chem. Rev.*, 1995, 95, 191-201.

31)Kluson, P., Scaife, S.J., “Pore Size Distribution of Structure Different Microporous Carbons-Theoretical Evaluation Based on Density functional Theory and Nitrogen and Argon Experimental Adsorption Isotherms at 77K”, *Chem. Biochem. Eng.*, 2001, 15, 117-125.

32)Larminie J. & Dicks A., Fuel Cell Systems Explained, (2nd edition, John Wiley & Sons, NewYork, N.Y.: 2003).

33)Langmuir, I., “The Adsorption of Gases on Plane Surface of Glass, Mica and Platinum”, *J of the American Chemical Society*, 1918, 40, 1361-1403.

34)Langmuir, I., “Chemical Reactions at Low Pressures”, *J. of the American Chemical Society*, 1915, 37, 1139-1167.

35)Lippens, B.C., De Boer, J.H., “Studies on Pore Systems in Catalysis V. The t Method”, *J. of Catalysis*, 1965, 4, 319-323.

36)Lippens, B.C., Lisen, B.G., De Boer, J.H.,”Studies on Pore Systems in Catalysis 1.The Adsorption of Nitrogen; Apparatus and Calculations”, *J. of Catalysis*, 1964, 3, 32-37.

37)Mathews F., Numerical Methods using MATLAB, (Prentice Hall, Englewood Cliffs, N.J.: 1999).

38)Michael, T.P., Karen, S.H., Arthur, H.J., Kathlyn, L.M., “Scanning Electron Microscopy: A Students Handbook”, 1980, Ladd Research Industries, Inc.

39)Nguyen, T.V., “Proton Exchange Membrane Fuel Cells as an Electrical Power Source: Recent Developments at the University of Kansas”.

40) Nguyen, T.V., White, R.E., "A Water and Heat Management Model for Proton-Exchange-Membrane Fuel Cells", *J. Electrochem. Soc.,* 1993,140, 2178-2186.

41) Nguyen, T.V., "A Gas Distributor Design for Proton-Exchange-Membrane Fuel Cells", *J. Electrochem. Soc*., 1996, 143, L103-L105.

42) Nguyen, T.V., Yi, J.S., "An Along-the-Channel Model for Proton Exchange Membrane Fuel Cells", *J. Electrochem. Soc*., 1998, 145, 1149-1159.

43) Nguyen, T.V., Yi, J.S., "Multicomponent Transport in Porous Electrodes of Proton Exchange Membrane Fuel Cells Using Interdigitated Gas Distributors", *J.Electrochem. Soc*., 1999, 146, 38-45.

44) Ogumi, Z., Takehara, Z., Yoshizawa, S.,, "Gas Permeation in SPE Method. I. Oxygen Permeation Through Nafion and NEOSEPTA", 1984, *J. of the Electrochem. Soc.*, 131, 769-773.

45) Perry, R.H., Green, D.W., Chemical Engineers' Handbook, 7th edition (McGraw-Hill, NewYork, NY: 1998).

46) Pascal, B., Marion, P., CEA_GENEC, "Electrolyzer, Hydrogen Storage and Fuel Cell", WP Report, 2003

47) PMI, Porous Materials, Inc., "Advanced Techniques for Pore Structure Characterization", Short Course Notes, 2003.

48) Quantachrome Corporation, "Gas Sorption System Manual", 1998.

49) Rouquerol, F., Rouquerol, J., Sing, K., Adsorption by Powders and Porous Solids, (Academic Press, London: 1999).

50) Shimshon, G., "The Polymer Electrolyte Fuel Cell: Material Issues in a Hydrogen Fueled Power Source," (2000).

51) Springer, T.E., Zawodzinski, T.A., Gottesfeld, S., "Polymer Electrolyte Fuel Cell Model", *J. Electrochem. Soc.,* 1991, 138, 2334-2341.

52) Springer, T.E., Zawodzinski, T.A.,Wilson, M.S., Gottesfeld, S., "Characterization of Polymer Electrolyte Fuel Cell Using AC Impedance Spectroscopy",*J. Electrochem. Soc*., 1996, 143, 587-599.

53) Springer, T.E., Zawodzinski, T.A., Gottesfeld, S., Derouin,C., Radzinski, S., Sherman, R.J., Smith, V.T.,"Water Uptake By and Transport Through Nafion$^{@}$ 117 Membranes", *J. Electrochem. Soc*., 1993a, 140, 1041-1047.

54) Springer, T.E., Wilson, M.S., Gottesfeld, S., "Modeling and Experimental Diagnostics in Polymer Electrolyte Fuel Cells", *J. Electrochem. Soc*., 1993b, 140, 3513-3526.

55) Springer, T.E., Zawodzinski, T.A., Wilson, M.S., Gottesfeld, S., "Proton Conducting Membrane Fuel Cells I", *The Electrochemical Society Proceedings*, 95(23), 137, (1995).

56) Suzuki, I., "Temperature-Compensated, Differential Tensimeter for Measuring Gas Adsorption by Low Surface Area Solids", *Rev. Sci. Instrum*, 1982, 53, 1061-1066.

57) Uan Zo Li, J.T., "The Effects of Structure, Humidity, and Aging on the Mechanical Properties of Polymeric Ionomers for Fuel Cell Applications", 2001.

58) Um, S., Wang, C.Y., Chen, K.S., "Computational Fluid Dynamics of Proton Exchange Membrane Fuel Cells", *J. Electrochem. Soc.,* 2000, 147, 4485-4493.

59) Uchida, M., Aoyama, Y., Eda, N., Ohta, A., "Investigation of the Microstructure in the Catalyst Layer and Effects of Both Perfluorosulfonate Ionomer and PTFE-Loaded Carbon on the Catalyst Layer of Polymer Electrolyte fuel cells"; *J of Electrochem. Soc*., 1995, 142, 4143-4149.

60) Verbrugge, M.W., "Ion and Solvent Transport in Ion-Exchange Membranes" *J.Electrochem. Soc.,* 1990, 137, 886-893.

61) Verbrugge, M.W., "Methanol Diffusion in Perfluorinated Ion-Exchange Membranes", *J. Electrochem. Soc*., 1989, 136, 417-423.

62) Verbrugge, M.W., Hill, R.F., "Analysis of Promising Perfluorinated Acid Membranes for Fuel Cell Electrolytes" *J. Electrochem. Soc.,* 1990, 137, 3770-3777.

63) Washburn, E.W., *Proc. Nat. Acad. Sci*., 1921, 7, 115.

64) Wang, Z.H., Wang, C.Y., Chen, K.S., "Two-Phase Flow and Transport in the air Cathode of Proton Exchange Membrane Fuel Cells", *J. of Power Sources*, 2001, 94, 40-50.

65) Wang, C.Y., 'Two-phase flow and transport", in Handbook of Fuel Cells – Fundamentals, Technology and Applications, Vielstich, W., Gasteiger, H.A., Lamm, A., editors, (Volume 3, John Wiley and Sons, Ltd.: New York, NY: 2003).

66) Webb, P., Orr, C., "Analytical Methods in Fine Particle Technology", 1998, Micromeritics Instrument Corporation, Norcross, GA.

67) Williams, M.V., Eric, B., Leonard, J.B., Russell, K.H., Fenton, J.M., "Characterization of Gas Diffusion Layers for PEMFCs", ECS_ 202nd meeting abstract, 2002

68) Wu, J., personal communication, (2003).

69) Yeo, S. C., Eisenberg, A., "Physical Properties and Supermolecular Structure of Perfluorinated Ion-Containing (Nafion) Polymers", *J. of Applied Polymer Science*, 1977, 21, 875-898.

70) Young, D. M., Crowell, A D., Physical Adsorption of Gases, (Butterworths Publishers, Washington, D.C.: 1962).